POLITECNICO DI TORINO

Collegio di Ingegneria Chimica e dei Materiali

Master of Science Course in Materials Engineering for Industry 4.0

Master of Science Thesis

Numerical simulation of ball burnishing on aluminium 2024 alloy using hybrid explicit—implicit finite element method.



Supervisors

Candidate

Prof. Daniele Ugues

MENGSTIE Endale Getu

Prof. Milena Salvo

Prof. Valiorgue Frederic

September 2025

Erasmus Mundus Joint Master in Manufacturing 4.0 by intElligent and susTAinable technologies



MASTER's Degree Thesis

Numerical simulation of ball burnishing on aluminium 2024 alloy using hybrid explicit-implicit finite element method.

Supervisors

Prof. Valiorgue Frederic

Prof. Milena SALVO

Prof. Cedric BOSCH

Candidate

Endale Getu MENGSTIE

September 2025













Abstract

Aluminium 2024 alloys are widely used in the manufacturing of aircraft structural components due to high strength-to-weight ratio, excellent resistance to fatigue crack propagation, good fracture toughness, and good machinability. However, the combined effect of local corrosion and cyclic loading leads to crack initiation and propagation during service, ultimately reducing the fatigue life of the component. To address this challenge, mechanical surface treatment (MST) methods, particularly ball burnishing, have emerged as promising post-machining finishing processes. This method induces surface compressive residual stresses, which are used to enhance fatigue performance and improve service life. The present thesis aims to develop an efficient 3D Finite Element Model for the ball burnishing process applied to Aluminium 2024 through a hybrid Explicit-Implicit FEM approach for accurate residual stress prediction. The dynamic explicit analysis is performed to replicate the physical ball burnishing process by designing a modified geometry of the burnishing component, simulating one tool pass to study the thermo-mechanical response during interaction. In contrast, the Implicit FEM approach is developed through the INP file modification technique using the normal stress generated during the Dynamic Explicit analysis to simulate multiple tool passes for residual stress prediction. The 3D FEM model prediction proves that the burnishing force is directly proportional to the generation of compressive residual stress, both at the surface and subsurface stress-affected zone. At applied burnishing force 348N, the tool sliding condition produces a surface axial and lateral compressive residual stress -146.24 MPa and -473.05 MPa, respectively, while the tool rolling condition generates -209.39MPa axial and -478.36 lateral compressive residual stress for an average stable burnished zone. The residual stress prediction shows a good agreement with XRD measurement. At applied burnishing force 275 N and tool sliding condition, the optimum FEM surface axial residual stress was obtained, with 7.8% deviation from XRD measurements.

Acknowledgements

I would like to continue with my acknowledgements for my thesis supervisor, Prof. Valiorgue Frederic, Professor at École Centrale de Lyon, ENISE, for his motivation, patience, and guidance, as well as for sharing his extensive knowledge, which was invaluable for completing my master's thesis. I would also like to say thank you Prof. Joël Rech, CEO of MISUTECH research company, for his project follow-up and other MISUTECH research team members, Ms Mariem Yaich, Mr Marc Raffestin, and Mr. Polly Loïc for their endless support. Thanks to Ms Solis Garduno Rosalinda, LTDS PhD researcher, for her excellent collaboration. I am delighted to have worked with such a dedicated and supportive team, and I look forward to continuing collaborations with this research team in the future.

I am also glad to say many thanks to Prof. Courbon Cédric, Professor at École Centrale de Lyon, ENISE, and Academic Meta 4.0 program coordinator, for his overall guidance and support during my studies, for creating a well-structured research environment, and for providing valuable thesis writing guidelines. Also, thank you, Prof. Milena SALVO and Prof.Daniele UGUES, Professor at Politecnico di Torino, as well as Prof. Cedric BOSCH, Professor at École des Mines de Saint-Étienne, for their guidance and support during my studies and thesis work.

I have to address a special thanks to Dr. Aurélie Brayet, Erasmus Mundus Joint Master Meta 4.0 program manager, for her excellent program management with dedicated support in administrative aspects.

I want to acknowledge the European Union for sponsoring 2-year expenses in the Erasmus Mundus Joint Master's in Manufacturing 4.0 program studies, which also helped me to learn in prestigious European universities with an international cultural exchange environment. My final acknowledgement goes to École Centrale de Lyon, ENISE, which covers the internship fund and useful resources for my thesis work.

Table of Contents

| Abstract | | I |
|-------------|---|-----|
| Acknowle | dgements | II |
| Table of C | ontents | III |
| List of Fig | ures | VI |
| List of Tab | oles | IX |
| Nomencla | ture | X |
| Chapter 1 | Introduction and Background | 1 |
| 1.1. Backş | ground of the study | 1 |
| 1.2. Probl | em Statement | 4 |
| 1.3. Objec | ctive | 5 |
| 1.4. Signif | ficance of the study | 5 |
| 1.5. Scope | e of the study | 6 |
| 1.6. Struc | ture of the thesis | 6 |
| Chapter 2 | Literature Review | 7 |
| 2.1. Surfa | ce integrity | 7 |
| 2.2. Fund | amentals of the ball burnishing process | 7 |
| 2.2.1. | Application of ball burnishing Process | 8 |
| 2.2.2. | Analysis of ball burnishing process parameters | 8 |
| 2.2.3. | Characterisation methods of residual Stress | 10 |
| 2.3. Finite | e element modelling of ball burnishing process | 11 |
| 2.3.1. | Ball burnishing part design and consideration. | 12 |
| 2.3.2. | Ball and workpiece material behaviour | 13 |
| 2.3.3. | Algorithms of contact between ball and workpiece surfaces | 13 |
| 234 | 3D FEM modelling houndary and loading conditions | 14 |

| 2.3.5. | Finite element analysis method | 15 |
|-------------|---|----|
| 2.3.6. | FEM model discretisation strategies | 16 |
| 2.4. Resea | arch summary and gap | 17 |
| Chapter 3 | Methodology | 20 |
| 3.1. Mater | rial | 20 |
| 3.1.1. | Ball Burnishing tool material | 20 |
| 3.1.2. | Ball burnishing work material | 21 |
| 3.2. Ball b | ournishing Experimental setup | 22 |
| 3.3. Finite | e element modelling of ball burnishing | 22 |
| 3.3.1. | Working condition and material property computation | 24 |
| 3.3.2. | Part geometry design and assumptions | 25 |
| 3.3.3. | Constitutive Behaviour law of aluminium 2024 alloy | 27 |
| 3.3.4. | Burnishing tool and work material Contact mechanics | 28 |
| 3.3.5. | Loading strategies for dynamic explicit analysis | 29 |
| 3.3.6. | Loading strategies for standard/implicit analysis | 30 |
| 3.3.7. | Boundary condition | 32 |
| 3.3.8. | Meshing strategy | 32 |
| 3.4. Field | output data extraction and analysis method | 34 |
| 3.4.1. | Manual field output data extraction method | 35 |
| 3.4.2. | Automated field output data extraction method | 35 |
| Chapter 4 | Results and discussion | 36 |
| 4.1. Dyna | mic explicit FEM stability and accuracy | 36 |
| 4.1.1. | Depth of penetration | 37 |
| 4.1.2. | Evolution of reaction force | 39 |
| 4.1.3. | Nodal temperature distribution | 40 |
| 4.2. Burni | ishing tool and work material interaction | 41 |
| 4.2.1. | Contact length and pressure | 43 |

| 4.2.2. | Normal stress distribution | 44 |
|--------------|---|----|
| 4.2.3. | Shear stress distribution | 45 |
| 4.2.4. | Temperature distribution | 46 |
| 4.2.5. | Heat flux distribution | 47 |
| 4.3. FEM | results of plastic strain and residual stress | 48 |
| 4.3.1. | Equivalent plastic strain | 49 |
| 4.3.2. | Residual stress | 51 |
| 4.4. Valid | ation of FEM residual stress results | 56 |
| 4.5. FEM | modelling computational performance | 57 |
| Chapter 5 | Conclusion and future work | 59 |
| 5.1. Concl | lusion | 59 |
| 5.2. Futur | e work: | 61 |
| Appendix | A | 62 |
| Appendix | В | 63 |
| Appendix | С | 64 |
| Appendix | D | 67 |
| Bibliography | | 69 |

List of Figures

| Figure 1.1: Al alloy aircraft structure material, a) S-N curve for different aluminium |
|---|
| alloys [7] and b) crack growth rate for Al 2024 [5]2 |
| Figure 1.2: Schematic illustration of a) surface integrity parameters [16] and b) ball |
| burnishing treatment on a cylindrical workpiece [12]3 |
| Figure 2.1: Plastic deformation phenomenon during burnishing [10]7 |
| Figure 2.2: Working mechanism of the ball burnishing process [16]9 |
| Figure 2.3: Schematic illustration of X-ray diffraction for A and B incident [8]11 |
| Figure 2.4: Ball burnishing part development, a) spherical ball on plate [26] and b) a |
| dome-shaped ball on a plate [17] configuration12 |
| Figure 2.5 : Small cut section for FEM modelling on cylindrical workpiece [28]13 |
| Figure 2.6: Ball burnishing boundary condition for a) cylindrical [12] and b) rectangular |
| plate [33]14 |
| Figure 2.7: Time incrementation under explicit and implicit solvers [36]16 |
| Figure 3.1 : ECL ENISE workshop, a) CNC lathe ball burnishing experimental setup and |
| b) tool workpiece contact [45]22 |
| Figure 3.2: A rectangular cut section on a cylindrical workpiece25 |
| Figure 3.3: Explicit analysis part geometry design a) rectangular plate workpiece, b) 2D |
| and 3D spherical cap burnishing tool26 |
| Figure 3.4: Dynamic explicit analysis part geometry design a) rectangular plate |
| workpiece, b) 3D spherical ball burnishing tool26 |
| Figure 3.5 : Schematic illustration for Hertz contact theory28 |
| Figure 3.6: Surface-to-surface contact between the ball and workpiece and Explicit |
| loading strategies a) tool rolling and b) sliding condition30 |
| Figure 3.7: INP file modification flow chart for the implicit analysis loading31 |
| Figure 3.8: Standard/Implicit FEM modelling loading strategies, a) 3D part with proper |
| mesh and b) 2D surface with pressure load for one tool pass32 |
| Figure 3.9: Work material meshing strategy for a) tool rolling and b) tool sliding FEM |
| modelling approach33 |
| Figure 3.10: Work material meshing strategy and boundary condition for the Implicit |
| FEM modelling approaches 34 |

| Figure $4.1:$ Slide burnishing numerical simulation result at Fb 348 N, a) s' mises stress |
|---|
| distribution, b) temperature distribution |
| Figure 4.2: Roller burnishing numerical simulation result at Fb 348N, a) s' mises stress |
| distribution, b) temperature distribution37 |
| $Figure\ 4.3:\ Evolution\ of\ penetration\ during\ the\ slide\ ball\ burnishing\ process38$ |
| Figure 4.4 : FEM modelling, a) tool sliding displacement result at Fb 348N and b) average |
| penetration at stable zone for different forces and types of tool motion39 |
| Figure 4.5 : Evolution of reaction force a) tangential (Ft) and b) normal (Fn)40 |
| Figure $4.6:$ Average Tangential and normal reaction force at the stable region40 |
| Figure 4.7: Nodal temperature distribution, a) tool sliding FEM result at Fb 348 N and |
| b) comparison of TR and TS with different burnishing forces41 |
| Figure 4.8 : A stable region cube section FEM result at Fb 348N a) 3D s33 (normal stress) |
| distribution and b) 2D surface contact region42 |
| Figure 4.9 : Surface contact length for different burnishing forces, a) at 275N, b) at 348N |
| and c) at 420N43 |
| Figure 4.10: Normal stress distribution a) 3D plot, b) 2D contact surface, c) 2D plot |
| normal stress for 31-line and d) 2D plot in burnishing direction44 |
| Figure 4.11: Shaer stress distribution, a) 3D plot, b) 2D contact surface, c) 2D plot shear |
| stress for 31-line and d) 2D plot in burnishing direction45 |
| Figure 4.12: Temperature distribution a) 3D plot, b) 2D contact surface, c) 2D plot |
| temperature for 31-line and d) 2D plot in burnishing direction46 |
| Figure 4.13: Heat flux distribution a) 3D plot, b) 2D contact surface, c) 2D plot for heat |
| flux for 31-line and d) 2D plot in burnishing direction |
| Figure 4.14: S, Mises distribution at tool sliding condition and 348N burnishing force.48 |
| Figure 4.15 : PEEQ distribution at tool sliding and 348 N burnishing force50 |
| Figure 4.16: PEEQ distribution through the surface, a) for tool sliding and rolling at Fb |
| 348 N and b) average surface PEEQ at the stable zone50 |
| Figure 4.17: PEEQ distribution through the depth, a) for the tool sliding condition and |
| b) for the sliding and rolling condition at Fb 348 N50 |
| Figure 4.18: Stress field output distribution for 10 tool passes, a) s11 and b) S2252 |
| Figure 4.19: Surface lateral and axial residual stress (RS) distribution for tool sliding and |
| rolling conditions at Fb 348N |

| Figure 4.20: Average axial and lateral surface residual stress for tool rolling and sliding |
|--|
| conditions and burnishing forces. |
| Figure 4.21: Lateral residual stress distribution under tool sliding through the depth |
| extracted at, a) at the centre of contact and b) at the centre of overlap54 |
| Figure 4.22: Lateral residual stress for tool rolling and sliding condition at Fb $348\ N$ |
| extracted at, a) at the centre of contact and b) at the centre of overlap54 |
| Figure $4.23:$ Tool sliding condition axial residual stress through the depth, a) at the |
| centre of contact and b) at the centre of overlap55 |
| Figure 4.24: Axial residual stress distribution for tool sliding and rolling condition at Fb |
| 348N, a) at the centre of contact and b) at the centre of overlap55 |
| Figure 4.25: Comparison of lateral residual stress (RS) distribution through the depth |
| between 3D FEM results and XRD measurements |
| Figure 4.26: Comparison of axial residual stress (Rs) distribution through the depth |
| between 3D FEM results and XRD measurements |
| Figure 4.27: Comparison of Computational performance for the dynamic explicit and |
| implicit FEM modelling approach |

List of Tables

| Table 2.1: Literature summary for the experimental ball burnishing process | 18 |
|---|-------|
| Table 2.2 : Literature summary for the 3D finite element modelling of the ball burnis | shing |
| process | 19 |
| Table 3.1 : Material properties of tungsten carbide [44] | 21 |
| Table 3.2: Chemical composition of AA2024 alloy | 21 |
| Table 3.3 : Material properties of aluminium 2024 alloy | 21 |
| Table 3.4: Working conditions for FEM modelling of the ball burnishing process | 24 |
| Table 3.5. Johnson Cook parameter for Aluminium 2024 [48], [50] | 28 |
| Table 3.6: HCT estimation of contact dimension and pressure | 29 |
| Table 4.1 : Contact length and maximum pressure at different burnishing force | 43 |
| Table 4.2 : Explicit and implicit FEM modelling computational performance | 58 |

Nomenclature

Abbreviations & acronyms

| CAE | Computer | -Aided | Engine | eering |
|-------|----------|--------|--------|--------|
| O1 11 | Compace | IIIaca | | |

FEM Finite Element Modelling

MST Mechanical Surface Treatment

INP INPut file

ODB Output DataBase

FEA Finite Element Analysis

CNC Computer Numerical Control

Fb Burnishing Force

TS Tool Sliding

TR Tool Rolling

XRD X-Ray Diffraction

JC Johnson Cook

HCT Hertz Contact Theory

GUI Abaqus Graphical User Interface

API Abaqus Application Programming Interface

APE Abaqus Python Environment

Fn Normal Force

Ft Tangential Force

BB Ball burnishing

RS Residual stress

Co Centre of overlap

Cc Centre of contact

Common Symbols

- P Pressure
- d Diameter
- f Feed rate
- a Contact length
- A Initial yield Strength
- C Strain rate constant
- $\dot{\varepsilon}$ Strain rate
- $\dot{\varepsilon}_{O}$ Reference strain rate
- n Strain hardening exponent,
- ε Plastic Strain
- B Hardening constant
- m Thermal softening exponent.
- $\delta \qquad \text{Indentation depth} \\$
- p_o Maximum pressure
- E Young's modulus
- E* Effective Young's modulus
- ϑ Poisson's ratio
- V Speed
- ρ Density
- λ Thermal conductivity
- *Cp* Specific heat
- α Expansion coefficient
- β Taylor Quinney Coefficient
- Al Aluminium

Abaqus software Symbol

| S11 | Normal stress in X direction |
|------|---|
| S22 | Normal stress in the Y Direction |
| S33 | Normal stress in Z Direction |
| S23 | Shear stress between the Y and Z directions |
| HFL | Heat flux |
| TEMP | Temperature |
| U1 | Displacement in the X direction |
| U2 | Displacement in the Y direction |
| U3 | Displacement in the Z direction |
| PEEQ | Equivalent plastic strain |
| NT11 | Nodal temperature distribution |
| RF2 | Reaction force in Y direction |
| RF3 | Reaction force in Z direction |

Chapter 1

Introduction and Background

In recent years, various industrial sectors have increasingly focused on enhancing the surface integrity of mechanical components to extend their service life. To ensure reliable performance and prolonged service life, their components require a high surface finish. Functional properties, including wear resistance, fatigue strength, corrosion resistance, and power loss from friction, are all significantly influenced by the surface finish. Unfortunately, these strict requirements cannot be accomplished by ordinary machining processes, such as turning, milling, or even classical grinding [1]. To address this challenge, mechanical surface treatment (MST) methods, particularly ball burnishing, have emerged as promising post-machining processes to improve surface properties. The aim is to understand the mechanical behaviour during burnishing better and validate experimental surface integrity properties through numerical modelling using the Finite Element Method (FEM) for the ball burnishing process on Aluminium 2024 alloy material.

1.1. Background of the study

The structural component of aircraft has been made from the optimal Aluminium alloy material for more than 80 years [2]. In commercial aircraft, 60 to 80% weight of the bodies is made from aluminium alloy [3]. It remains the main choice for structural components such as fuselage, wings and supporting structure of commercial airliners [2], [4]. Aluminium alloys are widely used in the manufacturing of aircraft components [5], due to its favourable mechanical and manufacturing properties, including adequate yield strength, excellent resistance to fatigue crack propagation, good fracture toughness, and machinability, facilitates an increase in the number of cycles before failure [6] presented in Figure 1.1a.

The Aloha Airlines accident in 1988 clearly demonstrated the dangers associated with the structural degradation of aeroplane aluminium alloy components. The degradation in fatigue life of the Al 2024 component was due to the initiation of a crack and growth at corrosion pits [5] as shown in Figure 1.1b.

The aircraft structures are mainly subjected to cyclic loading, which leads to the initiation of a crack, particularly the maximum stress-affected zone of the rear fuselage structure of the aircraft, approximately 22,222 flying hours [4].

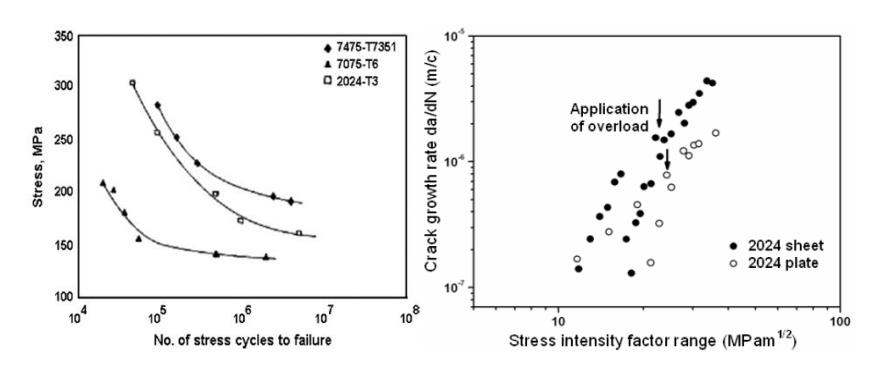


Figure 1.1: Al alloy aircraft structure material, a) S-N curve for different aluminium alloys [7] and b) crack growth rate for Al 2024 [5].

The surface of an engineering part can be defined as the boundary between the environment and the machined component. A real solid surface on metallic material may look clean and smooth or polished, but it has micro layers formed due to external factors, including the manufacturing process, temperature and oxidation [8]. A part's poor surface quality would accelerate the emergence and propagation of cracks and eventually trigger the component to fail [9].

The Mechanical surface treatment (MST) method, which is the plastic deformation of the surface peaks created by either rolling or sliding contact between the deforming components, provides a good surface treatment [10], [11]. The MST method has several advantages over finishing machining methods, including higher productivity, better surface finish, no material loss, lower heating on the treated surface, uniform microstructure, hardening, and induction of compressive residual stresses without any alteration in chemical composition [12], [13]. It can be either dynamic (shot peening and laser peening) or static (burnishing processes). The static methods are suitable for treating rotational surfaces and have the advantage that their working parameters are more easily adjusted to attain the desired surface integrity [14].

Surface integrity was introduced by Dr. M. Field and Dr. J. Kahles in 1964, referring to the enhanced material surface property through a manufacturing process. The two regions of surface integrity in the material component are surface topography and subsurface characteristics. The outer layer surface property in the component is known as surface topography. Surface characteristics or metallurgies are the properties of an altered layer found beneath the surface with respect to the base material [8], [15].

Ball burnishing is a static MST method recognised by its cost-effectiveness [10] and it is a superfinishing process that consists of hard ball rolling on the surface of the work material, which can deform the peak of the surface roughness plastically [16]. It's also called a non-chip finishing process performed usually at low temperature, used to improve surface compressive strength, corrosion resistance, hardening, and smoothness. The flattening of the roughness profile results in the introduction of a new surface integrity property, shown in Figure 1.2 [11].

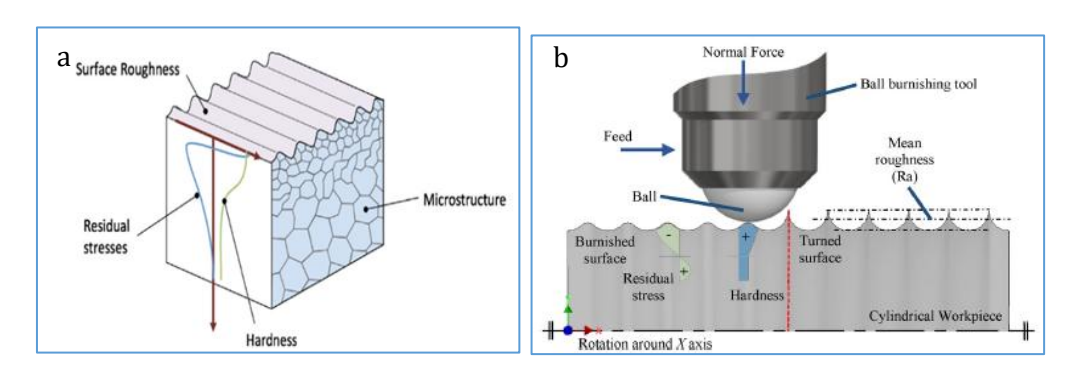


Figure 1.2: Schematic illustration of a) surface integrity parameters [16] and b) ball burnishing treatment on a cylindrical workpiece [12].

The induced compressive residual stresses on the burnished surface of the material are responsible for enhancing the fatigue strength and wear resistance of the surface layer [1]. A sample X-ray diffraction residual stress measurement method is the best measurement technique for estimating the fatigue life of engineering components. This method works using layer removal techniques in the depth profile stress-affected zone of the part. However, it requires extensive experimental effort as well as time-consuming, making it relatively expensive [14].

Instead of doing extensive experimental work, FEM modelling provides a better understanding of the effects of machining conditions on surface integrity properties, and it can predict fatigue performance of the components at minimal time and affordable cost [12], [17]. The first finite element method (FEM) as a numerical modelling approach emerged in the early 1940s. A key advancement in finite element theory for industrial applications and materials modelling was the introduction of the Zienkiewicz-Zhu error estimator, which guides adaptive mesh refinement and contributed to the theory of FEM mathematical approximation in the 1990s [18]. The finite element method (FEM) in the ball burnishing process can be 2D or 3D, which discretises the physical system either in 2D or 3D [9].

1.2. Problem Statement

Aluminium 2024 alloy is mainly used to fabricate the structural components of aircraft structures, including fuselage, wings, and other supporting structures, due to its excellent corrosion resistance, fatigue resistance, machinability and strength-to-weight ratio. However, aluminium machining often produces a poor surface finish, leading to reduced fatigue life and wear resistance of the component. These components are subjected to both high-cycle fatigue and low-cycle fatigue during service, leading to failure due to both cyclic loading and surface corrosion. The enhancement of surface integrity (especially residual stress) plays a key role in improving fatigue performance to resist surface crack initiation and propagation.

The ball burnishing process is one of the effective mechanical surface treatment methods to produce surface compressive residual stresses, which is used to extend the service life of aircraft structural components by inhibiting crack initiation and propagation. The X-ray diffraction method is commonly used to measure residual stress by profiling step by step a burnished component, but it requires extensive experimental work, time and material wastage. As an efficient alternative, a 3D FEM modelling can predict residual stress a better control of the machining conditions, minimal time and lower cost.

Predicting an accurate residual stress through the FEM modelling requires a well-discretised and fine mesh geometry. However, the excessive fine mesh significantly increases computational time and leads to the prevention of field output convergence. To address this issue, combining well-designed geometry of the ball burnishing components with a hybrid explicit–implicit FEM approach provides an effective balance between accuracy and computational efficiency for the prediction of fatigue life of Aluminium 2024 alloy components used in aircraft structural components.

1.3. Objective

The primary objective of this study is to develop an accurate 3D finite element model for the ball burnishing process applied to Aluminium 2024 alloy work material through a hybrid Explicit and Implicit approach for residual stress prediction. The numerical simulation result will serve as a good insight into a successful and sustainable Aluminium plane structure lifetime prediction for the burnished surface. The following specific objectives will be undertaken to achieve the primary goal of the current study.

- Develop a replica of the physical ball burnishing process through a dynamic Explicit FEM model by visualising a realistic ball burnishing experimental setup and working conditions.
- Validate the accuracy and stability of the dynamic explicit FEM model and conduct a detailed study of surface interaction between the burnishing tool and work material.
- Develop a static Implicit FEM modelling approach by extracting normal stress
 produced at the stable zone of the dynamic explicit FEM model, and create an
 accurate simulation by mapping normal stress on the surface of the work
 material by controlling process parameters.
- Study the effect of process parameters on residual stress produced at different
 positions of burnished work material. And validate the result using experimental
 XRD residual stress measurement data, as well as evaluate both Explicit and
 Implicit FEM model computational performance.

1.4. Significance of the study

This study demonstrates the role of Finite Element Modelling (FEM) for analysing the ball burnishing process by designing a modified part geometry and applying a hybrid Finite Element analysis method. The detailed analysis and validation of FEM model results offer a broad range of applications and confirm an effective alternative to the physical burnishing process. This provides detailed insights into the surface thermomechanical properties of burnished work material, including stress, plastic strain, and heat flux phenomena, which are difficult to measure using experimental methods. The study serves as a reference for predicting the sustainable lifetime of burnished 2024 aluminium alloy components by evaluating the induced compressive residual stress.

1.5. Scope of the study

This study focuses on numerical finite elements modelling (FEM) through a hybrid explicit and implicit approach for the ball burnishing process applied to Aluminium 2024 for residual stress prediction. The scope includes visualising a physical ball burnishing experimental setup and using the process working conditions to replicate a real process. The initial step involves developing an accurate Finite Element model (FEM) using dynamic explicit analysis to study the thermomechanical response during the interaction within a stable contact zone. After the dynamic explicit finite element analysis (FEA) burnishing process stability and accuracy are verified, a Standard/Implicit FEM modelling approach could be implemented to predict accurate residual stress based on normal stress obtained from dynamic explicit analysis.

1.6. Structure of the thesis

The current thesis work is organised into five main chapters to achieve the objectives Chapter 1: Introduction and Background

• Presents study background, problem statement, objectives, significance, and scope and limitations of the study.

Chapter 2: Literature Review

• Performs a comprehensive literature review for both physical and FEM modelling of the ball burnishing process and provides a summary of key findings with literature gaps.

Chapter 3: Methodology

• Describes the detailed procedure for the development of accurate FEM models for both dynamic explicit and standard /implicit FEM modelling approaches.

Chapter 4: Results and Discussion

 Presents the numerical simulation results and discussion of output fields for model accuracy, contact behaviour and residual stress prediction and validation.

Chapter 5: Conclusions and Future Work

 Presents a clear conclusion on the key findings and highlights the significance of working conditions on the ball burnishing process based on the results, and provides recommendations for future research work.

Chapter 2

Literature Review

In this chapter, a comprehensive review of the existing studies focusing on the ball burnishing process applied to aluminium alloy 2024 is presented for both experimental and numerical modelling approaches. The literature review in this chapter is organised into four sections: surface integrity, the fundamentals of the ball burnishing process, numerical modelling, and a summary with highlighting research gaps.

2.1. Surface integrity

Surface integrity is defined as a comprehensive property of the surface and its subsurface layers resulting from a component's manufacturing or machining. This term concerns four main fields of surface property parameters or characteristics, such as topological properties (roughness, geometric aspects, etc.), mechanical properties (microhardness, residual stresses, etc.), metallurgical properties (microstructure, grain size, etc.) and chemical composition change 15].

2.2. Fundamentals of the ball burnishing process

Ball burnishing is a cold-working surface finishing process that creates plastic deformation on the metallic workpiece by applying pressure through a very hard ball that improves its surface integrity properties [19]. The ball is made up of hard material called hardball, which can deform material from peaks to valleys of special irregularities or asperities by applying a uniform normal load [10], as shown in Figure 2.1.

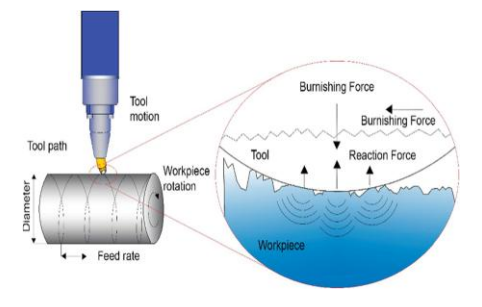


Figure 2.1: Plastic deformation phenomenon during burnishing [10]

The burnishing tool is mounted either on a CNC lathe or milling machine, where it is pressed against a workpiece under controlled machining conditions. Ball burnishing is used to enhance surface quality, such as dimension control, increase surface hardness, improve surface smoothness and induce compressive residual stress to improve component fatigue and wear of the surface layer. It is effective on smooth surfaces which has uniform asperities, mainly initial surface roughness between 2 and 5 μ m, and it can achieve dimensional accuracy within $\pm 5 \mu$ m [8].

2.2.1. Application of ball burnishing Process

Numerous industrial applications have made extensive use of the ball burnishing process for a variety of materials. The dominant workpiece materials used in ball burnishing, applicable in many industries, are steel alloy and aluminium alloy due to their favourable properties [1]. Especially, in automotive, aerospace, biomedical, and railroad industries are the most common industrial applications for the multiple materials studied in which this surface treatment is potentially used [1], [12], [20].

Some engineering components, such as shafts, press rods, and actuators, use medium carbon steel due to its mechanical characteristics and practical relevance. Tool steel, also called AISI P20, is used for large plastic injection moulding products for the automotive industry, and heat-treated steel is used for the construction of injection moulds [7]. Ball burnished chromium-nickel steels are also widely used in various industrial fields such as food, chemical, automotive, nuclear and traditional energy industries, household appliances, instrumentation, etc., due to their higher corrosion resistance [14].

Aluminium alloy is the most utilised material for the ball burnishing process used in many applications, next to steel. Currently, the automotive and aeronautic industries have a great demand for low-density materials, which can bear a high load increase [20]. A ball burnished Al 6061 utilised in automotive and aeronautics industrial applications [21]. Aluminium 2024 alloys are also applicable in the aero engine component [9] because of its excellent strength-to-weight ratio and good resistance to fatigue failure and T3 heat-treated Aluminium 2024 is widely used in fuselage construction [6].

2.2.2. Analysis of ball burnishing process parameters

The ball burnishing process has been studied in several experimental investigations aimed at identifying the most suitable parameters for a given material. Ball burnishing process parameter selection is mainly based on the recommendations of tool manufacturers and research interests.

The input parameters can be classified into deforming and productivity parameters. Burnishing force is categorised as a deforming parameter, and others, such as feed, speed, and number of passes, are part of the productivity parameter, which determines manufacturing time and cost. Among ball burnishing process parameters, some factors, such as burnishing force, have a significant effect on the generation of residual stress, whereas factors like speed exhibit comparatively low influence[22]. Among ball burnishing process parameters, burnishing force, feed rate, speed and number of tool passes are widely considered in experimental studies [1].

All ball burnishing process parameters depend on the geometry of the workpiece, which is a flat plate and a cylindrical workpiece, used on the milling and lathe machine setups, respectively. The typical ranges of most common ball burnishing parameters for different metallic materials, reporting values between 7 N and 1131 N for force, 0.1 m/min and 158 m/min for speed, and 0.01 mm/rev to 0.8 mm/rev for feed [20].

For the ball burnishing process under a cylindrical work part, where the workpiece always rotates around its axis at a defined rotating speed, and the tool is subjected to the workpiece, with a definite longitudinal displacement at the feed rate. The ball is supported in a fluid bearing with sufficient pressure to generate a ball burnishing force [16] as indicated in Figure 2.2.

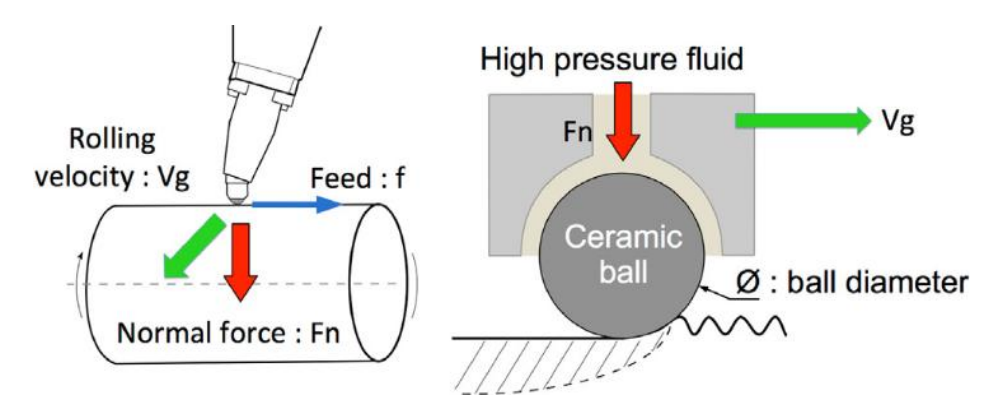


Figure 2.2: Working mechanism of the ball burnishing process [16]

A. Burnishing force

Burnishing force refers to the normal force applied by the burnishing ball onto the surface of the workpiece. This is a critical process parameter used to achieve surface property enhancement. Currently, the ball burnishing mechanism has been improved to a vibratory-assisted mechanism to allow the best control over the pressure [23]. The outcomes of higher pressure are higher plastic deformation, which has a direct effect on surface residual stress.

In a pressure-assisted ball burnishing process, a small amount of fluid is always lost along the circumferential gap between the ball and its socket. The estimated reduction of force due to this phenomenon is 11~% and in real burnishing force (Fb), the experimental angle between the ball tool and the normal to the workpieces is 15° [10]. The mathematical relationship between pressure (P) and burnishing force is given by Eq.(2.1).

$$Fb = 0.89 \frac{p \,\pi d^2}{4} * \cos 15^{\circ} \tag{2.1}$$

Where d=ball diameter, Fb =burnishing force and p = pressure

B. Burnishing speed

The linear or rotational speed of the tool or workpiece under ball burnishing operation is expressed as the burnishing speed given by m/min or rpm. In a flat surface, the ball burnishing operation, the workpiece remains stationary, but in a cylindrical surface, the ball is stationary. The effects of burnishing speed are negligible on the residual stress, but increasing burnishing speed is important to improve productivity [16].

C. Burnishing feed

Burnishing Feed (f) is the distance covered between successive tool revolutions or tool passes in ball burnishing, typically measured in (mm/rev). According to [20] literature review, higher residual stress can be obtained at low feed. The contact length of the ball on the surface of the material must be greater than the burnishing feed to produce a compressive stress.

2.2.3. Characterisation methods of residual Stress

Bragg's law forms the basis of X-ray diffraction (XRD), which is one of the most widely used non-destructive techniques for residual stress evaluation in crystalline materials. A monochromatic X-ray beam with wavelength (λ) interacts with atomic planes in a crystal lattice, and constructive interference occurs at an angle θ [8] given by Eq.(2.2)

$$2dsin\theta = n\lambda \tag{2.2}$$

Where d is the lattice spacing, and n is the diffraction order. Any accurately measurable shift in the diffraction peak position (2 θ) is used to enable the calculation of strain, and consequently residual stress, at the surface of metallic components.

The striking of X-rays on a simple crystal structure with Bragg's condition for both ray A and ray B also illustrates the diffraction geometry, where both A and B rays travel on the same path Figure 2.3.

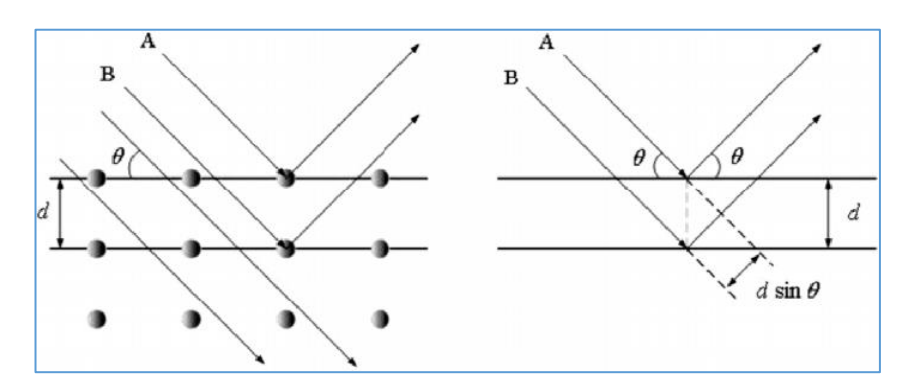


Figure 2.3: Schematic illustration of X-ray diffraction for A and B incident [8]

The residual stresses were characterised using the X-ray diffraction technique using the $\sin^2\Psi$ method following the EN15305 standard [24]. The electrolytic polishing was used to measure the depth profile of the burnished surface. This standard residual stress characterisation is performed by X RAYBOT. It utilises advanced X-ray tube and detector bandwidth positioning technologies, along with laser triangulation, for rapid and precise characterisation [25].

2.3. Finite element modelling of ball burnishing process

The finite element method (FEM) modelling is a crucial method for simulating plastic deformation produced through the burnishing process, where a hard ball is pressed against the work material at controlled machining conditions. A 3D model provides an accurate representation of the physical burnishing process, which is mainly characterised by model complexity and computational cost. Whereas, 2D FEM modelling offers a reduced computational requirement, and it does not capture the proper field output accurately [12], [17]. The most applicable software for simulating the ball burnishing process using FEM is ABAQUS, which has two main steps: pre-processing and post-processing. Pre-processing step involves creating the geometry of the burnishing tool and workpiece, assigning material properties with material behaviour law, selecting finite element analysis type (explicit or implicit), specifying a good tool-workpiece interaction, applying boundary condition and different load at reference point and defining a mesh and element type depending on the analysis.

In the postprocessing step, the software uses governing equations to compute the thermomechanical response field out such as stress, plastic strain, temperature, etc. These are then ready to be extracted for further results and discussion [12].

2.3.1. Ball burnishing part design and consideration.

In 3D FEM modelling of the ball burnishing process, the workpiece must be designed as deformable, whereas the spherical ball is designed as rigid or deformable. But in most studies, the ball is considered a rigid body due to the negligible deformation of the high hardness properties of the ball material. This approach is an effective method to reduce the model computation time [9], [26]. In the burning process, the geometry of the burnishing tool can be designed in a full sphere ball Figure 2.4a or a dome-shaped form Figure 2.4b (keeping curvature radius designed as a spherical cap) [17].

The spherical ball allows for plastic deformation by allowing both translation motion and rolling, which is used to represent the real ball burnishing process configuration. Whereas the spherical cap only allows translation and sliding motion, which is used to study the contact region, it can represent the slide burnishing process configuration and an effective approach to reduce computation time by decreasing the number of generated mesh elements. At a very low contact region and with a negligible coefficient of friction, both configurations can exhibit approximate plastic deformation and compressive residual stress.

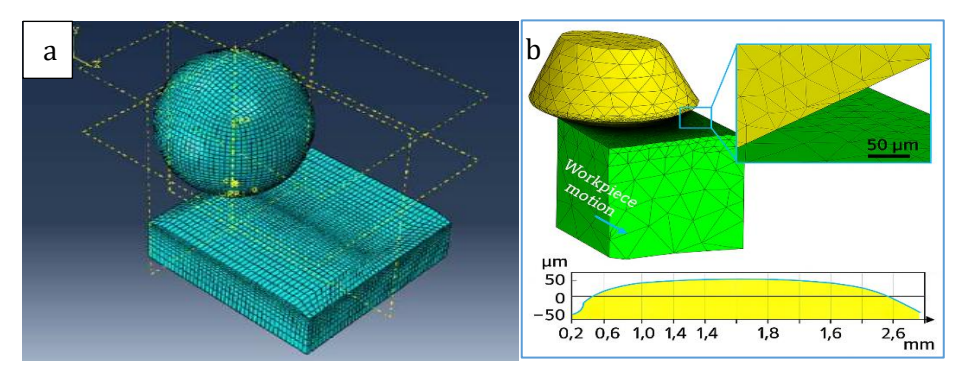


Figure 2.4 : Ball burnishing part development, a) spherical ball on plate [26] and b) a dome-shaped ball on a plate [17] configuration

Ball burnishing workpiece geometries can be a rectangular plate [26], and a cylindrical [27], depending on the experimental machining setup considerations. Burnishing through a milling machine setup, the work material is typically performed on a stationary rectangular plate, whereas in a lathe machine setup, the process is generally applied on a rotating cylindrical workpiece.

In ball burnishing FEM modelling, small cut-section part geometries can be extracted on a cylindrical bar, as indicated in Figure 2.5, which allows for assigning a fine mesh for the reduction of computation time with accurate output field prediction ([26], [27]. And the radius of curvature is negligible when a small cut section is taken from a big-diameter cylindrical bar, and the work material geometry is designed as a small plate for numerical simulation [28].

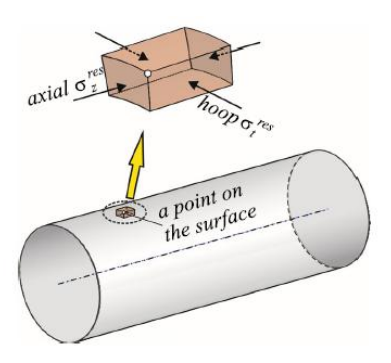


Figure 2.5 : Small cut section for FEM modelling on cylindrical workpiece [28]

2.3.2. Ball and workpiece material behaviour

In FEM modelling, accurately computing the material properties for both the ball and the workpiece is a crucial step. The ball is the critical component, made of hard material such as alumina carbide, silicon nitride, silicon carbide, cemented carbide, bearing steel, and is responsible for inducing plastic deformation on the workpiece [1], [13].

Whereas the workpiece is made of a metallic material component can exhibit elastic-plastic behaviour to create a permanent deformation. The mechanical behaviour of the workpiece material is represented by an appropriate constitutive model. For the representative mechanical behaviour model, it is necessary to perform a material characterisation to obtain a stress-deformation curve. The elastic-plastic behaviour of ball burnishing workpiece material can be represented by isotropic hardening, Johnson-Cook, Power-law and thermo-visco-plastic with Johnson-Cook [12]. The Johnson-Cook (JC) material behaviour model is widely used in modelling ball burnishing to predict residual stresses [9], [26], [29]. The Johnson-Cook model was initially developed by conducting torsion and Hopkinson bar tensile experimental tests over a wide range of temperature and strain rate for different engineering materials [30].

2.3.3. Algorithms of contact between ball and workpiece surfaces

An accurate definition of contact between the surface of the burnishing tool and work material plays a crucial role in replicating a physical process. These two components involve complex interactions during numerical simulation.

The suitable type of contact between the burnishing tool and the workpiece is the surface-to-surface at penalty contact method, defined as master and slave, respectively [25]. It allows enforcing the solver algorithm for realistic interaction properties [12]. And also, the augmented Lagrangian method is used as a contact algorithm in the simulation of the contact interaction in the ball burnishing process [31]. For a precise model interaction property, the initial surface is assumed as smooth, frictionless, low isothermal condition and a negligible burnishing speed [27]. The Hertz elastic contact theory is the best approach to analyse and estimate the contact properties between the surface of the workpiece and the burnishing tool contact region at the applied burnishing force to check the accuracy of the FEM model [32]

2.3.4. 3D FEM modelling boundary and loading conditions

In FEM modelling, an appropriate boundary condition definition is an essential step to replicate the physical behaviour of the ball burnishing process accurately. In a cylindrical workpiece, the workpiece is fixed on both sides and allows rotation around the axis of rotation, and the ball has the freedom to move the burnishing path to allow a feed during the process at an applied burnishing force [12] shown in Figure 2.6a. While in a rectangular plate, the workpiece should be constrained (encastre) at the bottom surface to fix degrees of freedom or to prevent body motion. Also, the remaining side faces should be symmetrically fixed by allowing deformation in the cut and feed direction in Figure 2.6b. The assigned reference point found on the centre of the rigid burnishing tool is responsible for applying a normal burnishing force and speed along the burnishing path [33].

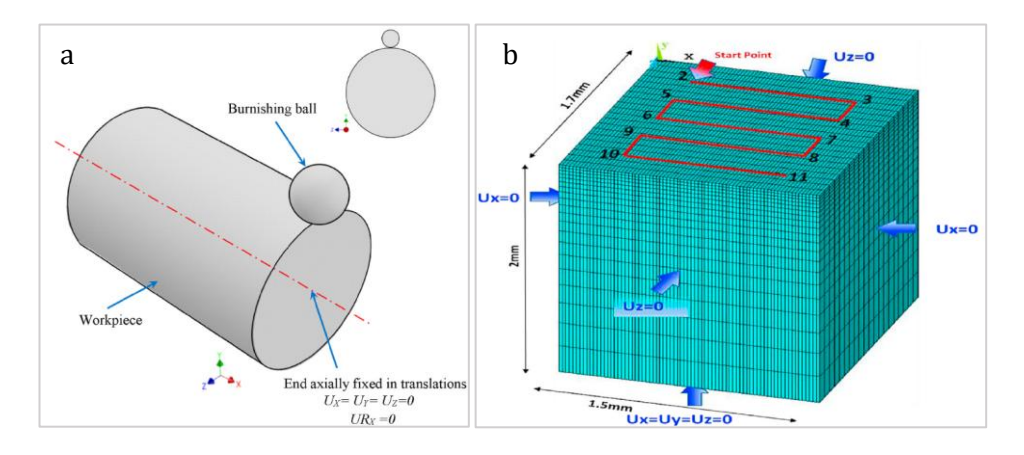


Figure 2.6: Ball burnishing boundary condition for a) cylindrical [12] and b) rectangular plate [33]

2.3.5. Finite element analysis method

In any FEM modelling, selecting an appropriate finite element analysis (FEA) method that matches the physical behaviour is the most critical step for an accurate numerical simulation. The FEA uses a direct time integration algorithm classified as Implicit time integration and Explicit time integration methods based on the equilibrium condition solving equations to get a solution at time $t + \Delta t$. To apply this direct time integration method for linear and non-linear systems, the well-known finite element governing equations [34] are given by Eq.2.3.

$$M\ddot{U} + C\dot{U} + KU = F \tag{2.3}$$

Where M, C and K represent matrices for mass, damping, and stiffness, respectively; F is a vector for the applied force, whereas \ddot{U} , \dot{U} and U are acceleration, velocity and linear displacement, respectively.

The Abaqus Standard (implicit solver) is designed for numerical simulation where systems require equilibrium at each step. It employs an implicit time integration method known as the Newton-Raphson iteration to solve equations and converge on the solution, particularly for nonlinear problems. While the Explicit solver can perform the calculation of motion directly by the known values of force without solving complex equations at every time step using the explicit time integration method [25].

The explicit FEM approach is suitable for nonlinear dynamic numerical simulation, offering a straightforward physical formulation of problems. However, it requires a smaller time increment to achieve model stability, which significantly increases the computational cost. A dynamic, coupled temperature-displacement explicit solver with automatic time incrementation is suitable for studying explicit numerical simulations. While the implicit is often preferred for solving static (structural loading, thermal steady-state) and quasi-static non-linear problems (contact or plasticity under slow loading) and employs a static, general solver with an automatic time increment suitable for capturing mechanical behaviour over large incremental time steps [25], [35].

In dynamic explicit analysis, significant errors are experienced when the time increment is too large, whereas the Standard/Implicit analysis remains stable and is not affected by the choice of time increment due to the use of an iterative approach [36] presented in Figure 2.7.

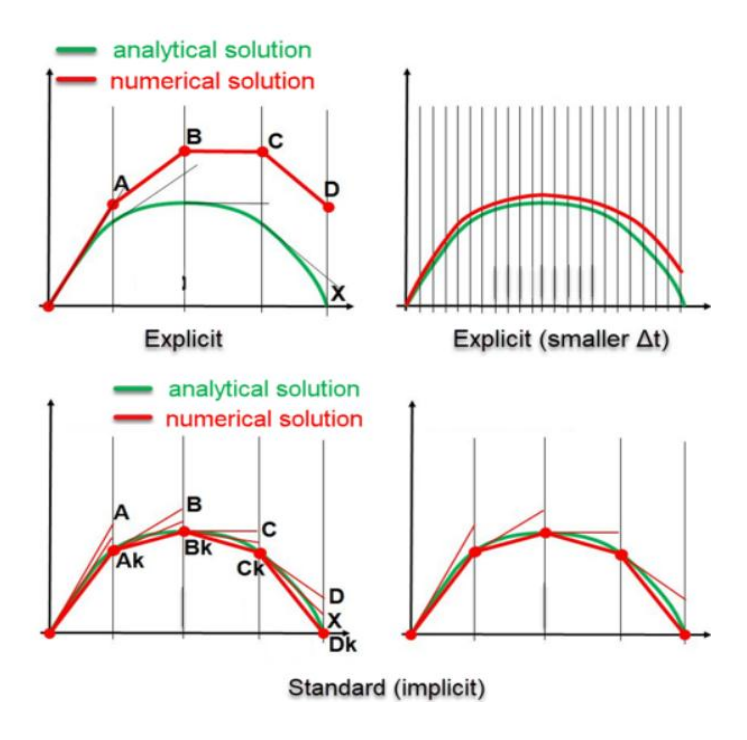


Figure 2.7: Time incrementation under explicit and implicit solvers [36]

2.3.6. FEM model discretisation strategies

The accuracy and reliability of analysing engineering structural components using finite element analysis (FEA) depend on the quality of analysis execution. The model discretisation is a crucial method to reduce the degree of freedom from infinite to finite elements. The process involves dividing the primary domain of the part into smaller subdomains, called elements, which are interconnected by nodes known as discretisation or meshing. A well-discretised fine mesh of parts plays a crucial role in determining the accuracy and computational efficiency of numerical simulations. Although fine meshes are essential for improving accuracy, the process requires more computing time [37]. In 3D FEM modelling of the ball burnishing process, a fine mesh, particularly at the contact region, is required to capture thermo-mechanical field outputs, including residual stress [29]. For both explicit and implicit analysis, a reduced integration type of element is widely used to achieve convergence with the minimum number of integration points for the finite element integrals of the stiffness matrices [12].

The most common types of elements used in FEM modelling of Ball burnishing are C3D8RT and C3D8R [9], [12], [26]. Where C3D8R is an 8-node linear brick with reduced integration and hourglass used to represent mechanical response in implicit analysis, whereas C3D8RT is applicable in a coupled temperature-displacement algorithm with reduced integration and hourglass control for dynamic explicit analysis.

2.4. Research summary and gap

The ball burnishing process is the most cost-effective and suitable superfinishing process for treating the surface of mechanical components and is particularly effective with elastoplastic metallic materials. Applicable to many industrial engineering components to improve service life. The process can be carried out on a conventional or CNC lathe or milling machine, performed after a proper turning or milling process. The process requires attention to its parameters and setup. The most governing process parameters that need consideration in the process are force, speed, and feed. Residual stress is one of the main field outputs of the ball burnishing process that forms a compressive stress on the surface or subsurface in both feed and burnishing directions. This property is responsible for fatigue resistance. Residual stress is quantified by the X-ray diffraction (XRD) technique.

Finite element modelling is an effective method for replicating a physical ball burnishing process to estimate thermal and mechanical field outputs through the finite element analysis technique. 3D FEM modelling is the most accurate approach for modelling ball burnishing and estimating residual stress, and ABAQUS finite element analysis software is the most powerful for simulating the process. Among all constitutive material behaviour laws, the Johnson-Cook model is the most powerful in capturing both mechanical and thermal field outputs. A surface-to-surface contact method is a practical approach for analysing the interaction behaviour of the contact region between the ball and the workpiece [25]. The burnishing tool is typically modelled as a rigid body, while the workpiece material is the primary focus of the analysis. A well-discretised mesh of parts plays a crucial role in determining the accuracy and computation time of numerical simulation in finite element modelling. Generally, the burnishing force, tool pass, and depth of penetration have a direct impact on generating compressive residual stress. The effects of working conditions for surface integrity during the experimental ball burnishing process and the finite element method (FEM) ball burnishing approach are summarised in Table 2.1 and Table 2.2 respectively.

Despite extensive literature studies, the research gap lies in FEM modelling of the ball burnishing process, particularly in the use of precise and well-discretised fine mesh size, modified burnishing tools, the comparison of tool sliding with physical tool rolling conditions, simulations on aerospace-grade Aluminium 2024 alloy, and the implementation of a combined dynamic explicit-implicit approach.

| Work Material | Ball | BB condition | Finding | Author |
|-----------------|-----------|--------------------|--------------------------|----------|
| | material | | | |
| 15-5PH | SiN | Fb: 150-300N | Rs improved by force | [16] |
| martensitic | Ceramic | V: 10-100 m/min | and pass, but the effect | |
| stainless steel | | fr: 0.05-0.2mm/r | of speed is negligible | |
| | | Pass: 1,2,3 | | |
| Al 2024-T3 | R6M5 tool | Fb: 400-1300N | Fatigue life improved | [38] |
| | steel | V: 63m/min | by 38.4%, and | |
| | | fr: 0.05 | compressive Rs was | |
| | | | introduced | |
| EN AW-2024-T3 | diamond | F: 40-60N | Traverse stresses are | [39] |
| | | fr: 0.5-1.5m/min | -130 MPa and | |
| | | | longitudinal stresses | |
| | | | are –242 MPa. | |
| 15-5PH | Ceramic | Fb: 80N | Surface Deep | [24] |
| martensitic | | V: 50m/min | compressive Rs | |
| stainless steel | | fr: 0.11mm/rev | achieved -620 Mpa | |
| Al 2024 alloy | Tungsten | Fb: 15.16 - 30.32N | Improves surface | [40] |
| | carbide | No, Pass:1-3 | compressive with force | . |
| | | | and pass. | |
| AISI 316Ti | Diamond | Fb: 50 -250N | Higher Compressive | [14] |
| austenitic | tip | V: 50, 250m/min | stress induced at high | |
| stainless steel | | fr: 0.02 to | force and low speed | |
| | | 0.1mm/rev | and fatigue life is | |
| | | | improved | |

Table 2.1: Literature summary for the experimental ball burnishing process

| Work | Material | Woking | Element | Finding | Author |
|----------------|---------------|----------------|----------|-------------------------|--------|
| Material | Constitutive | condition | type | | |
| | Model | | | | |
| Al 2024 T3 | kinematic | Fb: 800-1300 N | C3D8R | Compressive axial and | [28] |
| | hardening | V: 63m/min | | hoop residual stresses. | |
| | | f: 0.11mm/rev | | | |
| Ti-6Al-7Nb | Isotropic | P:100-300 bar | C3D8R | High compressive Rs | [27] |
| | hardening | f: 0.2mm/rev | | at high pressures | |
| AISI 1038 | Power law | Fb: 270N | SOLID186 | Residual stress | [31] |
| Steel | | Cof: 0-0.3 | | increased with Cof. | |
| AA6061-T6 | Johnson-Cook | Fb: 20-40N | C3D8R | Rs: -217 MPa at | [26] |
| | | f: 1-1.5m/min | | ultrasonic and -163 | |
| | | Va: 0-10µm | | MPa at conventional. | |
| Al Alloy 7075 | -Johnson-Cook | Fb: 150-600N | C3D8R | Rs increased with | [29] |
| T651 | | f: 0.1mm/r | | applied force | |
| | | ω: 240rpm | | | |
| Al 2024 | No specific | P: 10,15,20MPa | C3D8R | Rs increased with | [9] |
| | model | Pass: 1 -3 | | pressure and pass | |
| Stainless Stee | Power-law | Fb: 270, 470 N | - | Accurately predicted | [33] |
| | | fr: 0.6m/min | | Rs trends. | |
| AISI 4140 | Johnson-Cook | P: 30 Mpa | C3D8T | Compressive RS | [41] |
| steel | | db:13mm | | affected a depth of | |
| | | f: 1mm | | 2.7mm. | |
| AISI 52100 | Custom flow | P: 40MPa | _ | Induces compressive | [42] |
| | stress model | V:100m/min | | Rs and improved | |
| | | fr: 0.06mm/rev | | surface integrity | |
| AA2024- | Johnson-Cook | Bd: 6-40 μm; | C3D8R | Higher Bd depth | [43] |
| T351 | | ω: 40000 rpm. | C3D4 | creates higher | |
| | | V: 40 mm/min | | compressive Rs | |

Table 2.2 : Literature summary for the 3D finite element modelling of the ball burnishing process

Chapter 3

Methodology

This chapter presents a comprehensive methodological framework for simulating the ball burnishing process using 3D finite element modelling (FEM) techniques. A physical experimental setup provided the foundation for designing the component geometry. Studying component material properties and understanding the experimental setup are the first two crucial steps in establishing the model's foundation. The chapter then proceeds to the systematic development of FEM in Abaqus finite element analysis software, starting with the creation of an appropriate conceptual design for the part geometry, the computation of material properties using a consistent unit system, and the selection of a suitable simulation method. As a critical aspect, it is necessary to define an appropriate material behaviour model, as well as the properties of contact or interaction, boundary conditions, loading conditions, and mesh strategies, to ensure an accurate FEM simulation environment. Finally, the chapter incorporates simulation field output extraction and model modification techniques, which support analysis and interpretation of simulation results.

3.1. Material

The ball burnishing process consists of two components: the burnishing tool and the work material. An accurate computation of material properties for both ball burnishing components is the crucial initial step for numerical simulation of the process. The thermomechanical properties of both the Aluminium 2024 alloy work material and the burnishing tool material used for the current study were kindly provided by Solis Garduno Rosalinda, a PhD researcher at LTDS.

3.1.1. Ball Burnishing tool material

The deforming ball burnishing tool, known as Eco-roll hydrostatic (HG6), with a 6 mm ball diameter made of tungsten carbide, is used by the ECL-ENISE LTDS workshop. For finite element modelling, the tool is considered as a rigid body, because its hardness is much harder than the work material, and its deformation is almost negligible.

Although the tool is considered a rigid body, it is necessary to compute into the software the material properties of the burnishing tool material, shown in Table 3.1

| Tungsten carbide | Unit |
|--|--------|
| Density, ρ (kg/m³) | 14600 |
| Youngs Modulus, E (MPa) | 620000 |
| Poisson's Ratio, ϑ | 0.235 |
| Thermal conductivity, λ ($W\cdot m^{-1}\cdot {}^{\circ}C^{-1}$) | 110 |
| Specific heat, C_p ($\mathbf{W} \cdot kg^{-1} \cdot {}^{\circ}C^{-1}$) | 288 |

Table 3.1: Material properties of tungsten carbide [44]

3.1.2. Ball burnishing work material

In this FEM modelling of the ball burnishing process on Aluminium 2024 alloy work material (Appendix A) proposed by LTDS researcher, who is currently working in the LTDS laboratory [45]. The composition properties of the material are presented in Table 3.2.

| Element | Si | Fe | Cu | Mn | Mg | Cr | Zn | Ti | Ti+Zr |
|---------|------|------|-----|------|-----|------|------|------|-------|
| wt.% | 0.15 | 0.21 | 4.3 | 0.72 | 1.3 | 0.05 | 0.15 | 0.04 | 0.05 |

Table 3.2: Chemical composition of AA2024 alloy

The material properties of Aluminium 2024 alloy at roo temperature, which were compiled from various findings and proposed by an LTDS PhD researcher, are summarised in Table 3.3.

| Aluminium 2024 alloy | Unit | Source |
|---|-----------------------|--------|
| Youngs Modulus, E (MPa) | 72400 | [46] |
| Poisson's Ratio, ϑ | 0.33 | |
| Density, ρ (kg/m ³) | 2770 | [47] |
| Thermal conductivity, λ (W. m^{-1} . ${}^{\circ}C^{-1}$) | 121.1 | |
| Specific heat, c_p (W. $kg^{-1} \circ C^{-1}$) | 877 | |
| Thermal expansion coefficient, α (° C^{-1}) | 2.23×10 ⁻⁵ | [48] |

Table 3.3: Material properties of aluminium 2024 alloy

3.2. Ball burnishing Experimental setup

Before starting FEM modelling of the ball burnishing process, it is necessary to observe a real machining setup, including the working axis, loading strategy, lubrication system, fixed position, etc., in addition to the machining conditions. Ecole centrale de Lyon, ENISE laboratory work workshops called LTDS, are equipped with a multipurpose CNC lathe machine called CMZ TC 20 YS for the ball burnishing process [45] Figure 3.1a. The ball burnishing machine setup works with the ECOROLL system, consisting of a high-pressure supply pump plugged into an Eco-roll hydrostatic burnishing ball with a lubrication system of water-miscible Betronol EP, 5 %. The machine setup enables modification of machining conditions, such as hydrostatic pressure (p), burnishing speed (V), feed rate (f), and burnishing force, which are controlled by a dynamometer. It works with a turned cylindrical workpiece supported between two chucks of a lathe, allowing it to rotate. Whereas the ball can press the workpiece perpendicular to its rotation axis with some tool inclination, as shown Figure 3.1b.

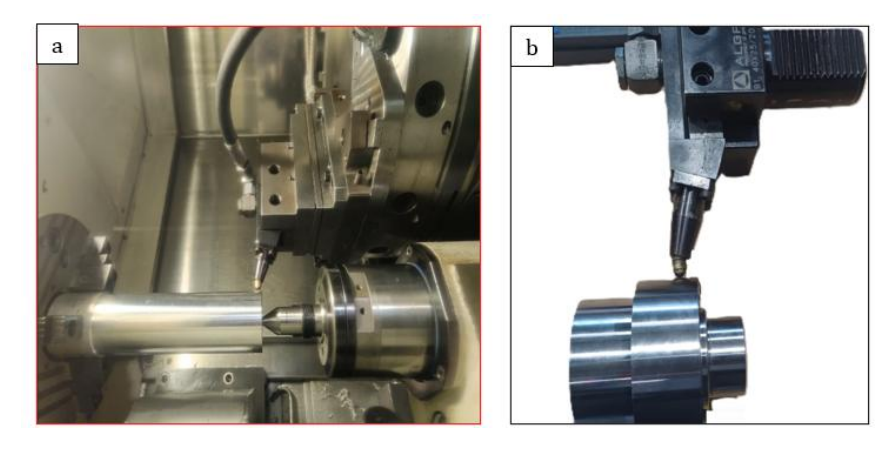


Figure 3.1 : ECL ENISE workshop, a) CNC lathe ball burnishing experimental setup and b) tool workpiece contact [45]

3.3. Finite element modelling of ball burnishing

A commercial Abaqus/2024 HF3 [45] finite element analysis software was used to perform numerical simulations for the present study. The finite element method aims to replicate a physical ball burnishing process, and to investigate the thermo-mechanical behaviour of the tool-workpiece interface as well as throughout the depth of the workpiece.

The numerical simulation aimed to replicate the physical ball burnishing process and to investigate the thermo-mechanical behaviour at the tool–workpiece interface as well as throughout the depth of the workpiece. To achieve this aim, the analysis employs a hybrid dynamic explicit and Standard/Implicit FEM approach for the entire process. This two-step numerical simulation approach ensures both model accuracy and computational efficiency [35].

An Explicit solver is suitable for simulating fast nonlinear or dynamic problems. The FEM modelling of the burnishing process provides a straightforward replication of the physical ball burnishing process at a small time increment for model stability. In the present study, Abaqus/Explicit dynamic analysis was employed to simulate a real ball burnishing process on Aluminium 2024 alloy, aiming to investigate the effect of working parameters and conditions on the interface. A dynamic temperature-displacement explicit solver with an automatic time increment was selected to study the numerical simulation of the ball burnishing process. This FEM approach was chosen to verify the model stability and material flow characteristics during plastic deformation under the physical interaction between the burnishing tool and the work material. It is more appropriate to capture the nonlinear thermo-mechanical behaviour. It enables the study of the effect of ball burnishing process parameters on key field outputs such as reaction force, penetration force, contact length, pressure, normal stress, shear stress, temperature distribution, heat flux, etc, during interaction. It is also used to extract normal stress (S33) produced on the stable region of Explicit analysis based on each surface element ID at the integration point for the input of Standard/Implicit analysis.

The implicit finite element analysis utilises implicit time integration to solve the equation governing contact behaviour under slow loading, allowing for large time increments and making it efficient for long process computations. When the number of passes increased during the burnishing process, the required time to compute increased.

This situation cannot be accomplished through an explicit analysis because of numerous increments. Due to this issue, a standard implicit approach was developed after computing the dynamic explicit model based on the normal stress input data extracted from the explicit analysis to study residual stress distribution. A static, general solver with an automatic time increment was used to study numerical simulation for capturing only mechanical behaviour after checking the thermal condition. The following section presents a detailed procedure for numerical simulation for Abaqus Explicit and Standard (Implicit) solvers.

3.3.1. Working condition and material property computation

The working conditions, including applied force, feed, speed, mesh size, and friction behaviour, were selected based on the comprehensive literature review. It proves that burnishing force was the most critical and influential deforming parameter. Then, only the force variations are considered, and the remaining process parameter is constant. Specifically, the burnishing force (257N), speed, ball diameter, feed, work material diameter, and friction condition were proposed by LTDS researchers based on the physical process presented Table 3.4. A frictionless condition arises from the assumption of machining with proper lubrication and a burnishing process on a smooth, turned surface.

| Working condition | Unit |
|-------------------------------------|------------------|
| Force, Fb (N) | 275, 348 and 420 |
| Feed rate, f (mm/rev) | 0.16 |
| Speed, V (m/min) | 80 |
| Ball diameter, d (mm) | 6 |
| Workpiece diameter, D (mm) | 60 |
| Friction condition | Frictionless |
| Taylor-Quinney Coefficient (TQC), β | 0.85 |

Table 3.4: Working conditions for FEM modelling of the ball burnishing process

Abaqus software does not have a predefined unit designation system, but it requires the use of a consistent unit designation throughout the model. For the current study, material properties, including part geometries, loads, and time, are expressed using a consistent unit system based on millimetres (mm), Newtons (N), seconds (s), and Megapascals (MPa) unit designation. This unit system ensures accurate numerical simulation results without unit conversion. Additionally, predefined constant material properties, such as the absolute zero temperature, Stefan-Boltzmann constant, and universal gas constant, are defined. The work material properties were described as temperature-dependent and used for both explicit and implicit analyses (Appendix B).

3.3.2. Part geometry design and assumptions

The first step in finite element modelling (FEM) for dynamic explicit analysis was designing a proper geometry of the ball burnishing process by visualising a real experimental setup Figure 3.1 and working conditions. It is not efficient to use a physical ball burnishing with exact part geometry (6 mm ball and 60 mm cylindrical sample) due to the time increment limitation and inaccurate results. Therefore, the geometry of the part must be modified to consider an accurate result with less computation time. Since the diameter of the workpiece is much higher than the diameter of the burnishing tool. Then, a small cut section of a rectangular plate was taken from a large cylindrical workpiece based on [28] consideration, and its curvature was neglected Figure 3.2.

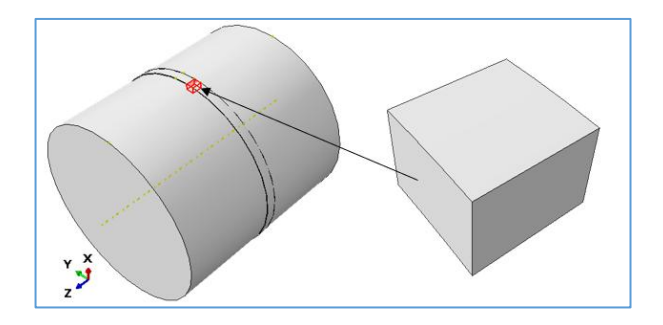


Figure 3.2: A rectangular cut section on a cylindrical workpiece

After a lot of trial and error of model stability, mesh size and computation time, the optimal final geometry of the work material was $(1.6 \times 3.66 \times 1)mm^3$ in Figure 3.3a, and $(5 \times 6 \times 1)mm^3$ Figure 3.4a for tool sliding (TS) and tool rolling (TR) conditions, respectively, for dynamic explicit analysis. And also, the work material geometry used for implicit analysis is $(2.44 \times 1.4 \times 1)mm^3$ a shown Figure 3.10.

The design of the burnishing tool geometry for finite element modelling of the ball burnishing process requires attention to define the physical phenomenon during the process accurately. According to the literature investigation, a modified burnishing tool (for a diamond tip) and a spherical ball were implemented to replicate the real burnishing process. The recent burnishing process primarily utilises a pressure-assisted ECOROLL system, which includes machines located in the LTDS laboratory.

It uses a spherical ball with roller conditions, and most literature findings use a spherical physical ball geometry for the FEM part geometry. Due to this, both tool sliding (proposed by the LTDS researcher) and the tool rolling condition (as supported in the literature and by the ECOROLL system) are considered.

A 3mm radius of curvature spherical cap burnishing tool presented in Figure 3.3b for ball sliding configuration was designed based on [44] part development approach. The following assumptions are considered for the slide burnishing condition.

- If the ball has no freedom to rotate during the process, especially when it is made from expensive, hard and brittle diamond.
- A large ball moves along a very short cut section of workpiece with a short path; the ball may not rotate much due to the small arc length in localised burnishing.
- If the workpiece moves faster than the ball, it results in the ball being dragged across the surface. It means that the ball has no time to rotate.
- Ball burnishing on ultra-smooth surfaces with a frictionless condition, a freerotating ball may not create enough torque to start rolling.

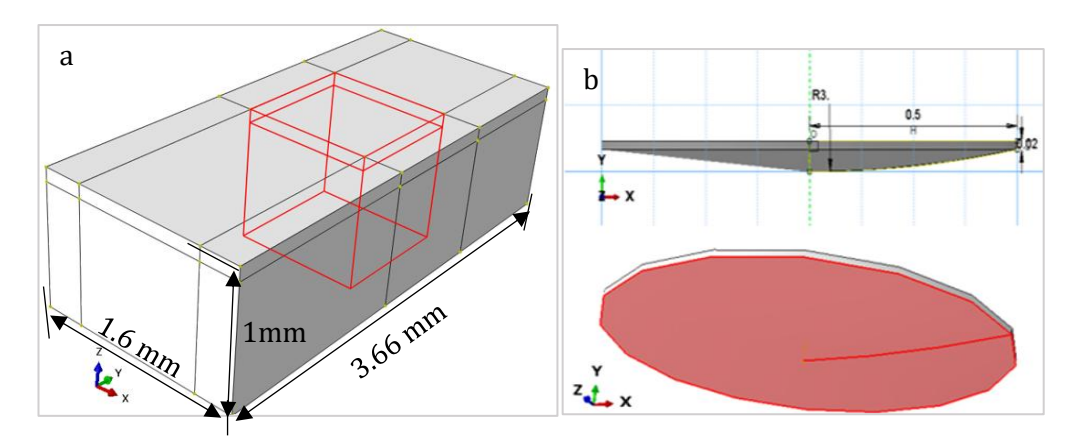


Figure 3.3: Explicit analysis part geometry design a) rectangular plate workpiece, b) 2D and 3D spherical cap burnishing tool.

Also, a full 6mm spherical ball Figure 3.4b was designed to replicate the recent real experimental roller burnishing setup and uses only 348N burnishing force to study the effect of tool rolling and sliding conditions.

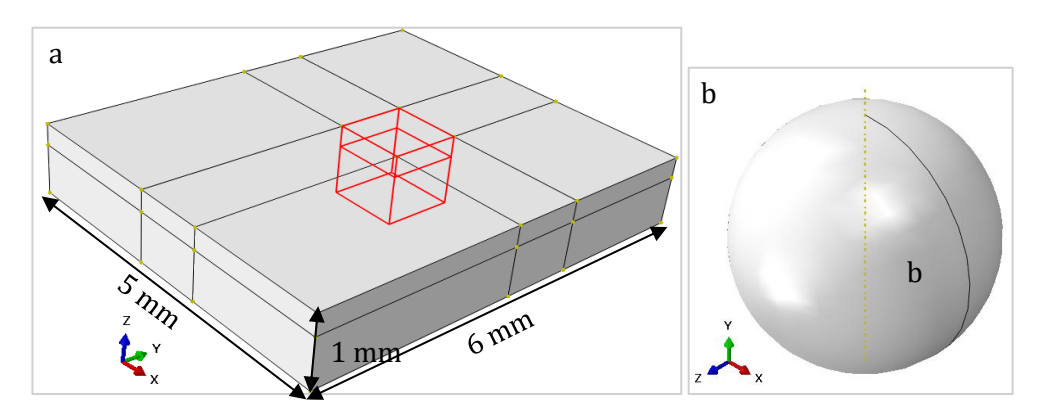


Figure 3.4: Dynamic explicit analysis part geometry design a) rectangular plate workpiece, b) 3D spherical ball burnishing tool

3.3.3. Constitutive Behaviour law of aluminium 2024 alloy

Among different types of material behaviour laws, the Johnson-Cook (JC) material constitutive model was used for the current FEM modelling of the ball burnishing process, which is also used by different Aluminium alloy FEM ball burnishing studies[26], [29], [43]. The flow stress of the IC model is given by the product of three main parts: work hardening, strain rate strengthening, and thermal softening of the material [43], given by Eq.(3.1).

$$\sigma = (A + B\epsilon^{n}) \left(1 + C \ln \left(\frac{\dot{\epsilon}}{\dot{\epsilon}_{o}} \right) \right) \left(1 - \left(\frac{T - T_{\text{room}}}{T_{\text{melt}} - T_{\text{room}}} \right)^{m} \right)$$
(3.1)

Where A, B, n, and ε describe the material's strain hardening characteristics at the reference temperature and reference strain rate for quasi-static yield strength, strain hardening coefficient, strain hardening index and strain, respectively. The second main part of JC is called strain rate strengthening, consisting of parameters such as strain rate constant (C), strain rate ($\dot{\varepsilon}$) and reference strain rate ($\dot{\varepsilon}_o$). The last main part is thermal softening, which captures the thermal behaviour involving the melting point (T_{melt}), room temperature (T_{room}) and softening constant (m).

The work done during the plastic deformation of the material is partially stored as a result of microstructural changes and partially converted into heat. The material softening behaviour depends on both heat generation and conduction during plastic deformation [49], defined by Eq.(3.2).

$$\frac{\partial T(x,t)}{\partial t} = \frac{1}{\rho C p} \left\{ \nabla \cdot \left(k \cdot \nabla \left(T(x,t) \right) \right) + \dot{q} \right\} \tag{3.2}$$

The internal heat source of solid bodies can be described by plastic work and defined by the following Eq. (3.3).

$$\dot{q} = \beta \sigma_{\rm v} \, \dot{\varepsilon}_{\rm p} \tag{3.3}$$

In Aluminium 2024, under the constitutive material model developed by JC at low temperatures, ball burnishing heat conduction is ignored, and heat generation is solely the result of plastic work, as implemented in Eq. (3.4).

$$\frac{\partial T(x,t)}{\partial t} = \frac{1}{\rho C p} \int q \, dt = \frac{1}{\rho C p} \int \beta \sigma_y \dot{\varepsilon}_p \, dt \tag{3.4}$$

Where ρ is the density, Cp is the heat capacity, k is the heat conductivity, T is the temperature, \dot{q} is the rate of the internal heat sources per unit volume, σ_y is the flow stress, $\dot{\epsilon}_p$ is the rate of the plastic strain, and β is the Taylor-Quinney Coefficient (TQC), which describes the percentage of plastic work converted into heat energy

Based on the material certificate presented in (Appendix A) the material exhibits good machinability and strength, making it a reliable choice for aerospace applications. A T3511 type of heat treatment is called stress-relieving by stretching, and the strengthened material ensures dimensional stability. Although the Johnson-Cook model was not experimentally validated, the Johnson-Cook parameters for Aluminium 2024 alloy were determined by investigating literature-related materials presented in Table 3.5. The LTDS researchers proposed those JC parameters for use in the current study without experimental validation.

| A (MPa) | В (МРа) | n | С | m | $\dot{\varepsilon}_o(s^{-1})$ | T _{melt} (°C) | T (°C) |
|---------|---------|------|--------|---|-------------------------------|------------------------|--------|
| 435.6 | 471 | 0.42 | 0.0083 | 1 | 1 | 520 | 20 |

Table 3.5. Johnson Cook parameter for Aluminium 2024 [48], [50].

3.3.4. Burnishing tool and work material Contact mechanics

For dynamic explicit analysis, a surface-to-surface hard contact between the burnishing tool and the work material is presented in Figure 3.6 with the penalty contact method was utilised. The outer surface of the burnishing tool is assigned as master, and the contact surface of the workpiece is designated as the slave to enforce the solver algorithm for realistic interaction. The analytical estimation of contact dimension, including contact length (a), penetration depth (δ) and maximum pressure (Po), presented in the Figure 3.5, was analysed through Hertz's elastic contact theory (HCT). The mathematical expression based on material properties and geometry of burnishing components at an applied burnishing force for HCT[41] is illustrated Eq. (3.5) to (3.9).

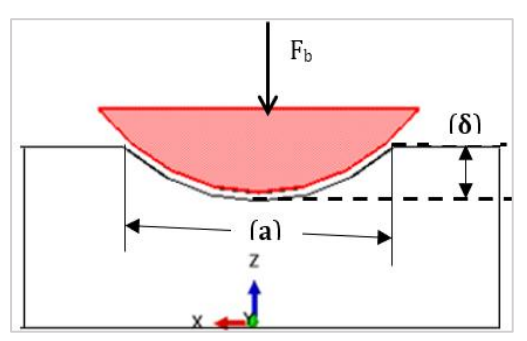


Figure 3.5 : Schematic illustration for Hertz contact theory

$$2a = 2(\frac{3F_bR^*}{4F^*})^{\frac{1}{3}}$$
 (3.5)

$$E^* = \left(\frac{1 - \theta_{WP}^2}{E_{WP}} + \frac{1 - \theta_{ball}^2}{E_{ball}}\right)^{-1}$$
 (3.6)

$$\frac{1}{R^*} = \left(\frac{1}{R_{WP}} + \frac{1}{R_{hall}}\right)$$
 (3.7)

$$Po = \frac{3F_b}{2\pi a^2}$$
 (3.8)

$$\delta = \frac{a^2}{R_{\text{ball}}} \tag{3.9}$$

Where: Fb is the applied ball burnishing force, R_{wp} and R_{ball} are the radius of the cylindrical workpiece and spherical ball assumption, respectively, while E and ϑ represent Young's modulus (E) and Poisson's ratio (ϑ) of both workpiece and ball components. In addition, E* and R* are the effective Young's modulus and effective radius, respectively.

The analytical estimation of the contact dimension, the contact length exceeds the feed. This implies that there is an overlap during the conservative tool pass. The higher overlap is beneficial for creating a smooth surface finish and uniform surface residual stress, but it requires more computation time. The percentage of overlap between tool passes given by Eq.(3.10).

Overlap % =
$$\frac{L_c - f}{L_c} \times 100$$
 (3.10)

The HCT estimation for contact dimension, maximum pressure, and percentage of overlap is presented in the Table 3.6.

| Burnishing | Contact length (mm |) Penetration | Maximum | Percentage of |
|------------|--------------------|---------------|----------------|---------------|
| force (N) | | depth (mm) | pressure (MPa) | overlap (%) |
| 275 | 0.396 | 0.014 | 3346 | 59.6 |
| 348 | 0.427 | 0.017 | 3605 | 62.5 |
| 420 | 0.458 | 0.019 | 3863 | 65.1 |

Table 3.6: HCT estimation of contact dimension and pressure

3.3.5. Loading strategies for dynamic explicit analysis

Accurate loading representations are also a crucial step in Finite Element Modelling (FEM). The predefined temperature of the burnishing tool and work material bodies was set at 20 °C, and working conditions, such as burnishing force (Fb) and speed, were applied directly at the centre reference point of the burnishing tool. At the initial dynamic loading condition for the process was unstable. To overcome this phenomenon, the load is increased by a small fraction of time using tabular amplitude to allow non-instantaneous loading. The burnishing tool moves at a speed of (80m/min) on the stationary surface of the workpiece. Figure 3.6. All the distance for burnishing was controlled by using a speed at a 2ms step period for tool sliding and 3ms for the tool rolling condition.

The other most crucial working condition was the feed, which is only applicable to define multi-revolution FEM modelling of physical burnishing. A multi-revolution assumption numerical simulation was studied, including cooling and loading/unloading considerations in Explicit analysis. Due to the higher step time requirement, the dynamic explicit model was not, and Abaqus software does not execute more than three revolutions. Then, only one revolution simulation was simulated successfully.

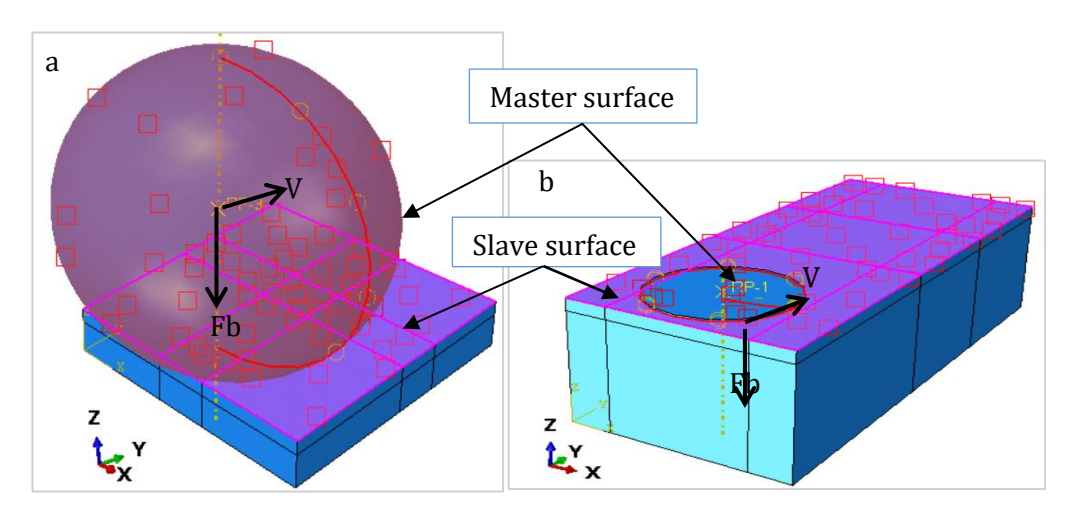


Figure 3.6 : Surface-to-surface contact between the ball and workpiece and Explicit loading strategies a) tool rolling and b) sliding condition

3.3.6. Loading strategies for standard/implicit analysis

After dynamic explicit analysis, the implicit method was introduced to analyse the FEM model at quasi-static conditions, involving a long-time computation.

Additionally, the Explicit analysis confirms that the generated temperature was very low, indicating that it does not significantly affect the residual stress. Therefore, the time required for a complete revolution for cooling was reduced, and only mechanical-based Standard/Implicit analysis was introduced. In the case of standard/implicit analysis, the loading strategies differ significantly from those in dynamic modelling. There is no direct force applied using a burnishing tool; instead, the extracted pressure (S33 over time) was applied to the surface of the work material. Figure 3.8b. This is done by creating an element set for each element ID on the surface, then the pressure magnitude (-1), and making a link with the amplitude of the extracted normal stress value. The tabular amplitude was correctly defined by considering the speed of the burnishing tool movement. A step time of 1.675 ms was required for one pass, considering an 80m/min burnishing speed.

The feed (0.16mm/s) was also controlled by escaping eight elements (each element has a 0.02 mm size) after finishing the first pass. When feed is implemented, there is always an overlap (when feed is less than contact length), which is a portion of the contact zone that is re-burnished by successive passes. All these loading strategies were implemented using INP file modification techniques through verified Python scripting (Appendix C) with Visual Studio Code software, as illustrated in the flowchart shown in Figure 3.7.

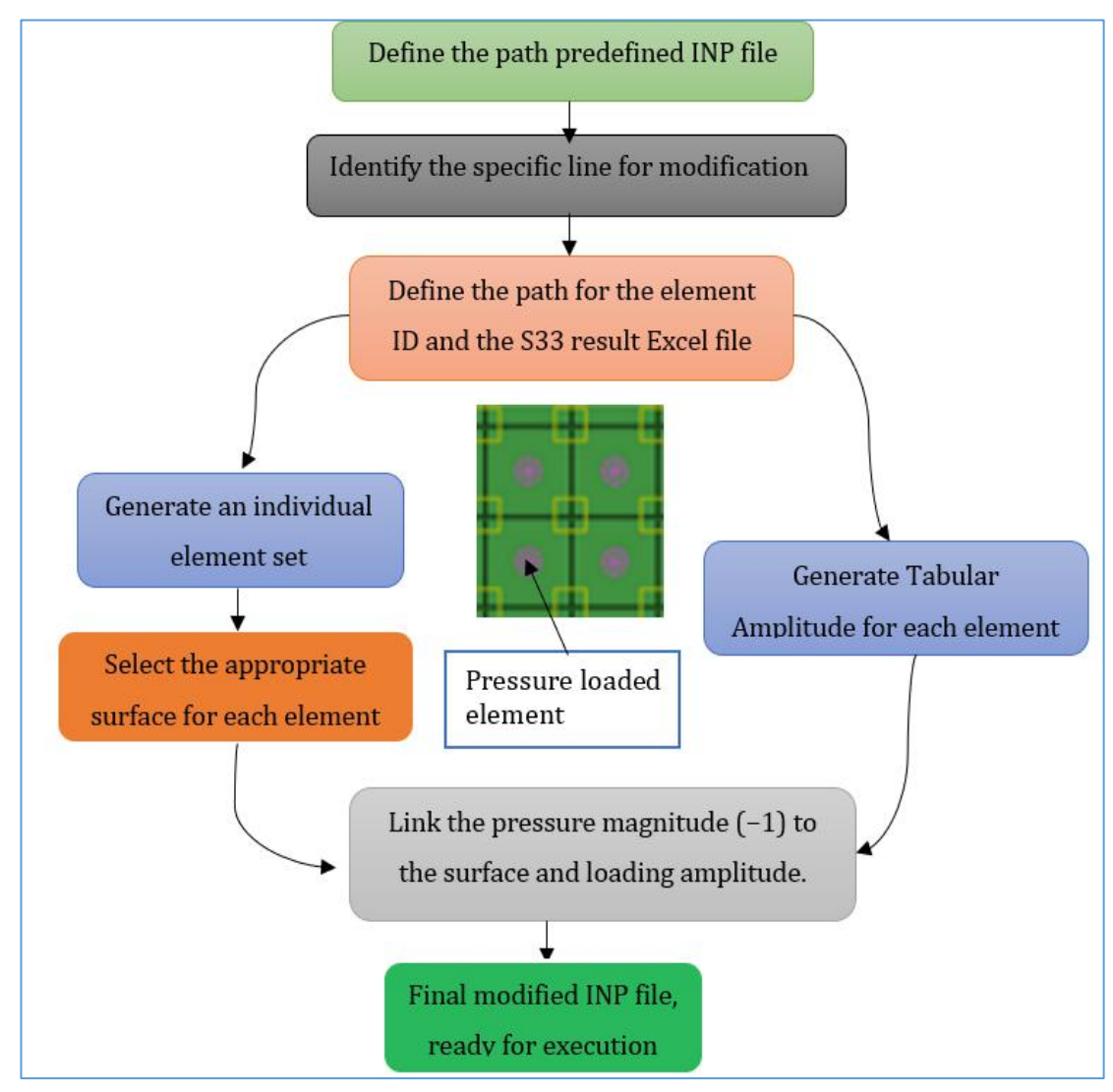


Figure 3.7: INP file modification flow chart for the implicit analysis loading

Finally, a total of 3,500 tabular amplitudes and 35,000 elements were pressurised on the surface of the work material for 10 tool passes and 12 steps, as shown in Figure 3.8.

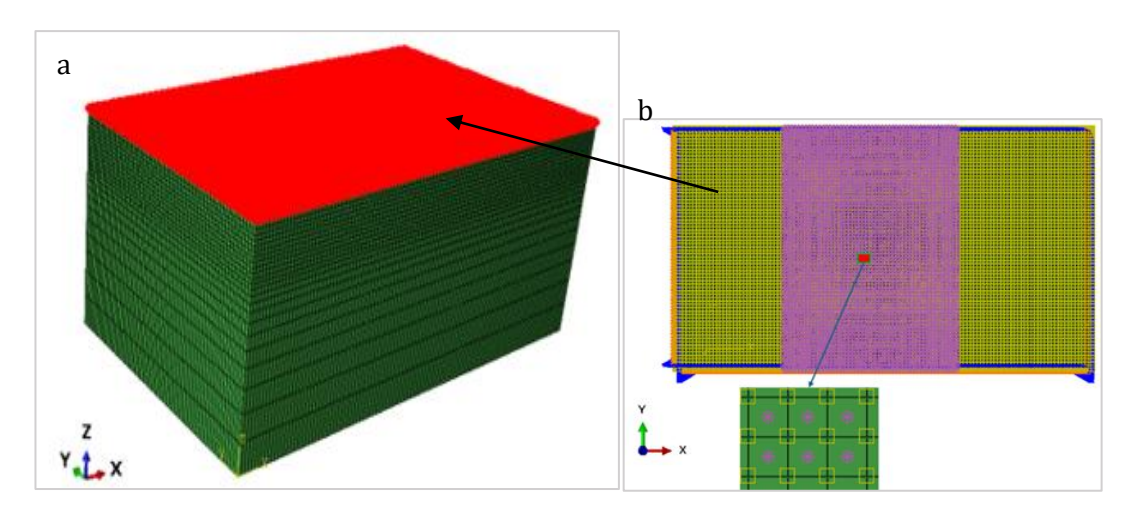


Figure 3.8: Standard/Implicit FEM modelling loading strategies, a) 3D part with proper mesh and b) 2D surface with pressure load for one tool pass.

3.3.7. Boundary condition

In Finite Element modelling, applying a proper boundary condition is the crucial step to represent a physical constraint within numerical simulation. The rectangular plate workpiece should be constrained properly to replicate a real clamping or supporting condition. For both Explicit and Implicit analysis, the bottom surface of the workpiece should be fully encastre (all linear and rotational degrees of freedom should be zero), and the remaining side face constrained symmetrically (use of XSYMM and YSYMM for surface plane perpendicular to X and Y plane, respectively) [51]. The symmetric boundary condition allows deformation in the z-axis, but it can restrict the motion in the X and Y axes, including a rotation constraint, as shown in Figure 3.9 and Figure 3.10 for Explicit and Implicit analysis methods, respectively. These types of boundary conditions are suitable for ensuring an accurate and stable numerical simulation and are used for both Explicit and Implicit FEM modelling approaches.

3.3.8. Meshing strategy

Obtaining a suitable mesh size was one of the primary challenges, which required numerous numerical simulation trials. When we use fine mesh, the accuracy of the output field would be good, but it needs more computation time. Whereas modelling with a coarse mesh, the results get inaccurate, but it requires low computation time.

For a dynamic explicit FEM model, a 3D 8-node linear brick element with reduced integration (C3D8RT) is employed, which is designed explicitly for coupled thermomechanical simulations. These types of element categories, under the Coupled Temperature–Displacement family, can allow for the simultaneous computation of thermal and mechanical fields. The optimum fine mesh size, determined after numerous tests, is 0.02mm for the burnishing tool and workpiece contact region. To reduce computation time, a mesh size increment method is applied when it is far from the contact region. For large workpieces, geometry designed for tool rolling considerations, the total generated elements were 277,424, with mesh size increments ranging from 0.020mm to 0.8mm, as presented in Figure 3.9a. And for the tool sliding assumption, 232,962 elements were generated with the mesh size increment increased from 0.02mm to 0.12mm, as shown in Figure 3.9b.

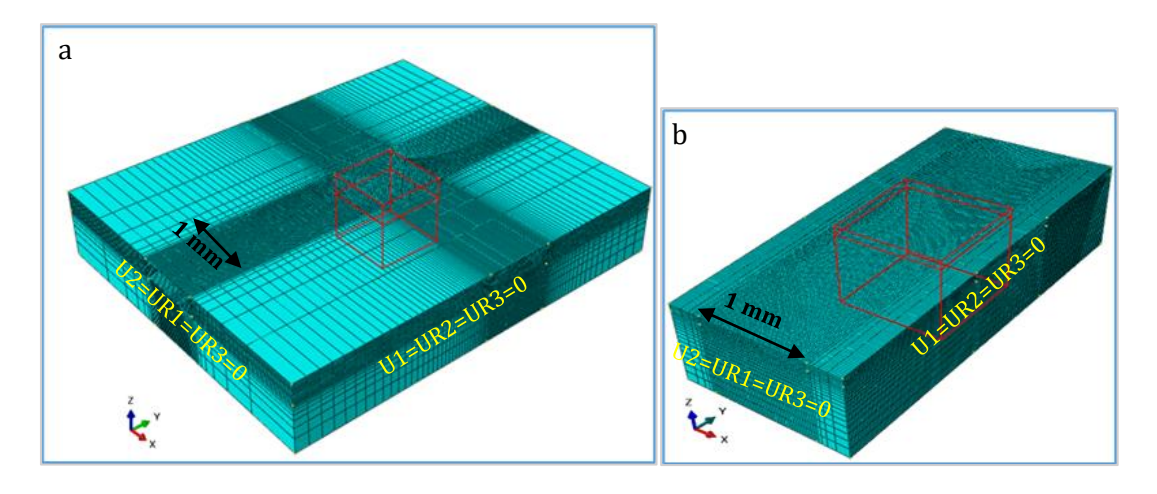


Figure 3.9: Work material meshing strategy for a) tool rolling and b) tool sliding FEM modelling approach

In a standard /Implicit analysis, the C3D8R element type with the Standard 3D stress element family was selected to study only the mechanical field output. The well-defined hexagonal shape of the element enables automated control and extraction of field output through Python coding in the Abaqus Python environment, utilizing its element ID. Additionally, an hourglass control property of the element is used to prevent non-physical deformation or distortion of the element. The mesh size of 0.20mm is used at the contact surface, and it increases to 0.120mm when it is far from the contact region, to reduce computation time, as shown in Figure 3.10.

The total number of fine elements generated for the whole geometry was 204,960. The surface number of the generated fine uniform mesh was 8540; among these surface elements, 3500 elements were used for an accurate simulation of one tool pass in Implicit finite element analysis.

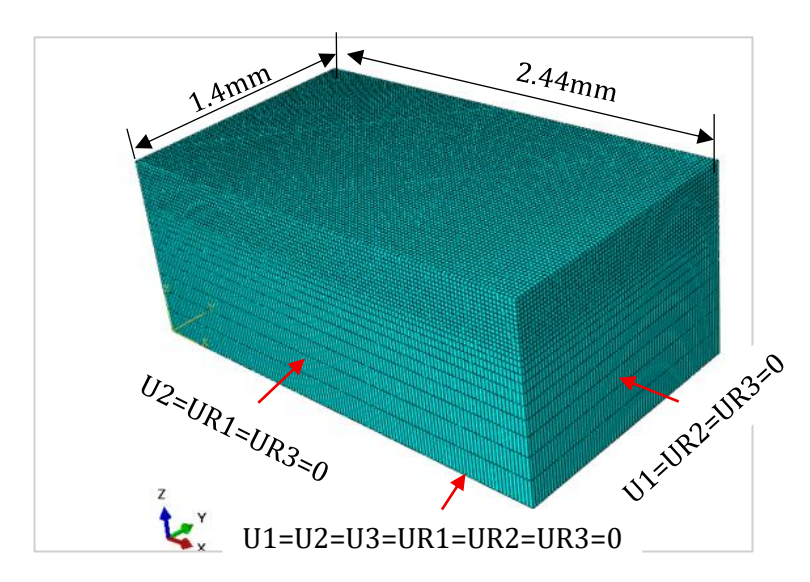


Figure 3.10 : Work material meshing strategy and boundary condition for the Implicit FEM modelling approaches.

3.4. Field output data extraction and analysis method

Field output data in finite element analysis are numerical simulation results distributed throughout the model for both explicit and implicit analysis. These are physical responses of the material or structure under ball burnishing loading conditions. In FEM modelling, the field output extraction is carried out at the Abaqus visualisation step on the Abaqus ODB file. After a successful and accurate data extraction, the numerical simulation result should be interpreted or analysed by plotting curves and bar charts to ensure model accuracy to support engineering decisions. These data analysis methods are primarily performed using Excel and MATLAB R2024b student version software.

In dynamic explicit analysis, thermo-mechanical simulation results, such as displacement, stress, strain, heat flux, temperature, and reaction force, could be extracted for analysis. However, in the Implicit analysis, only mechanical field output results, such as stress and strain components, are extracted for analysis. All field output data extraction used for this finite element method is categorised as a manual method or an automated method.

3.4.1. Manual field output data extraction method

Manual method FEM field output data extraction is a simple manual extraction method in which data is extracted directly on the visualisation module through the Abaqus graphical user interface (GUI) system from the ODB file. It is suitable for quick inspection and for some field applications where automation is not required. These extractions are carried out using the XY data field output and probe tool value found on the visualisation module queries tool for both nodal and elemental field outputs. Simple field outputs, such as deformation, reaction force, nodal temperature and nodal heat flux distribution, were extracted through this method.

3.4.2. Automated field output data extraction method

An automated data extraction method is the most effective technique for extracting field output, especially for complex and large finite element models. It uses the Abaqus application programming interface (API) [25] system. The interface enables the integration of a Python script, allowing it to run within the Abaqus Python environment (APE). The extracted data was saved as a CSV file for further analysis.

Writing a Python script is challenging and requires a detailed understanding of both the Computer-Aided Engineering (CAE) file and the output database (ODB) file. Python scripting can be developed using either coordinate points or element ID patterns. Scripting using the coordinate system works by calling four initial nodal x,y,z coordinate points to access a specific element. Currently, this method is efficient only for surfaces that undergo low-deforming processes, such as FEM modelling for turning processes. After numerous trials, this method proved ineffective for the ball burnishing process because the coordinate points before and after deformation are different. Also, the deformation behaviour is higher at the contact region and lower farther from it, and the mesh size for the element is not uniform throughout all the bodies.

Python scripting using the element ID pattern was highly efficient for extracting field output in the current finite element modelling of the ball burnishing process. In this case, first, it needs to study the element ID arrangement of the model and then develop a script based on the increment and decrement of the element IDs. Finally, it is necessary to connect those element IDs with the field output using a Python script to run on the Abaqus Python environment, a sample verified script to extract residual stress is presented in (Appendix D).

Chapter 4

Results and discussion

This chapter presents a comprehensive result and discussion of both dynamic explicit and Implicit finite element analysis. The results are interpreted based on both the physical phenomenon of the ball burnishing process and a numerical simulation approach on the effect of working conditions on mechanical and thermal responses. The results of the dynamic explicit numerical simulation are discussed to verify model accuracy and stability, as well as to study the thermo-mechanical response during toolwork material interaction. Additionally, a detailed discussion of the standard/implicit analysis results for equivalent plastic strain and residual stress distribution for multipass burnished work material is presented. Finally, the finite element residual stress distribution is validated through a comparison of experimental XRD residual stress measurements, and an optimal type of burnishing tool is proposed based on a computational performance study of the model. The numerical simulation results and discussion on the analysis of sliding and rolling actions are only presented at an applied load of 348 N.

4.1. Dynamic explicit FEM stability and accuracy

The dynamic finite element analysis (FEA) was performed to simulate the thermomechanical behaviour of the physical ball burnishing process for both tool rolling and sliding conditions. The accuracy and stability of the finite element model were investigated under dynamic loading conditions for a single tool pass at various applied burnishing forces, while maintaining a constant burnishing speed and a fine mesh.

The dynamic explicit approach was suitable for studying the effects of working conditions on the physical interaction between two components of the burnishing process over a short time period. It allows for the accurate capture of the thermal-mechanical response, including penetration depth (to verify a stable burnished zone), reaction forces, and nodal temperatures during the interaction. The burnishing force was applied in the–Z axis and the burnishing tool travels (burnishing direction) in +Y axis.

The evolution of stress and temperature distribution of the dynamic explicit analysis simulation result for the tool sliding and rolling conditions is presented in Figure 4.1 and Figure 4.2, respectively. The S'Mises stress distribution for two burnishing conditions illustrated that yielding and plastic deformation are successfully produced. The generated maximum temperature is approximately the same, with a slight increment in the sliding condition due to the dragging effect during the process.

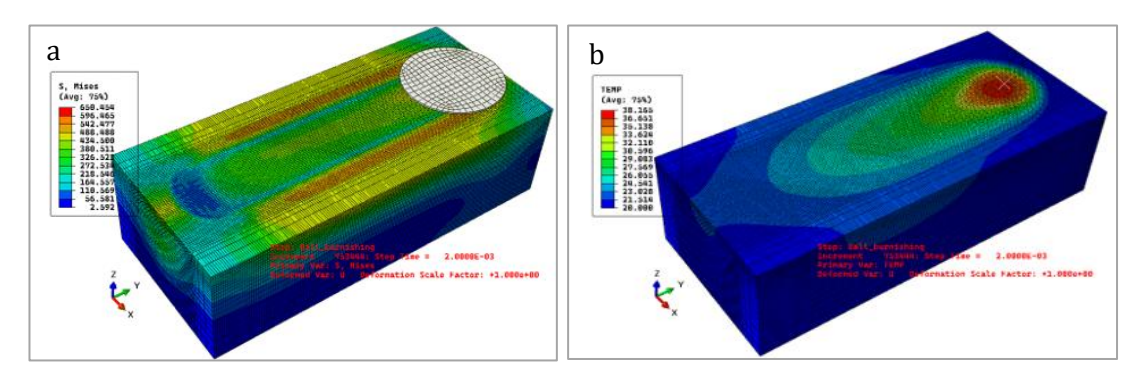


Figure 4.1 : Slide burnishing numerical simulation result at Fb 348 N, a) s' mises stress distribution, b) temperature distribution

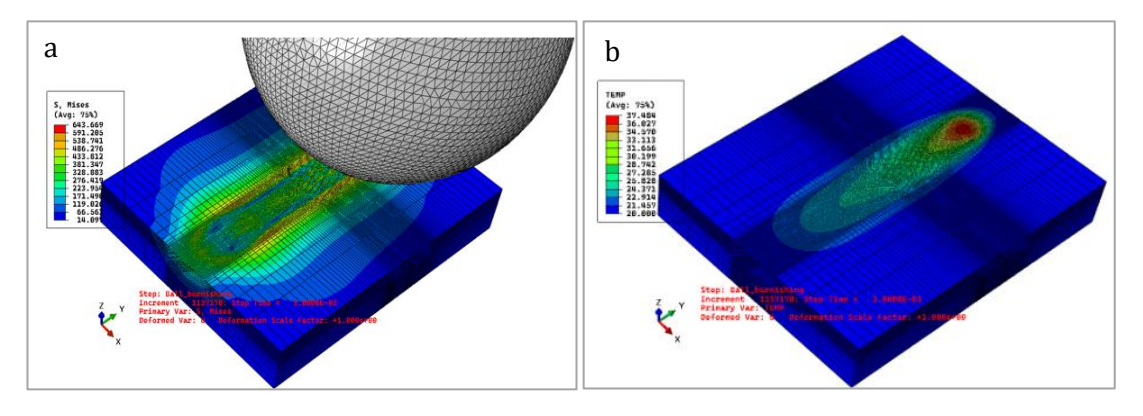


Figure 4.2: Roller burnishing numerical simulation result at Fb 348N, a) s' mises stress distribution, b) temperature distribution

4.1.1. Depth of penetration

In the FEM modelling of the burnishing process, studying penetration depth plays a crucial role in verifying the model stability and accuracy. Penetration (δ) is the maximum deformation produced parallel to the applied force direction during the burnishing process, resulting in changes in the shape of the surface of the Aluminium 2024-T5311 material. In numerical simulation. It is determined by analysing the displacement in the compressive Z direction (U3) extracted at the reference point of the burnishing tool, as shown in Figure 4.4a.

It is the sum of the temporary (elastic) and permanent (plastic) deformation, depending on the material response. But, in ball burnishing, the penetration depth is equivalent to permanent plastic deformation.

The evolution of penetration depth (mm) through time (ms) Figure 4.3 indicates that the higher and unstable condition occurs at the beginning of the burnishing process and stabilises after a short time increment. This illustrates a real burnishing process, which is always unstable during instantaneous contact between the ball and workpiece at the moving parts. This behaviour can be reduced by applying a small-time tabular amplitude, allowing the applied burnishing force to increase gradually only when the tool is in a sliding condition (TS). Due to instantaneous loading applied during the tool rolling condition, this approach creates very high penetration at the beginning of the process. It starts to stabilise after a short time, similar to a sliding condition. The fluctuation of the curve clearly demonstrates the rolling effect.

The tool rolling (TR) action induces plastic deformation, allowing the material to flow both in depth and in lateral directions. Continuous and uniform pressures or stresses applied perpendicular to the surface promote a deeper penetration depth. Whereas the tool sliding only promotes material to move sideways across the surface, resulting in less material penetration depth. A tool rolling condition can create up to 20% higher penetration depth at 348N burnishing force.

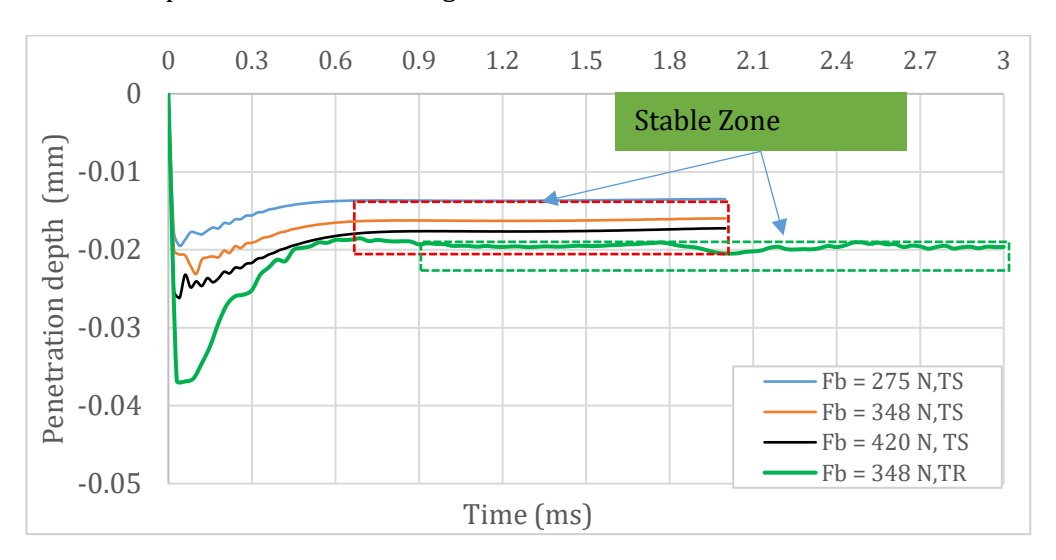


Figure 4.3: Evolution of penetration during the slide ball burnishing process

The comparison of the average penetration depth obtained at the stable zone FEM result Figure 4.4b and the Hertz elastic contact analysis is presented in Table 3.6 confirming an accurate load transfer from the burnishing tool to the workpiece with good consistency.

Additionally, increasing the applied burnishing force leads to an increase in penetration depth for both tool sliding and rolling conditions. presented on Figure 4.4b.

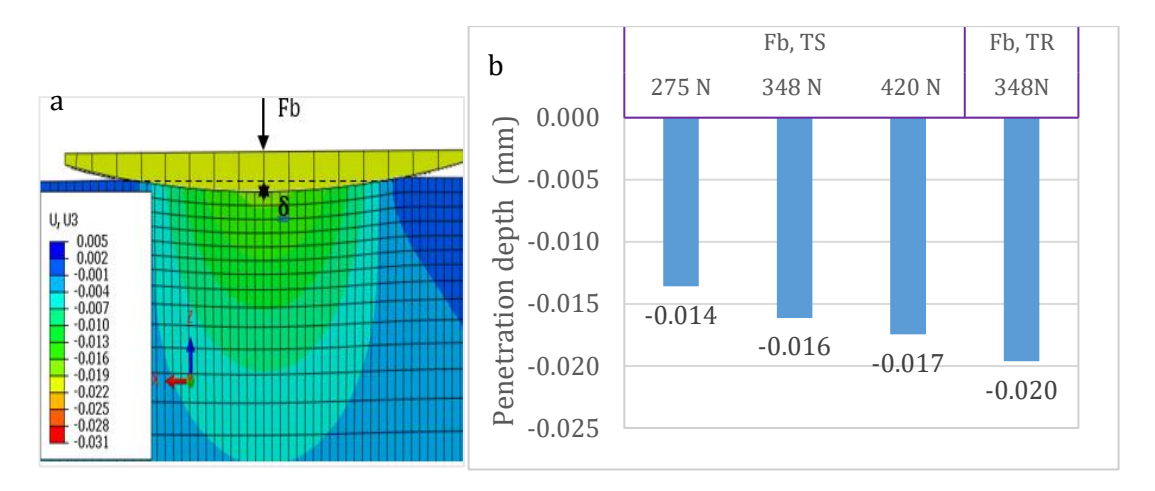


Figure 4.4 : FEM modelling, a) tool sliding displacement result at Fb 348N and b) average penetration at stable zone for different forces and types of tool motion.

4.1.2. Evolution of reaction force

Studying the evolution of the Reaction force is also an approach to checking model accuracy and reliability. In finite element modelling (FEM) of ball burnishing, there are normal reaction forces (Fn) and tangential reaction forces (Ft). The tangential reaction force is the force produced to resist the burnishing process in the Y direction. The result should be extracted at the tool reference point (RF2 value) in the direction of tool travel. Since the burnishing process was carried out without a friction coefficient, a small tangential reaction force is generated due to the ploughing effect of the burnishing tool during the process, as shown in Figure 4.5a. Normal reaction force is a force that resists the applied burnishing force, which is the total sum of nodal forces (RF3 value) produced at the bottom surface of the workpiece or in the opposite direction to the applied burnishing force. The evolution of the normal reaction force over time is presented as shown in Figure 4.5b.

The instantaneous applied burnishing force at the beginning of tool contact with the work material initially leads to an increase in the reaction force. Additionally, the tool rolling action clearly indicates that the reaction force is higher than that of sliding due to the rolling action plus the instantaneous load. In both tool sliding and rolling conditions, the reaction force stabilises after a short time increment.

The average reaction force at the stable region indicates an accurate load transfer during the burnishing process in the Figure 4.6. These kinds of reaction force distribution behaviours are consistent with investigations [43], [52].

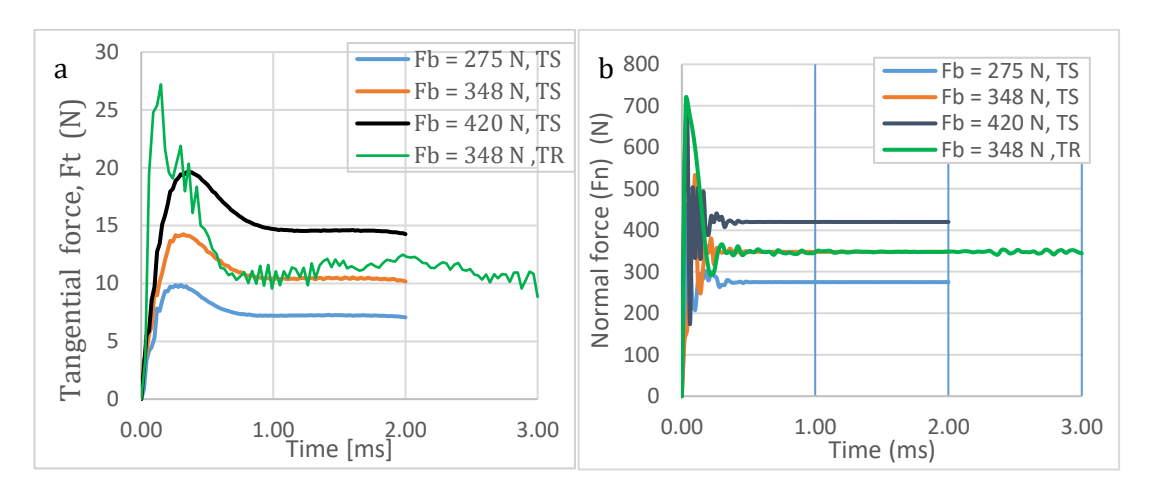


Figure 4.5: Evolution of reaction force a) tangential (Ft) and b) normal (Fn)

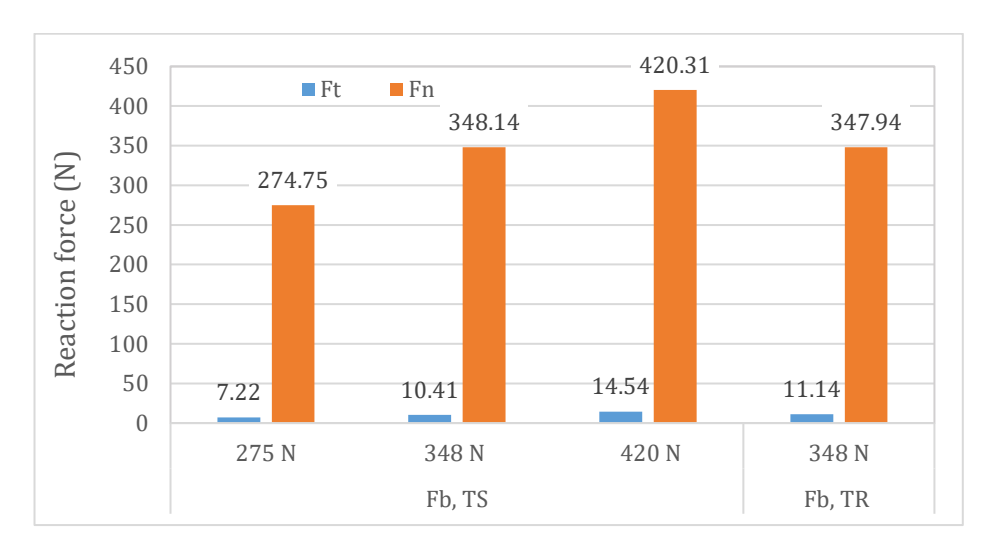


Figure 4.6: Average Tangential and normal reaction force at the stable region

4.1.3. Nodal temperature distribution

In finite element modelling of the ball burnishing process, the predefined temperature was set to room temperature (20 °C). The nodal temperature is the local temperature used to show the critical temperature at a small nodal point. The nodal temperature distribution for the current FEM modelling of frictionless burnishing is primarily due to the heat source generated by plastic work, as given by Eq.(3.4). This temperature generation, defined by analytical reasoning and corresponding to an 85% flow stress, was converted to work due to the use of a 0.85 Taylor-Quinney coefficient. The numerical simulation for nodal temperature distribution is indicated in Figure 4.7a.

The evolution of nodal temperature distribution through time is shown in Figure 4.7b was extracted at the surface contact nodal point, indicating that the temperature increases proportionally with the applied burnishing force. The nodal temperature can reach around 43°C at the 420N slide burnishing approach. Additionally, the tool rolling and sliding conditions of the burnishing process, which generate heat during the process, are insignificant. In general, the generated maximum temperature at the contact region under tool sliding and rolling conditions is very low, which implies that its effect on residual stress is negligible. These phenomena are expected in frictionless conditions.

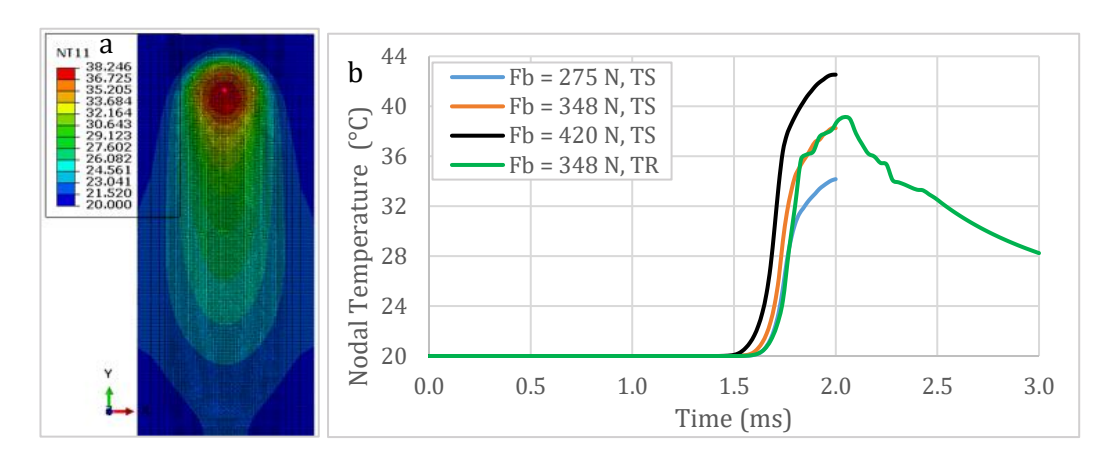


Figure 4.7: Nodal temperature distribution, a) tool sliding FEM result at Fb 348 N and b) comparison of TR and TS with different burnishing forces

4.2. Burnishing tool and work material interaction

Studying the contact mechanics of burnishing tools and workpieces plays a crucial role in estimating the interaction thermo-mechanical response during the burnishing process. The tool rolling and sliding effects on penetration depth, reaction force, and nodal temperature are approximately similar, as discussed in the Section 4.1. Therefore, only a tool sliding condition is considered in the current dynamic explicit FEM modelling of ball burnishing to study tool-workpiece contact mechanics. A spherical cap of a burnishing tool is pressed against the workpiece under a controlled normal burnishing force during slide burnishing. This action creates a localised contact region where the generated contact geometry and pressure depend on the applied load, ball diameter, and elastic-plastic properties of the material. Material surface property modification is due to permanent plastic deformation induced by localised normal stress.

The main criteria for selecting surface contact area are due to the phenomenon of field output distribution produced during the process. For the current study, a small cube section from the full work material geometry with 1 mm length for each face at the stable zone of a dynamic explicit FEM model. And the slide burnishing tool was paused at simulation Frame 61 (step time: 1.22ms) precisely at the middle of the cube XY plane surface Figure 4.8a. By considering the surrounding approximately zero field output, the rectangular surface area (1×0.62) mm2 considered for detail analysis. Based on this surface dimension, there are 50 elements in the X direction and 31 elements in the Y direction at a mesh size of 0.02 mm. The line in the figure in the X direction represents the element set, which has a 50-element list, and a total of 31 lines in the Y direction are represented for detailed study as indicated in Figure 4.8b.

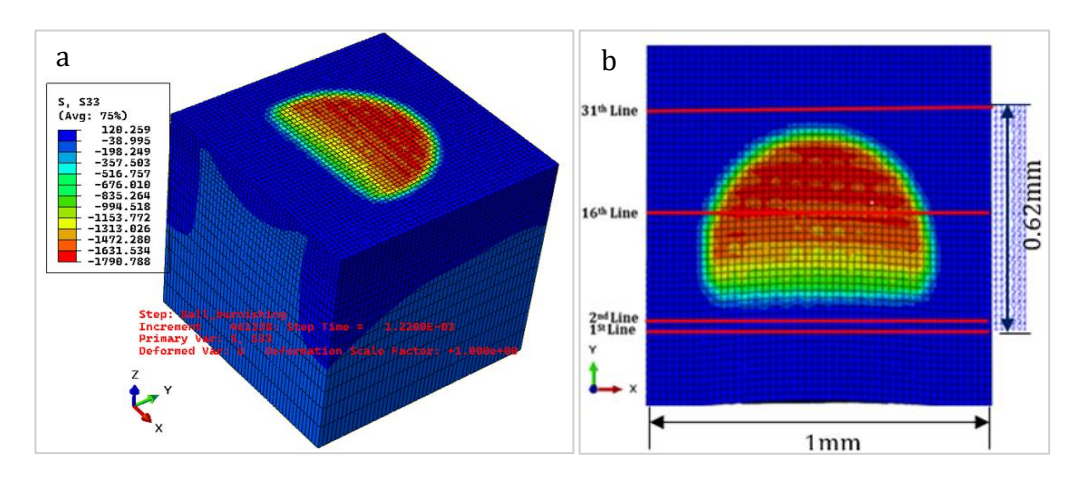


Figure 4.8 : A stable region cube section FEM result at Fb 348N a) 3D s33 (normal stress) distribution and b) 2D surface contact region

The surface dimensions and pressure distribution of the tool-workpiece contact region are compared across all burnishing forces. The thermo-mechanical response, including normal stresses (s33), shear stress (s23), temperature (TEMP), and heat flux (HFL) distribution, which is extracted at the C3D8RT elemental integration point, are examined only at Fb 348N and the tool sliding condition. Depending on the mesh size and the generated element on the selected section, a total of 50×31 matrix data is always extracted for all output fields, and the results are interpreted using different plots. The U1 and U2 represent the displacement values for perpendicular to the burnishing direction (X axis) and the burnishing direction (Y axis) shown in Figure 4.8b, respectively, which are used to plot all field output simulation results.

4.2.1. Contact length and pressure

Before proceeding to the detailed analysis, it is necessary to observe the surface contact length (a) and maximum pressure (Po) produced at the contact surface zone. The shape of the contact zone is not exactly a half-circle, but it approximates to a circular segment in which one-quarter of the part is in appear, because the burnishing process was paused at a stable region randomly. All phenomena of slide burnishing at three applied forces are studied in the rectangular sectional area of the surface XY plane for U1 and U2 displacement values, and the double arrow inside the figure indicates the maximum contact length (a) produced in Figure 4.9.

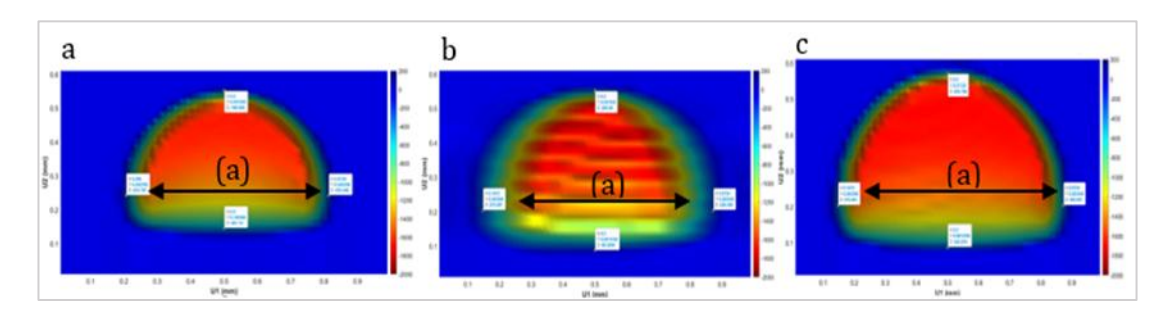


Figure 4.9: Surface contact length for different burnishing forces, a) at 275N, b) at 348N and c) at 420N.

According to Table 4.1, higher applied burnishing force creates a higher contact length (a), like penetration depth. This situation arises from the application of a burnishing force to a hard, non-deformable ball or a fixed burnishing tool, considering modelling considerations. This approach is also crucial for verifying the accuracy and reliability of FEM modelling results by comparing them with the analytical estimations based on Hertz elastic contact theory. The contact length estimation from FEM modelling and HCT analysis Table 3.6 has a good agreement. Also, the maximum pressure generated on the contact zone under FEM is significantly higher than the yield stress of the Al 2024 alloy material property. This implies that the pressures generated at the contact zone under the applied burnishing force are sufficient to induce plastic deformation.

| Burnishing force (N) | Contact length, a (mm) | Maximum pressure, Po (MPa) |
|----------------------|------------------------|----------------------------|
| 275 | 0.418 | 3200 |
| 348 | 0.434 | 3314 |
| 420 | 0.462 | 3500 |

Table 4.1: Contact length and maximum pressure at different burnishing force

4.2.2. Normal stress distribution

The distribution of normal stress (S33) extracted values for each element at the contact region, which is produced by the applied burnishing force per surface area. The direct normal stress has a direct relation to the applied force and is inversely proportional to the contact area. A 3D plot Figure 4.10a indicates the phenomenon of normal stress distribution in the Z-axis and the displacement values of U1 and U2 at the contact zone. The surface contact region on the plane defined by U1 and U2 illustrates the normal stress phenomena on the surface, where the red colour in the region indicates the place where higher compressive stress is produced in Figure 4.10b.

A filtered normal stress distribution was also characterised line by line for 31 individual 2D plots to show its behaviour for each 50 elements along each line. This approach provides a detailed representation of fine mesh local stress. A maximum normal stress can reach up to -1800 MPa at a burnishing force of 348N, exactly at the middle of the U1 direction Figure 4.10c. Whereas the maximum normal stress is more shifted to the end of the U2 direction or the leading position. Due to the combined effect of loading and the simultaneous movement of the burnishing tool over a short period of time, the non-linear peaks and valleys suggest complex interactions Figure 4.10d.

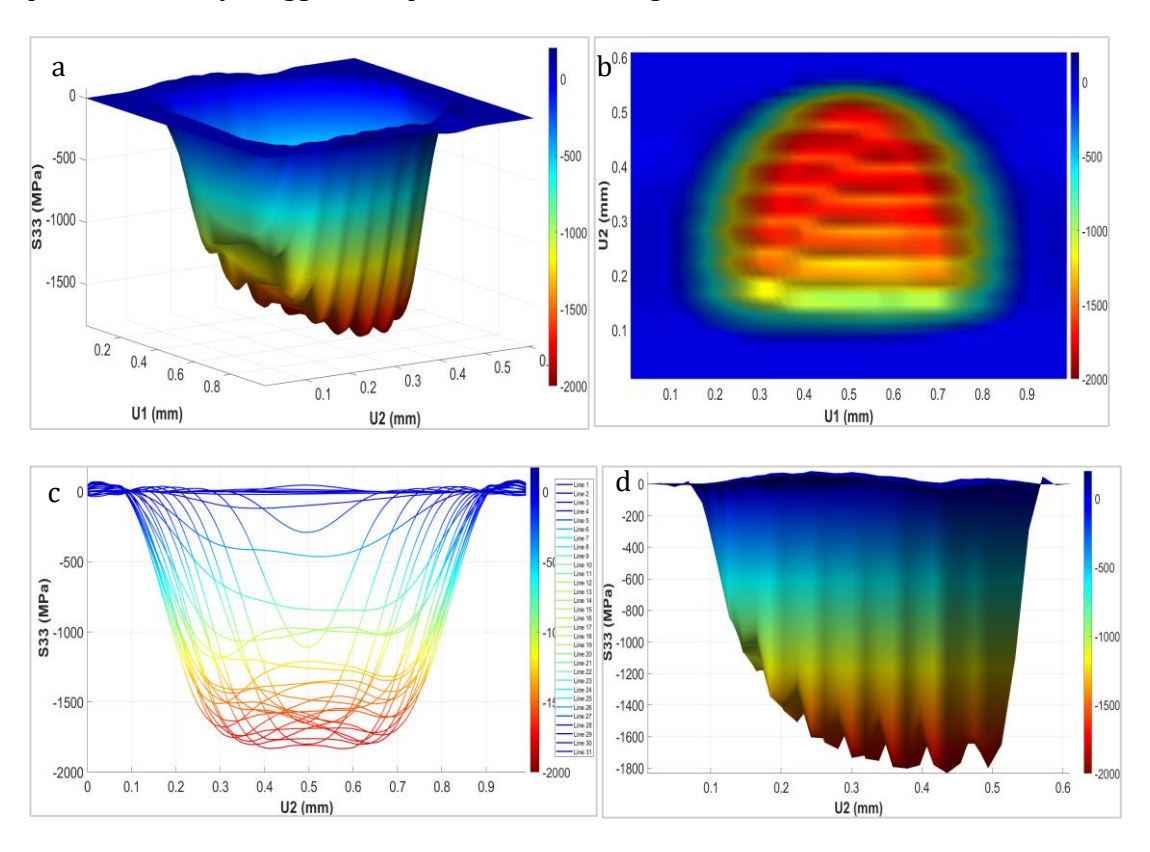


Figure 4.10: Normal stress distribution a) 3D plot, b) 2D contact surface, c) 2D plot normal stress for 31-line and d) 2D plot in burnishing direction.

4.2.3. Shear stress distribution

For a frictionless burnishing process, a small tangential reaction force was produced due to the burnishing ploughing effect of the burnishing tool, as discussed in the section 4.1.2. These tangential forces are responsible for creating shear stress between the burnishing direction and the tool movement direction, as represented by s23 stress in the Abaqus stress field output. The 3D shear stress plot, shown in Figure 4.11a highlights a symmetric distribution of shear stress for the leading edge and trailing edge caused by the applied burnishing force and unidirectional motion of the burnishing tool. The maximum compressive shear stress was experienced at the position of the Leading edge; in contrast, a maximum tensile shear stress is produced on the trailing edge.

The peaks and valleys of shear stress behaviour during the burnishing process are due to non-uniform local contact between two components and elastic-plastic material properties. The peak corresponds to an elastic rebound, leading to a tensile stress concentration, and the valleys illustrate compressive stress when a hard ball presses against workpieces. This is because the material flow is easy to flow outward (tensile) instead of inward (compressive), as shown in Figure 4.11a, Figure 4.11b and Figure 4.11d. The maximum compressive shear stress and maximum tensile shear stress are found to be -180MPa and 180MPa, respectively, in Figure 4.11c. These stress amounts are less due to low tangential load and are not enough to create a full plastic deformation in shear direction.

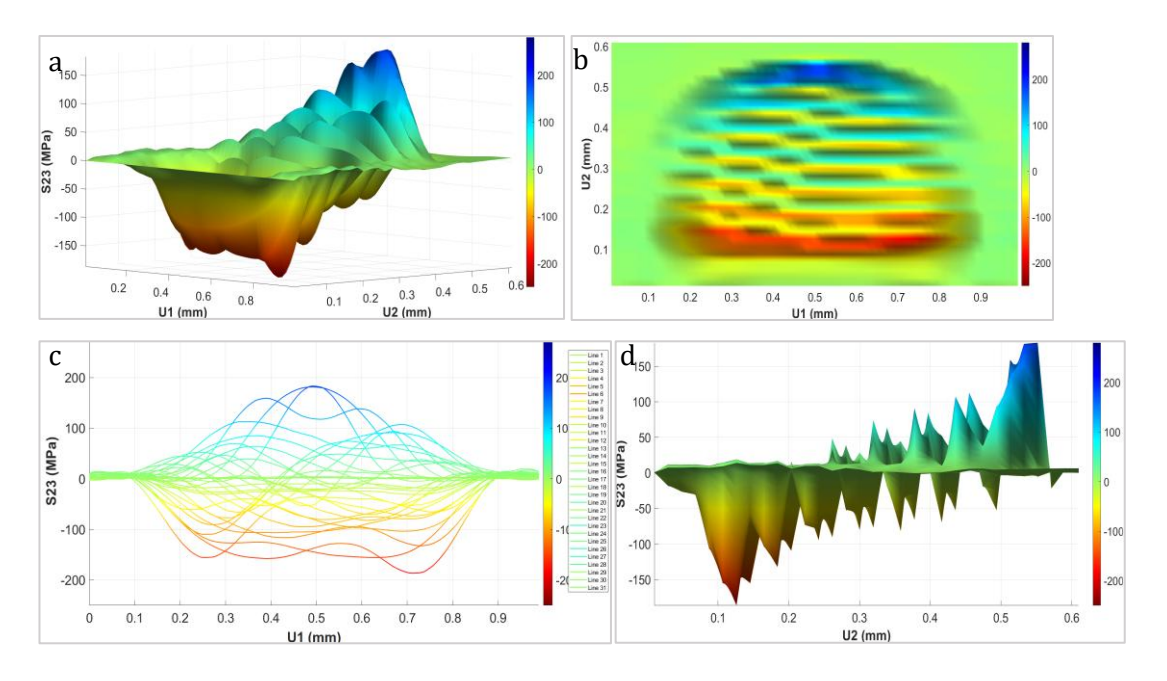


Figure 4.11: Shaer stress distribution, a) 3D plot, b) 2D contact surface, c) 2D plot shear stress for 31-line and d) 2D plot in burnishing direction

4.2.4. Temperature distribution

In FEM modelling of the burnishing process, a localised heat is generated at the contact zone due to a coupled temperature–displacement model representation. To study the evolution of temperature in the contact region, an elemental temperature was extracted from the integration of a point. In a frictionless condition, the conversion of inelastic work into heat are the only source of temperature during plastic deformation discussed in the section 4.1.3. The temperature-dependent material properties in the numerical simulation, such as thermal conductivity, specific heat, and other mechanical properties, were essential for capturing thermal responses in the model. Although burnishing processes were carried out at low speed, a high contact pressure and repetitive toolworkpiece interaction can induce measurable temperatures.

A 3D plot in Figure 4.12a illustrates the temperature distribution under three axes of the plane, where the temperature distribution is symmetric in the U1 direction and asymmetric in the U2 direction. And the distribution of temperatures is reduced when the surface is far away from the centre of contact in Figure 4.12b. A 2D plot representation indicates the temperature distribution, precisely at the midpoint of U1, where the maximum 38°C is produced, as shown in Figure 4.12c. However, this maximum temperature is not precisely at the mid-point in the U2 direction because the leading edge of the burnished surface gets more heat before the trailing edge, as shown in Figure 4.12d.

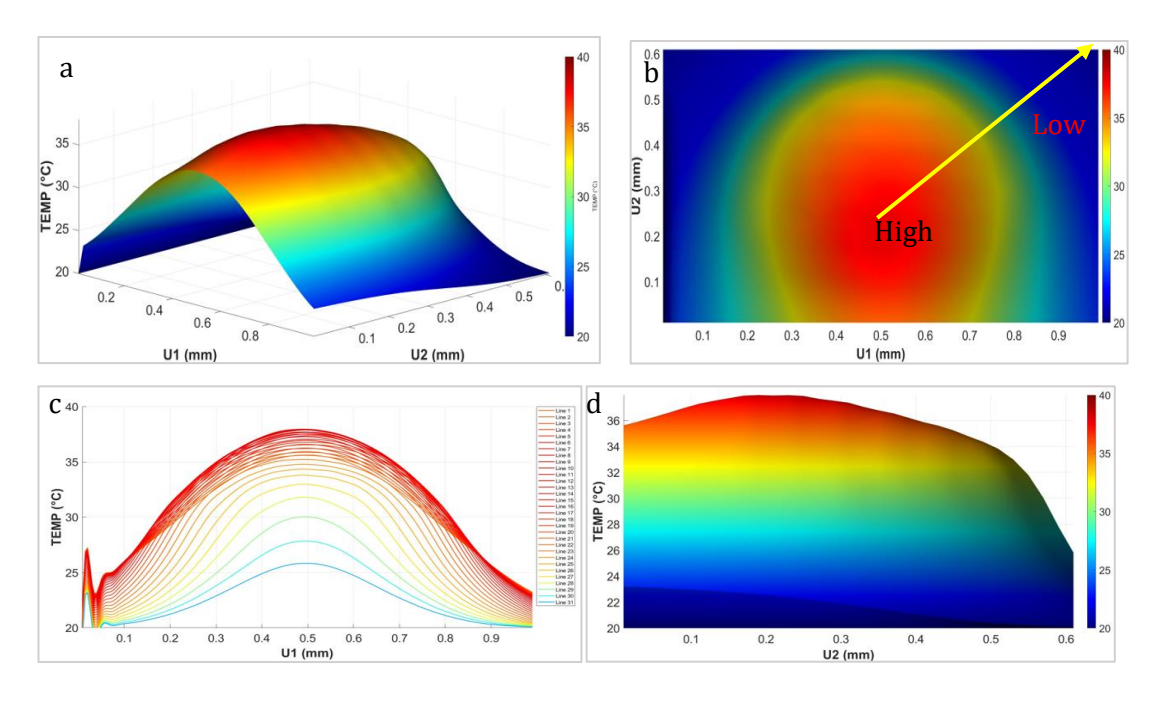


Figure 4.12 : Temperature distribution a) 3D plot, b) 2D contact surface, c) 2D plot temperature for 31-line and d) 2D plot in burnishing direction

4.2.5. Heat flux distribution

Heat flux is the rate of heat transfer per unit surface area expressed in (kW/m²). The analysis of the solver used to estimate heat flux by multiplying the heat source comes from the plastic work Eq.(3.3) and element thickness (in this case mesh size). In the ball burnishing process, studying the heat flux distribution at the contact interface provides crucial insight into the localised thermal loads generated during the process. This is essential for evaluating material behaviour and its functional performance. In the current numerical simulation, a proper boundary condition with a coupled temperature was considered and studied within a specified rectangular section of the contact region. A 3D plot in Figure 4.13a presents a three-axis heat flux distribution. The heat transfer in the leading edge is towards the material depth, and the highest heat per surface area is accumulated or transferred to the trailing edge. Figure 4.13b indicates the distribution of heat flux on the 2D surface of the contact region for U1 and U2 displacement.

A combined filtered 2D plot Figure 4.13c. illustrates the detailed distribution of heat flux line by line when the burnishing tool moves from the leading to the trailing edge. The maximum and minimum heat fluxes are produced exactly at the midpoint in U1 and are reduced symmetrically on both sides. But the maximum heat is generated at the end of the trailing edge, and the minimum heat flux is found at the leading edge, shown in Figure 4.13d and it can reach to $14,000 \text{ kW/m}^2$.

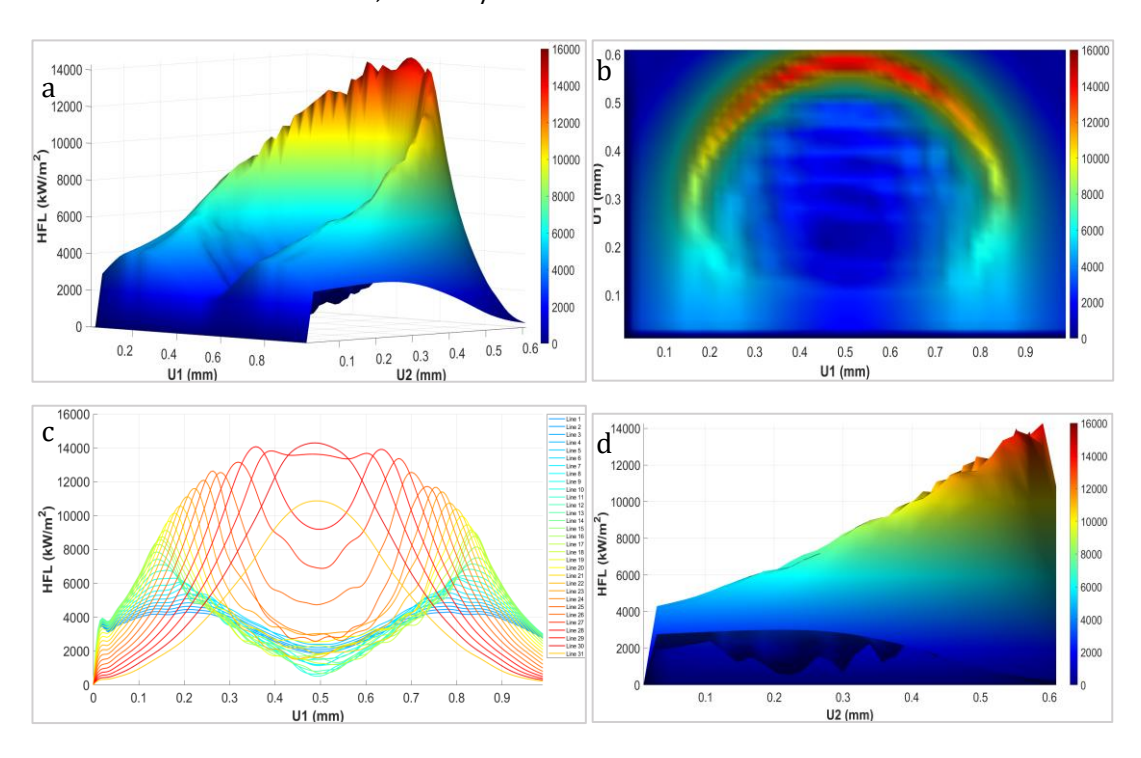


Figure 4.13 : Heat flux distribution a) 3D plot, b) 2D contact surface, c) 2D plot for heat flux for 31-line and d) 2D plot in burnishing direction.

4.3. FEM results of plastic strain and residual stress

The current study focuses on 3D FEM modelling of the burnishing process to predict the residual stress distribution on Aluminium 2024 alloy material. Residual stress in an engineering component has significant benefits and is a primary factor in improving functional performance. The temperature and heat flux distribution produced under the dynamic explicit model was low, so its effect on residual stress and plastic strain is almost negligible, as discussed in the above section. 4.2.4 and 4.2.5. To replicate a physical ball burnishing process on cylindrical workpieces, a small rectangular cut section was used for FEM analysis as discussed. 3.3.2. Since the full revolution simulation is not performed, each burnishing operation is referred to as a tool pass for the purposes of discussion.

A total of 11 steps were dedicated to 10 tool passes and 1 for the unloading step for model stabilisation and force removal on the numerical simulation. Those multiple passes enhance the FEM model uniformity and stability of residual stress and plastic strain distribution. The surface texture for both tool sliding and tool rolling is almost similar. But the discussion only presents the tool sliding numerical simulation for different fields' outputs. The Figure 4.14 illustrates S, Mises stress distribution in which the tool travels in the Y axis, called the burnishing direction, and feed was applied in the X axis, called the feed direction. A cut section from A to B along the centre line is dedicated to extracting residual stress and equivalent plastic strain through the surface and the depth.

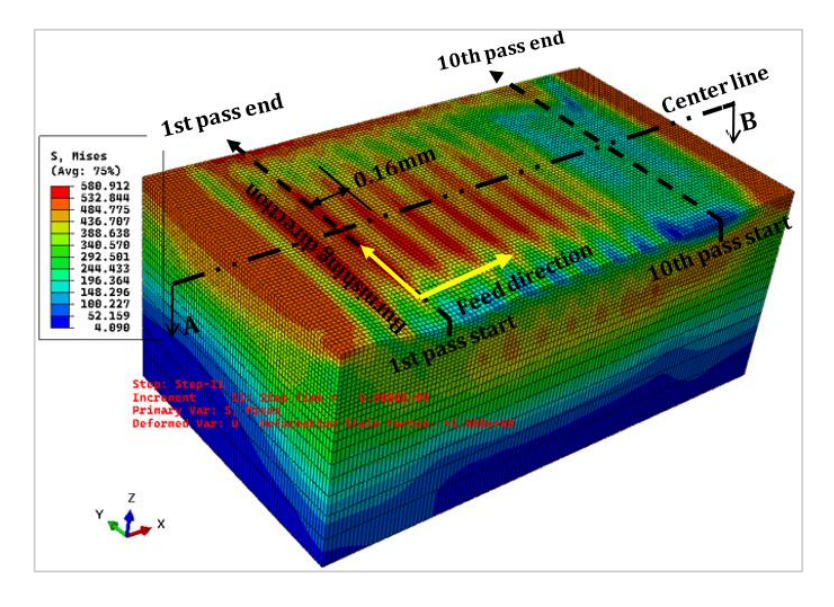


Figure 4.14: S, Mises distribution at tool sliding condition and 348N burnishing force.

4.3.1. Equivalent plastic strain

When the contact pressure exerted by the ball exceeds the yield strength of Aluminium 2024, permanent deformation is generated on the surface and subsurface layers. In numerical simulation, this dimensionless permanent plastic deformation is quantified through the accumulation of scalar measurements of plastic strain, known as equivalent plastic strain, represented by PEEQ [53] in Abaqus. Studying the PEEQ field output is a valuable tool for examining deformation behaviour and observing improvements in surface integrity properties.

A numerical simulation result plot indicated in Figure 4.16a a illustrates the equivalent plastic strain distributed for both sliding and rolling conditions on the surface of the burnished workpiece through the feed direction extracted from point A to B in Figure 4.15. At the beginning of the first tool pass, the equivalent plastic strain is higher because the material is free from stress concentrations. After the initial peak, the strain is reduced slightly and stabilises because the material begins to harden due to the previously generated tool pass permanent deformation. A sinusoidal type of curve is generated, and the peak equivalent plastic strain is produced exactly at the tool pass centre of contact, and the valley is at the centre of overlap. The tool's sliding and rolling conditions have no variation for equivalent plastic strain. The higher burnishing force leads to an increase in the equivalent plastic strain, as shown in Figure 4.16b.

The equivalent plastic strain distribution shown in Figure 4.17 indicates the distribution of equivalent plastic strain (PEEQ) through the depth at the stable region extracted from point C to point D in Figure 4.15 exactly at the centre of contact, the 4^{th} tool pass of the burnished workpiece. The highest equivalent plastic strain is found beneath the surface, located $20\mu m$ below the surface. Because material has freedom to flow at the surface, whereas beneath the surface, it gets more constrained, resulting predominantly in plastic flow. The distribution of equivalent plastic strain across the surface and depth has a direct relation with the burnishing force. The maximum equivalent plastic strain beneath the surface can reach 0.14, 0.17, and 0.21 for burnishing forces of 275N, 348N, and 420N, respectively, as shown in Figure 4.17a. This behaviour was also observed in the study of [28].

In addition, the contribution of sliding and rolling for plastic strain through the depth is almost negligible, as illustrated Figure 4.17b.

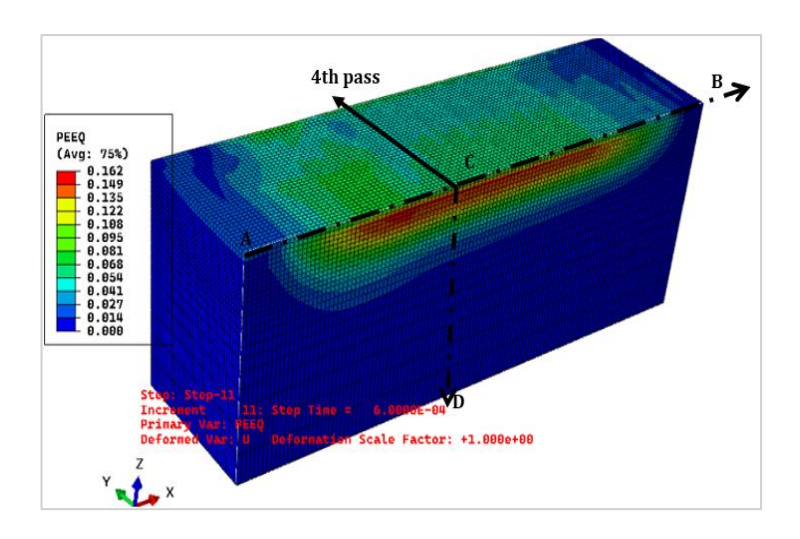


Figure 4.15: PEEQ distribution at tool sliding and 348 N burnishing force

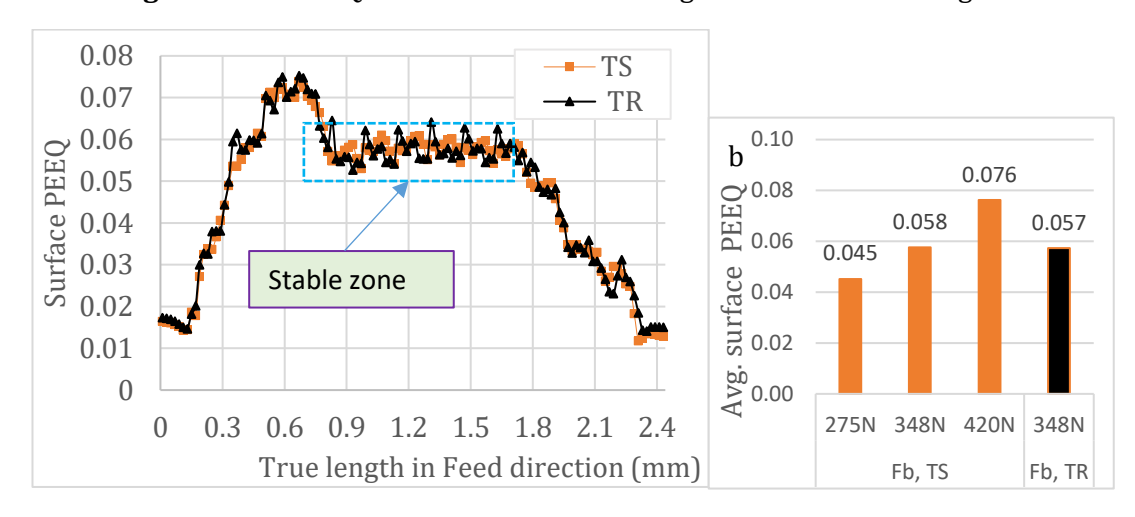


Figure 4.16: PEEQ distribution through the surface, a) for tool sliding and rolling at Fb 348 N and b) average surface PEEQ at the stable zone.

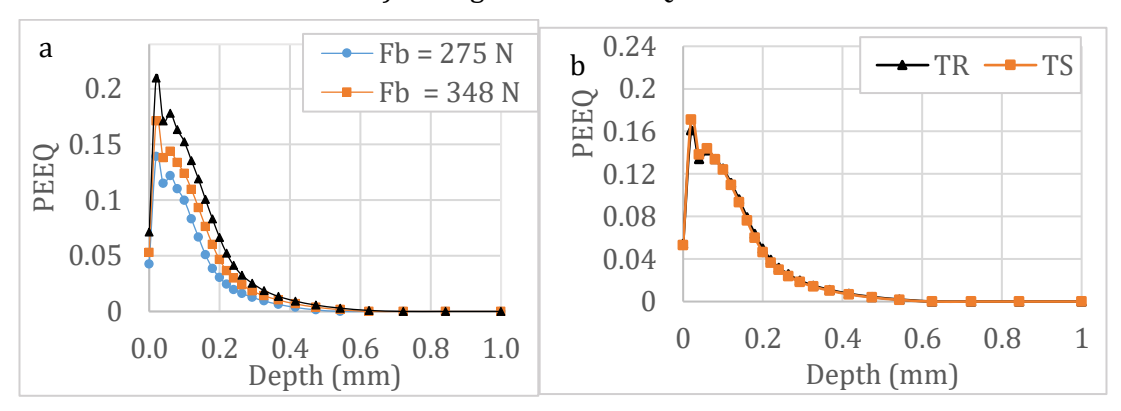


Figure 4.17 : PEEQ distribution through the depth, a) for the tool sliding condition and b) for the sliding and rolling condition at Fb 348 N.

4.3.2. Residual stress

The primary objective of this study is to estimate residual stress during the ball burnishing process using the finite element method. A two-step numerical modelling approach was implemented to capture a compressive residual stress. The primary consideration before extracting residual stress is unloading the burnishing load and temperature. For a small cut section of a rectangular plate workpiece, a burnishing force was applied along the z-axis (normal to the plate surface). The burnishing tool moved along the y-axis (burnishing direction) and multiple tool passes were made using feed along the x-axis (feed direction). The residual stress distribution is evaluated along the surface and depth of the workpiece.

The distribution of residual stresses comprises three main stress components, each assigned according to the stress tensor, for each element. A normal residual stress (σ_{zz}) is a stress distribution through the radial direction or parallel to the direction of force. This value is very high during the interaction between the burnishing tool and the workpiece, but it is eliminated after unloading. Then it is not essential for the analysis. Based on the investigation [51] the two principal residual stress distributions on a rectangular burnished work material are assigned as lateral and axial residual stress. A transverse (lateral) residual stress (σ_{xx}) is a distribution of stress in the direction parallel to the feed direction and perpendicular to the ball burnishing direction or axial direction. The stress distribution is referred to as longitudinal (axial) residual stress (σ_{yy}), which is a distribution in the direction parallel to the burnishing direction.

A. Surface Residual Stress Distribution

The residual stress distribution result was extracted at the centre of the burnished workpiece in the feed direction from point A to B in Figure 4.18. The lateral and axial surface residual stress (RS) at a burnishing force of 348N in Figure 4.19 illustrates that the highest compressive stress is accumulated near the boundary condition. The symmetric type of boundary condition constrains material flow for both feed and burnishing direction, and it facilitates compressive stress instead of tensile stress. Between the 1st and 8th tool passes, the curve shows a stable and sinusoidal curve that fluctuates between -100 to -200 MPa and -400 to -500 MPa for axial and lateral residual stress, respectively. The peak compressive stress for lateral residual stress is produced exactly at the centre of contact (Cc) of each tool pass. This behaviour is similar to equivalent plastic strain. In contrast, the peak compressive stress for axial residual stress is generated exactly at the centre of overlap (Co).

The last 9th and 10th tool passes, which are found to be 1.78 mm and 1.94 mm from the initial point, respectively, have produced a clear tensile stress, indicating that more than two tool passes are required to create compressive residual stress. The tool rolling condition creates a higher compressive axial stress and smooth lateral stress when compared with the tool sliding condition.

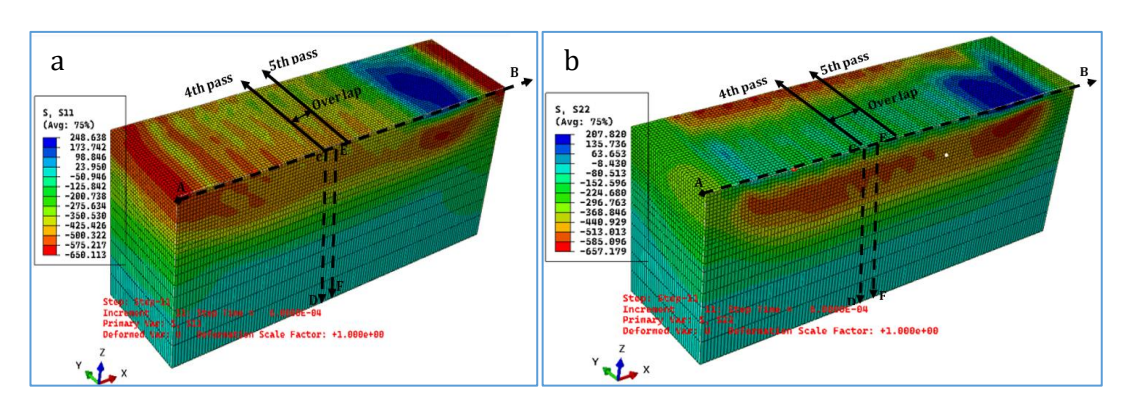


Figure 4.18: Stress field output distribution for 10 tool passes, a) s11 and b) S22

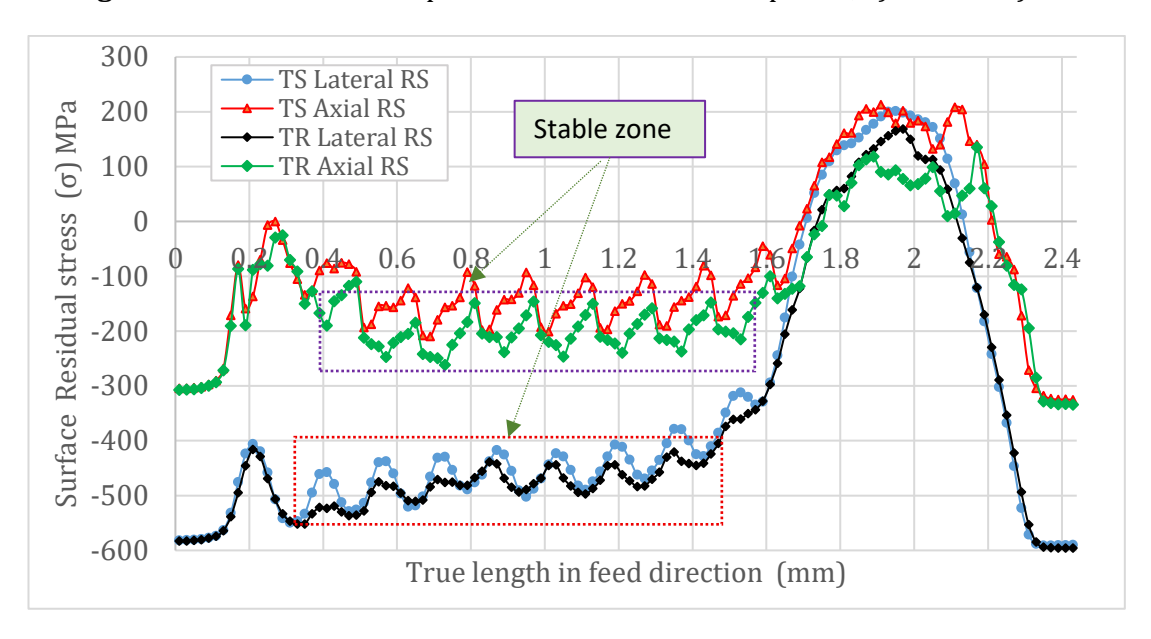


Figure 4.19: Surface lateral and axial residual stress (RS) distribution for tool sliding and rolling conditions at Fb 348N.

The column chart in Figure 4.20 demonstrates the average lateral and axial surface residual stress produced at different burnishing forces for the stable region shown Figure 4.20. Higher compressive stress is produced at higher burnishing force for the sliding condition. At the 348 N burnishing force, a tool rolling condition creates higher axial compressive stress. The tool rolling condition creates 30.2% higher axial residual stress than the tool sliding condition. In contrast, the lateral residual stress is almost similar for the two tool movement conditions.

An experimental investigation of the ball burnishing process through XRD measurement is under investigation [38] shows a good surface residual stress agreement with the current study.

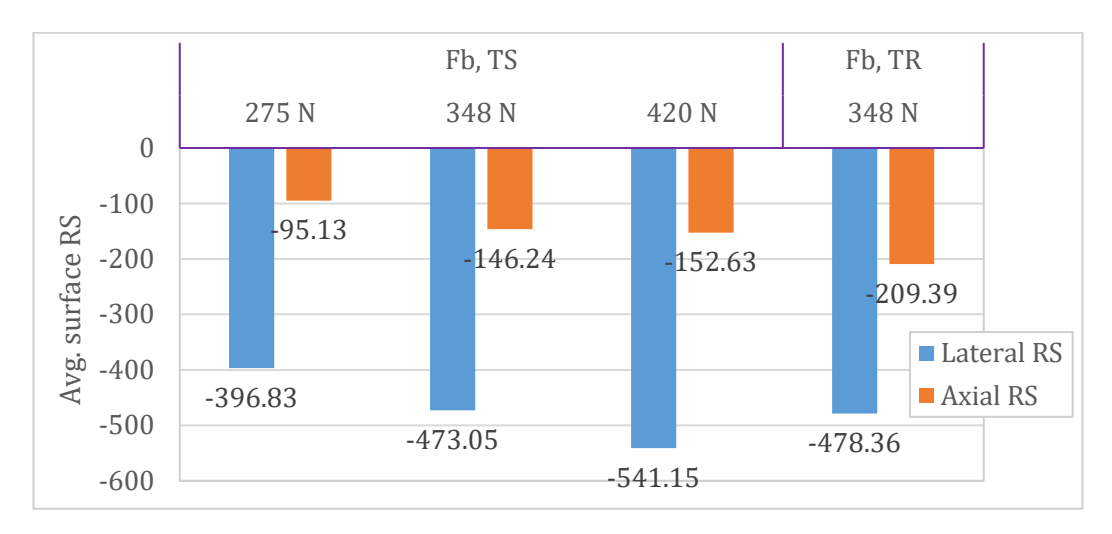


Figure 4.20: Average axial and lateral surface residual stress for tool rolling and sliding conditions and burnishing forces.

B. Residual stress distribution through the depth

The most interesting residual stress is the stress distribution along the depth of the workpiece, which helps estimate the service life of the component. Since the distribution of residual stress is not uniform throughout the surface discussed in Section A above, the first eight tool passes were stable. Then, the residual stress distribution was extracted from the centre of the 4th tool pass, exactly at the centre of contact (Cc) from point C to point D, and the centre of overlap between 4th and 5th tool passes, point E to F, shown in Figure 4.18. Both lateral and axial residual stress results have a comparative residual stress result obtained by experimental and FEM modelling study of the ball burnishing process on related Aluminium 2024 alloy material, investigated by different studies such as [9], [28], [38], [40], [43].

Under a sliding FEM approach, the lateral residual stress distribution produced at the centre of contact is higher at the surface for a burnishing force of 348N and 420N, but for a burnishing force of 275N, is produced below the surface in Figure 4.21a. Whereas the higher residual stress for the data extracted from the midpoint of the overlap is below the surface for burnishing forces of 275N and 348N, presented in Figure 4.21b. This is due to the amount of burnishing force was enough to create higher permanent deformation at the surface.

In general, a surface residual stress produced at the centre of contact creates higher compressive stress compared to stress at the centre of overlap, as discussed in the above section A. And a higher burnishing force can create a more compressive stress-affected zone.

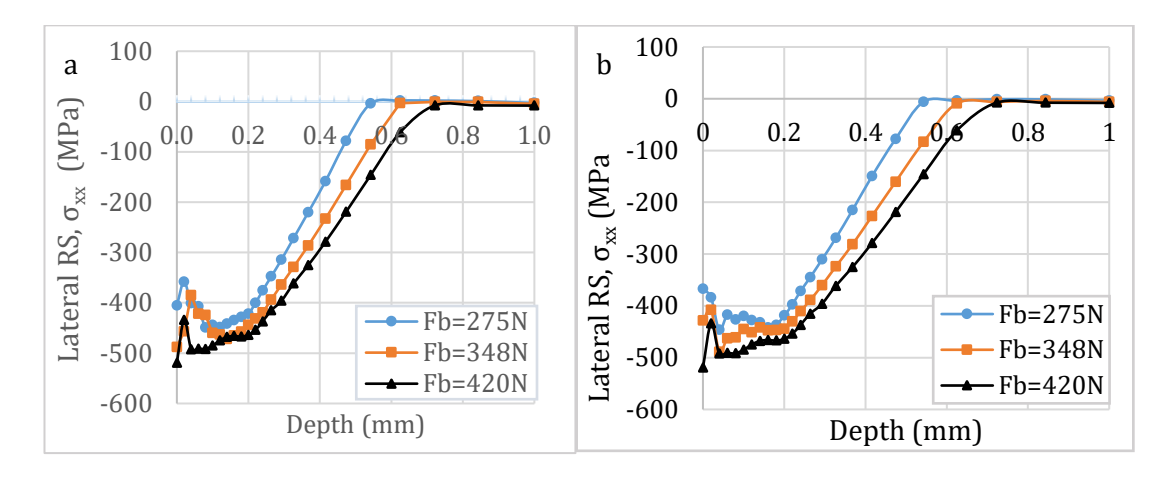


Figure 4.21: Lateral residual stress distribution under tool sliding through the depth extracted at, a) at the centre of contact and b) at the centre of overlap.

The behaviour of lateral residual stress extracted at the centre of contact, both tool sliding and rolling conditions, is almost similar to that shown in Figure 4.22a. But the tool rolling condition produces slightly higher compressive stress compared with the tool sliding, only at the surface, while through the depth are exactly similar in Figure 4.22b. In general, the tool sliding and tool rolling condition has no significant effect on producing compressive lateral residual stress.

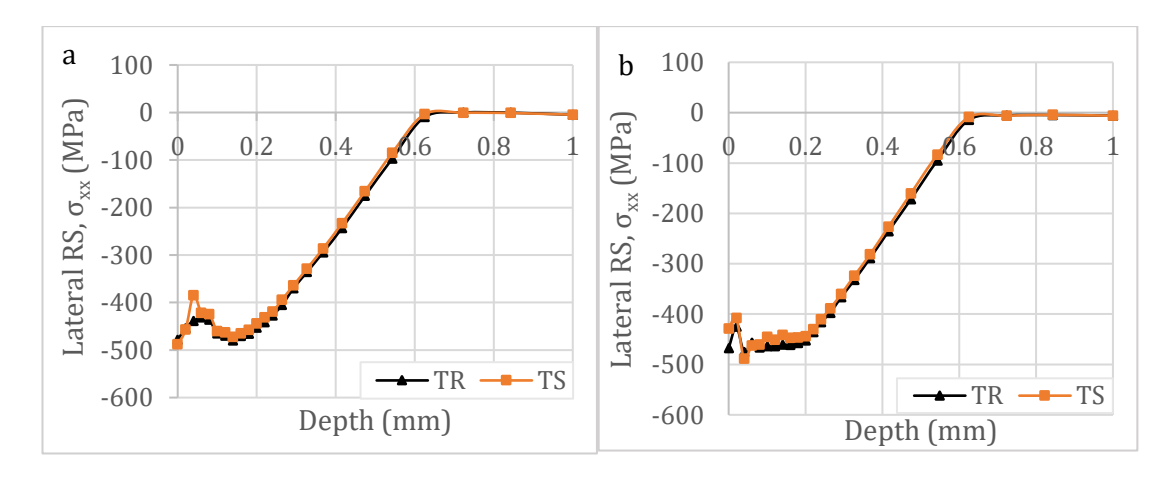


Figure 4.22: Lateral residual stress for tool rolling and sliding condition at Fb 348 N extracted at, a) at the centre of contact and b) at the centre of overlap.

A higher axial residual stress distribution along the depth of the workpiece is produced below the surface, around 0.2mm in Figure 4.23. The lowest surface residual stress is produced at the exact centre of contact (Cc), Figure 4.23a, whereas the higher surface axial residual stress is generated exactly at the centre of the overlap (Co) in Figure 4.23b. A reverse behaviour is experienced when it is compared with a lateral residual stress. The compressive axial residual stress can affect a workpiece up to 1mm in depth of work material, and higher burnishing forces create a wide stress-affected zone.

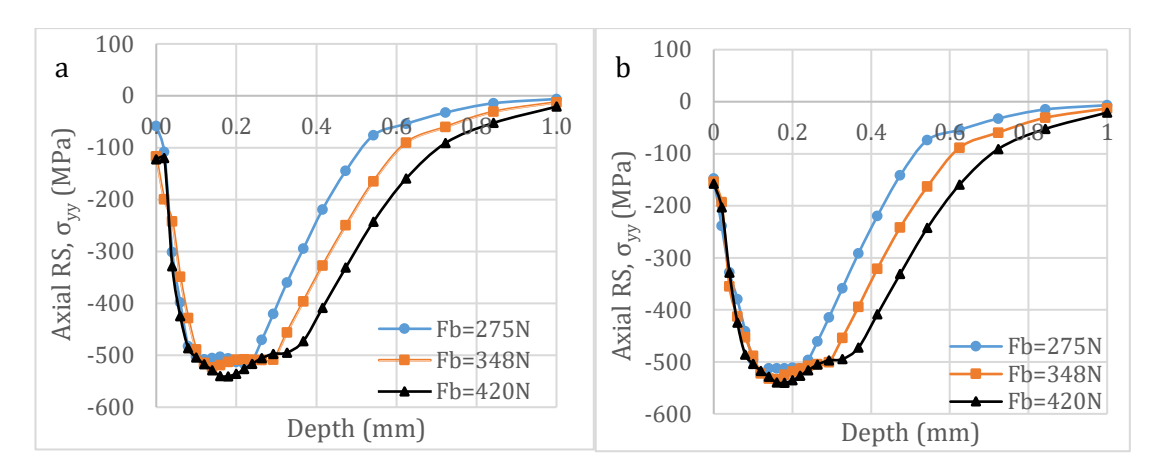


Figure 4.23: Tool sliding condition axial residual stress through the depth, a) at the centre of contact and b) at the centre of overlap.

A higher surface axial compressive stress is produced by the tool rolling condition when it compared with slide burnishing, as shown in Figure 4.24a. Especially, axial residual stress extracted at the centre of overlap, a tool rolling condition can produce up to 43.2% higher surface compressive stress than the tool sliding condition as shown in Figure 4.24b. But both tool movement conditions have the same residual distribution behaviour through the depth.

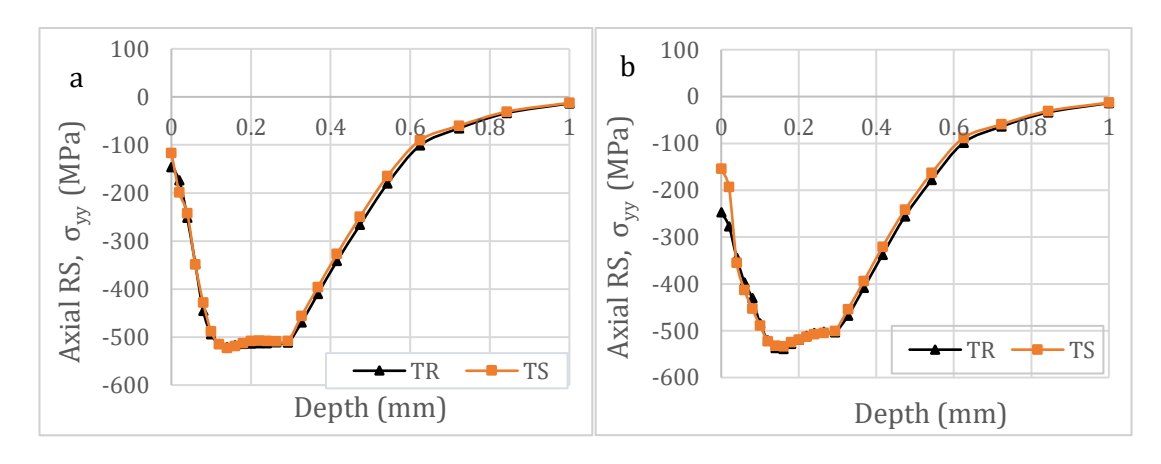


Figure 4.24: Axial residual stress distribution for tool sliding and rolling condition at Fb 348N, a) at the centre of contact and b) at the centre of overlap

4.4. Validation of FEM residual stress results

Validation of finite element modelling of ball burnishing distribution of residual stress is an essential step to ensure the model accuracy and reliability. The comparison is performed between the 3D FEM result and the XRD measurement results obtained at a burnishing force of 275N by Solis Garduño Rosalinda, PhD, a researcher at the LTDS. The XRD residual stress experimental measurement was performed just once without repeated tests.

The surface lateral residual stress XRD measurement compressive stress is higher by 22.8 % compared with the FEM residual stress extracted at the centre of contact (Cc) shown in Figure 4.25. Whereas the axial residual stress surface XRD measurement is also higher by 7.8% when compared with the FEM residual stress extracted at the centre of overlap (Co), illustrated in Figure 4.26. The highlighted comparison shows that the lateral FEM residual stress slightly underestimates the experimental residual stresses. However, better agreement is observed for the axial residual stress extracted at the centre of overlap. The spot diameter of the XRD measurement was 2mm. Due to the spot diameter, the comparison with the average surface residual stress presented in Figure 4.20, proves that XRD measurement experienced a higher compressive stress for both axial and lateral residual stress.

An observation of lateral and axial residual stress distribution through the depth clearly illustrated that the maximum compressive stress for both XRD and FEM prediction occurs beneath the surface, with a higher XRD measurement stress-affected zone, as indicated in Figure 4.25 and Figure 4.26. Although the stress-affected zone and compressive stress are higher in the XRD measurement, considering the experimental uncertainties, both lateral and axial residual stress FEM results show a good agreement with the experimental XRD measurement throughout the depth.

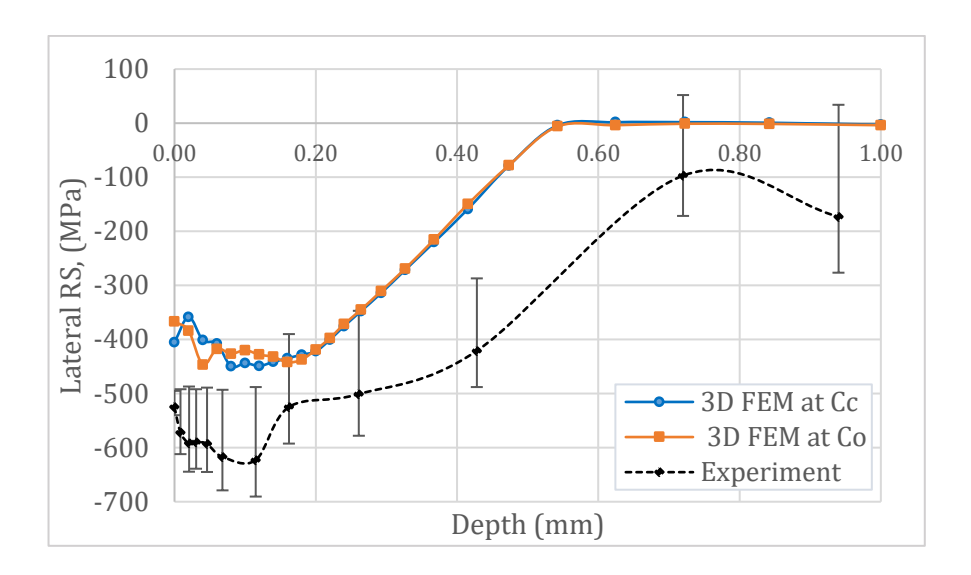


Figure 4.25: Comparison of lateral residual stress (RS) distribution through the depth between 3D FEM results and XRD measurements

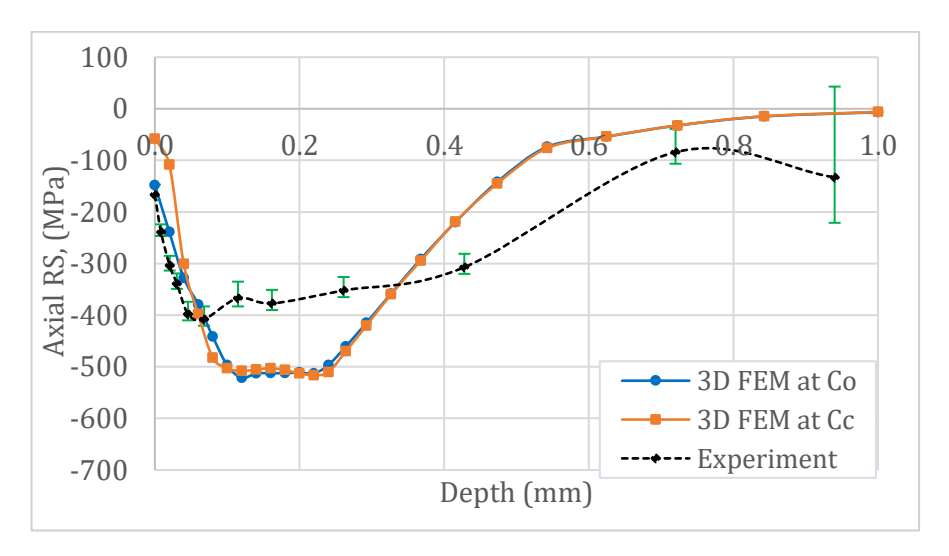


Figure 4.26 : Comparison of axial residual stress (Rs) distribution through the depth between 3D FEM results and XRD measurements

4.5. FEM modelling computational performance

Studying the computational performance of the EM modelling of ball burnishing is crucial for the sustainable implementation of the process through FEM modelling for ball burnishing. The sustainable computational performance of the FEM model for ball burnishing primarily depends on computational time and resource requirements. Those two parameters are critical in numerical simulations for industrial applications in terms of cost.

The average computation time, time increment and ODB file sizes are recorded for an Explicit sliding, Explicit rolling and Implicit analysis as presented in Table 4.2.

| FEM Model | Number of | Computation Time | Increment | ODb file size per |
|-------------------|-----------|------------------|------------------------|-------------------|
| | Elements | | Time (ms) | model (GB) |
| Explicit sliding | 232,962 | 1 d 1 h 20 min | 2.55×10 ⁻⁶ | 2.29 |
| Explicit rolling | 277,424 | 1 d 12 h 55 min | 2.62×10-6 | 1.9 |
| Standard/Implicit | 204,960 | 4 d 23 h 9 min | 1.68 ×10 ⁻² | 16 |

Table 4.2: Explicit and implicit FEM modelling computational performance

Initially, a multi-tool pass FEM modelling was tested to analyse using a dynamic Explicit analysis. However, the number of increments exceeded the allowable range of Abaqus due to the large number of elements generated on the workpiece, which required a short time increment. It did not execute more than three tool passes. A dynamic Explicit with ball rolling assumption required higher computational time, even having a higher time increment and relatively smaller ODB file size, as shown in Figure 4.27. This is based on a fixed tool consideration, accounting for 38.17% of the total fine mesh elements. The computational time primarily depends on the total number of elements to be executed and the storage requirements, which are influenced by the type and frequency of field output recorded during the analysis. In contrast, the Sliding ball assumption has a low computational time, with a 1% fine mesh number of elements generated on the spherical cap of the burnishing tool. Therefore, a standard implicit analysis approach and a dynamic explicit analysis approach of slide burnishing by a spherical cap tool are efficient FEM modelling approaches in terms of computational performance and cost.

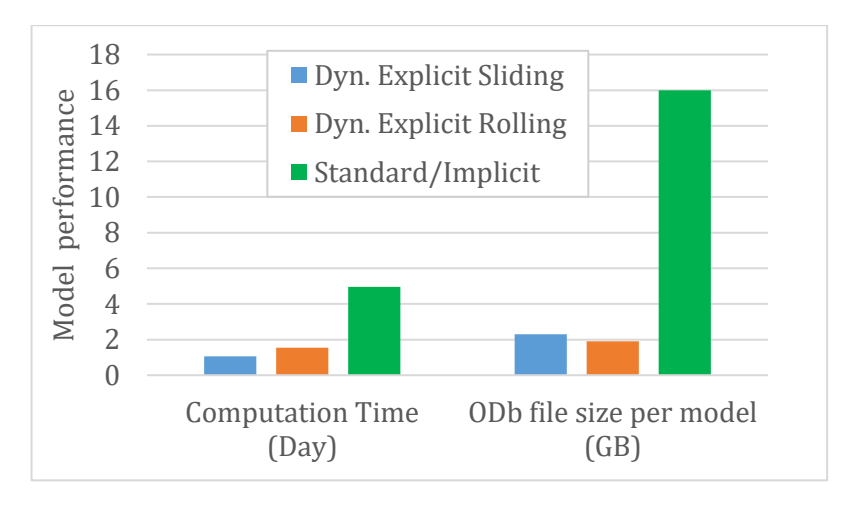


Figure 4.27 : Comparison of Computational performance for the dynamic explicit and implicit FEM modelling approach.

Chapter 5

Conclusion and future work

5.1. Conclusion

The current study focuses on the numerical simulation of the ball burnishing process using hybrid explicit-implicit 3D finite element modelling (FEM) methods on Aluminium 2024 work material. For dynamic Explicit analysis, a 3mm radius spherical cap and a 6 mm diameter spherical ball are designed to represent a real slide burnishing and roller burnishing, respectively, for a small cut section rectangular plate. Burnishing forces of 275N, 348N, and 420N at a tool travel speed of 80 mm/min are considered for the sliding tool FEM analysis under working conditions. A 348 N burnishing force is also applied at the same speed for the tool rolling condition. After validating the dynamic explicit analysis, a standard/Implicit analysis was performed using a normal stress extracted from a stable region of explicitly burnished work material, at a speed of 80 m/min and a feed of 0.16 mm/rev for 10 tool passes. The following key findings are summarised.

- According to dynamic Explicit analysis, a tool rolling action creates up to 20% deeper penetration depth than a tool sliding burnishing condition at a burnishing force of 348N. An increased burnishing force produces greater penetration depth, longer contact length and higher contact pressure. It shows a good agreement with Hertz contact theory, and the generated maximum pressure is enough to produce plastic deformation.
- Although the FEM modelling was performed under a frictionless condition, a small tangential reaction force was generated due to the burnishing tool ploughing effect, and a normal reaction force shows an accurate load transfer of the model for both sliding and rolling conditions.
- At the tool sliding condition, the nodal temperature produced at the contact region can reach up to 43°C at 420 N applied burnishing force, while the temperature difference between the tool sliding and tool rolling conditions is insignificant. Low temperature had no notable effect on the residual stress of the burnished component.

- Based on a detailed fine elemental study of the spherical cap burnishing tool and work material contact at a burnishing force of 348N, the maximum compressive normal stress and shear stress reached -1800MPa and -180MPa, respectively.
- The maximum temperature can reach up to 38°C, which was produced precisely at the centre of contact at Fb 348 N. The generated heat flux was higher at the midpoint of the feed direction and at the trailing edge of the burnishing direction, 14,000 kW/m² under the same working conditions.
- The maximum equivalent plastic strain is produced 0.02mm beneath the surface, and it can reach up to 0.14, 0.17 and 0.21 for 275N, 348N and 420N, respectively.
 The contribution of the tool sliding and rolling conditions for the generated plastic strain is negligible.
- Between 1st and 8th tool passes, the maximum surface average compressive axial residual stress is -146.24 MPa for tool sliding and -209.39 MPa for rolling condition at burnishing force 348 N. While lateral residual stress is 473.05MPa and -478.36 MPa for tool sliding and rolling conditions, respectively, at a burnishing force of 348N. The tool rolling condition increased surface compressive lateral and axial residual stresses by up to 1.1% and 43.2%, respectively, compared with the tool sliding condition.
- A sinusoidal curve was observed for both surface equivalent plastic strain and residual stress distribution, but it can be improved by reducing the feed rate.
- To produce a surface compressive residual stress, it requires more than two tool
 passes for FEM modelling the ball burnishing process. A maximum lateral
 residual stress occurs at the surface, and it can affect up to 0.6mm deep. The
 maximum surface compressive axial stress is produced below the surface
 between 0.15 mm and 0.2mm, which also affects compressive stress up to 1 mm
 below the surface.
- The XRD experimental result and literature finding reveal good agreement with numerical results. Notably, surface axial residual stress can be obtained in a difference of up to 7.8% compared to experimental XRD measurements at a burnishing force of 257N and a tool sliding condition.
- Dynamic Explicit analysis is computationally efficient to replicate a real physical ball burnishing process in a short time. In contrast, Static Implicit analysis is better for long-duration and multi-tool pass simulation. In terms of FEM model computational performance, a tool sliding condition is more efficient than a tool rolling condition.

In general, the present study developed a hybrid Explicit-Implicit FEM modelling approach for simulating the ball burnishing process performed on Aluminium 2024 alloy to predict residual stress. The obtained final axial and lateral residual stress results show a good agreement with literature findings and experimental XRD measurements. This study presents a promising and tangible approach to estimating the fatigue life of aircraft structural components made from aerospace-grade 2024 aluminium alloy materials. Additionally, a developed FEM model can help engineers reduce the need for extensive experimental studies for both the ball burnishing process and XRD measurements of residual stress, thereby saving time and cost. It is recommended to use it directly for different Aluminium 2024 alloys, not only in Aerospace but also in the automotive industries by changing specific material properties.

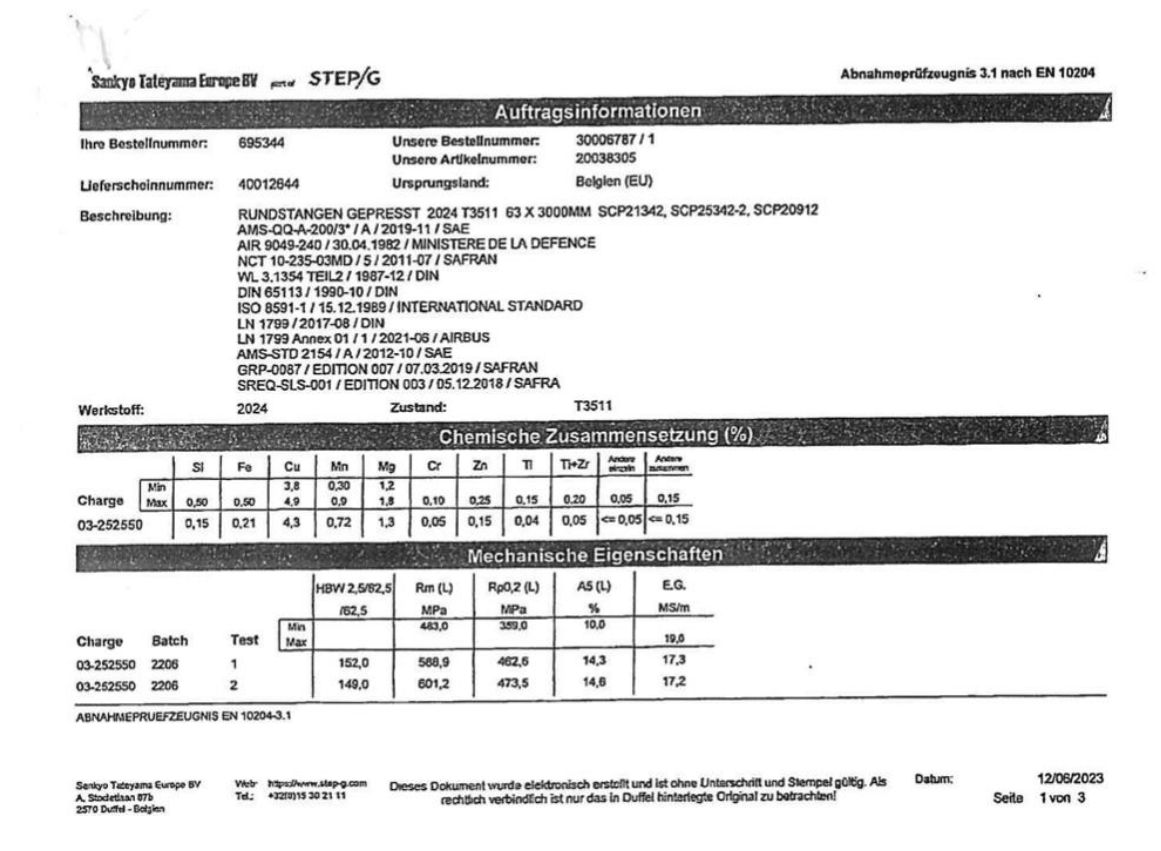
5.2. Future work:

Although the current finite element modelling for the ball burnishing process indicates a good approach to predicting residual stress, the study has some limitations that remain open for future work.

- The current study's FEM model was developed by varying the burnishing force;
 however, the future work should also investigate the influence of other working conditions, including the coefficient of friction, ball diameter and feed rate.
- The current finite element model was built through the Johnson-Cook material
 constitutive law, whose parameters were obtained from various findings from
 different Aluminium 2024 alloys and provided by the LTDS researcher.
 Therefore, the JC constitutive behaviour parameter and the mechanical
 properties of a particular material must be experimentally characterised to
 compare the result with physical XRD measurement
- The experimental validation for residual stress was carried out using FEM results with real XRD measurements. But the XRD measurement was not repeated for the same burnished component. At least three repeated experimental XRD measurements are necessary to ensure the accuracy of the measurement.
- Further investigations are also recommended to incorporate additional surface integrity properties into the study.

Appendix A

Material certificate for Al 2024 -T3511



Appendix B

Temperature-dependent material properties of Al 2024 alloy

| Al 2024 Alloy | Unit | T(°C) |
|---|----------|-------|
| Density, ρ [kg/m³] | 2770 | 20 |
| Youngs Modulus, E [Mpa] | 72400 | 20 |
| | 66500 | 100 |
| | 60400 | 200 |
| | 56100 | 300 |
| | 50000 | 400 |
| Poisson's Ratio, ϑ | 0.33 | 20 |
| Thermal conductivity, λ [W. m^{-1} . ${}^{\circ}C^{-1}$] | 121,1 | 20 |
| | 133 | 100 |
| | 148,3 | 200 |
| | 178 | 300 |
| | 176,3 | 400 |
| Specific heat , C_p)[W. $kg^{-1} \circ C^{-1}$] | 877 | 20 |
| | 918 | 100 |
| | 962 | 200 |
| | 1003 | 300 |
| | 1044 | 400 |
| Taylor Quinney Coefficient and strain rate, β | 0,85 | |
| Thermal expansion coefficient, α | 2,32E-05 | 20 |
| | 2,47E-05 | 250 |
| | | |

Appendix C

Implicit FEM model INP file modification Python script.

```
###EFFICIENT INP MODIFICATION SCRIPT
import pandas as pd
import os
# Define the paths to your Excel files
element set excel path = r'C:\temp\INTERNSHIP\STANDARD MODEL
4\INP MODIFICATION\Standard Model ELT ID.xlsx'
amplitude_excel_path = r'C:\temp\INTERNSHIP\STANDARD MODEL
4\INP_MODIFICATION\TS_Dyn_Exp_S33_F348_Result_Amplitude.xlsx'
inp file path = r'C:\temp\INTERNSHIP\STANDARD MODEL
4\INP MODIFICATION\FINAL BB FEM 10R INP Standard model.inp'
output file path = r'C:\temp\INTERNSHIP\STANDARD MODEL
4\INP MODIFICATION\MODIFIED FINAL BB FEM 10R F348 INP Standard model.in
p'
# Define the element sets from the element set Excel file
element sets = {}
for index, row in element_set_data.iterrows():
    element_sets[index + 1] = row.dropna().tolist()
# Find the index to insert the new element sets
insert index = None
for i in range(len(lines)):
    if "_SUR_UPPER_S5, S5" in lines[i]:
        insert index = i + 1
        while lines[insert_index].strip() and not
lines[insert index].startswith('*'):
            insert index += 1
        break
# Insert the element sets into the lines
for i in range(1, len(element_sets) + 1):
    lines.insert(insert_index, f"*Elset, elset=_Line_{i}, internal,
instance=ALMWP-1\n")
    elements = element_sets[i]
    for j in range(0, len(elements), 16):
        lines.insert(insert_index + 1, ", ".join(map(str,
elements[j:j+16])) + "\n")
```

```
insert_index += 1
    insert_index += 1
# Create individual element sets and surfaces
individual insert index = insert index
for set_id in element_sets:
   for idx, element_id in enumerate(element_sets[set_id], start=1):
        lines.insert(individual insert index, f"*Elset,
elset=_L{set_id}E{idx}_S5, internal, instance=ALMWP-1\n")
        lines.insert(individual_insert_index + 1, f"{element_id}\n")
        lines.insert(individual_insert_index + 2, f"*Surface,
type=ELEMENT, name=L{set_id}E{idx}\n")
        lines.insert(individual_insert_index + 3,
f"_L{set_id}E{idx}_S5, S5\n")
        individual_insert_index += 4
# Generate amplitude names
amplitude_names = [f"AMP_L{L}E{line_idx}" for L in range(1, 71) for
line_idx in range(1, len(amplitude_data) + 1)]
# Function to generate pressure loading
def generate_pressure_loading(elements, step, amplitude_names):
    inp_content = f"** STEP: Revolution-{step}\n"
   for i, element_name in enumerate(elements):
        name = f"R{step}_{element_name}"
        amplitude = amplitude_names[i % len(amplitude_names)]
        inp_content += f"** Name: {name} Type: Pressure\n"
        inp content += f"*Dsload, op=NEW, amplitude={amplitude}\n"
        inp_content += f"{element_name}, P, -1\n"
    return inp_content
# Generate loading content for steps 1 to 10
loading contents = []
for step in range(1, 11):
    start_idx = (step - 1) * 8 + 1
    end idx = start idx + 50
    loading_element_id = [f"L{set_id}E{idx}" for set_id in element_sets
for idx in range(start_idx, end_idx)]
    loading_contents.append(generate_pressure_loading(loading_element_i
d, step, amplitude_names))
# Insert the loading content into the lines
for idx, insert_index in enumerate(loading_insert_indices):
    if idx < len(loading_contents):</pre>
        lines.insert(insert index, loading contents[idx])
   else:
        print(f"Warning: Step {idx+1} exceeds the length of
loading contents")
```

```
# Find the index to insert amplitude data after *End Assembly
end_assembly_index = None
for i in range(len(lines)):
    if "*End Assembly" in lines[i]:
        end_assembly_index = i + 1
        break
# Insert amplitude data after *End Assembly
if end_assembly_index is not None:
    amplitude_lines = []
    for L in range(1, len(element sets) + 1):
        for line_idx in range(1, len(amplitude_data) + 1):
            amplitude_lines.append(f"*Amplitude,
name=AMP_L{L}E{line_idx}\n")
            amplitude line = ""
            seen_pairs = set()
            for time_idx, time_value in enumerate(time_data):
                modified_time_value = time_value + (L - 1) * 1.5e-05
                time_str = f"{modified_time_value:.6f}" if
modified_time_value != 0 else "0."
                amplitude str = f"{amplitude data.iloc[line idx - 1,
time_idx]:.2f}" if amplitude_data.iloc[line_idx - 1, time_idx] != 0
else "0."
                pair = (time_str, amplitude_str)
                if pair not in seen pairs:
                    amplitude_line +=
f"{time_str},
                  {amplitude_str}, "
                    seen pairs.add(pair)
                if (time idx + 1) % 4 == 0:
                    amplitude_line =
amplitude_line.rstrip(",
                                  ")
                    amplitude lines.append(amplitude line + "\n")
                    amplitude line = ""
            if amplitude_line:
                amplitude_line = amplitude_line.rstrip(", ")
                amplitude lines.append(amplitude line + "\n")
    lines[end_assembly_index:end_assembly_index] = amplitude_lines
# Write the modified lines to the output file
write_inp_file(output_file_path, lines)
print("Element sets, surfaces, and 11-step loading/unloading have been
added to the output file.")
```

Appendix D

Residual stress extraction Python script.

```
###STANDARD FEM MODEL RESIDUAL STRESS THROUGH THE DEPTH
from odbAccess import *
from abaqusConstants import *
import csv
# Open the ODB file
odb_path = 'C:\\temp\\INTERNSHIP\\STANDARD MODEL 4\\SERVER FILE\\ODB
FILE\\FINAL BB FEM 10R F275 INP Standard model.odb'
odb_file = openOdb(odb_path)
# Access the correct instance and element set
target instance = odb file.rootAssembly.instances['ALMWP-1']
all_elts_set = target_instance.elementSets['ALMWP'].elements
# Parameters
lines = 10
elements_per_line = 24
x increment = 6720
first_half_count = 12
second_half_count = 12
start_id_decreasing = 20966
start id increasing = 122675
# Access the last frame of Step-11
step = odb file.steps['Step-11']
last_frame = step.frames[-1]
# Extract stress and PEEQ values
stress_field = last_frame.fieldOutputs['S'].values
peeq_field = last_frame.fieldOutputs['PEEQ'].values
# Create lookup dictionaries
stress_dict = {val.elementLabel: val.data for val in stress_field}
peeq_dict = {val.elementLabel: val.data for val in peeq_field}
# Output file
output_file = 'step11_last_frame_results_Z_direction_pattern.csv'
with open(output_file, 'w', newline='') as csvfile:
    csvwriter = csv.writer(csvfile)
    csvwriter.writerow(['Line', 'Element ID', 'S11', 'S22', 'S33',
'PEEQ'])
    for line in range(lines):
```

```
# Compute base IDs for this line
        base_dec = start_id_decreasing + line * x_increment
        base_inc = start_id_increasing + line * x_increment
        # First 12 elements: decreasing by 70
        first_half = [base_dec - i * 70 for i in
range(first_half_count)]
        # Next 12 elements: increasing by 70
        second_half = [base_inc + i * 70 for i in
range(second_half_count)]
        # Combine both halves
        line_elements = first_half + second_half
        line_label = f"Line {line + 1}"
        # Print extracted element IDs before processing
        print(f"\n{line_label} - Extracted Element IDs:")
        print(line_elements)
        # Extract and write results
        for eid in line_elements:
            if eid in stress_dict and eid in peeq_dict:
                s11, s22, s33 = stress_dict[eid][0],
stress_dict[eid][1], stress_dict[eid][2]
                peeq = peeq_dict[eid]
                csvwriter.writerow([line_label, eid, f"{s11:.2f}",
f"{s22:.2f}", f"{s33:.2f}", f"{peeq:.5f}"])
                print(f"{line_label} | Element ID: {eid} | S11:
{s11:.2f}, S22: {s22:.2f}, S33: {s33:.2f}, PEEQ: {peeq:.5f}")
# Final confirmation
print(f"\n✓ Results saved to: {output file}")
```

Bibliography

- [1] D. Mahajan and R. Tajane, 'A Review on Ball Burnishing Process', *Int. J. Sci. Res. Publ.*, Apr. 2013.
- [2] A. Khadimallah, J. Petit, N. Hfaiedh, and A. Znaidi, 'Characterization of fatigue behavior of AA2024-T351 aluminum alloy', *Fatigue Fract. Eng. Mater. Struct.*, vol. 46, no. 10, pp. 3729–3744, Oct. 2023, doi: 10.1111/ffe.14102.
- [3] S. Li *et al.*, 'Development and applications of aluminum alloys for aerospace industry', *J. Mater. Res. Technol.*, vol. 27, pp. 944–983, Nov. 2023, doi: 10.1016/j.jmrt.2023.09.274.
- [4] Chetan B S., 'Fatigue life estimation of the rear fuselage structure of an aircraft.', *Int. J. Res. Eng. Technol.*, vol. 04, no. 07, pp. 347–354, July 2015, doi: 10.15623/ijret.2015.0407056.
- [5] Sp. G. Pantelakis and A. Th. Kermanidis, 'Fatigue Crack Growth of Aircraft Aluminum Alloys', in *Multiscale Fatigue Crack Initiation and Propagation of Engineering Materials: Structural Integrity and Microstructural Worthiness*, vol. 152, G. C. Sih, Ed., in Solid Mechanics and its Applications, vol. 152., Dordrecht: Springer Netherlands, 2008, pp. 345–366. doi: 10.1007/978-1-4020-8520-8_13.
- [6] T. Dursun and C. Soutis, 'Recent developments in advanced aircraft aluminium alloys', *Mater. Des. 1980-2015*, vol. 56, pp. 862–871, Apr. 2014, doi: 10.1016/j.matdes.2013.12.002.
- [7] B. B. Verma, J. D. Atkinson, and M. Kumar, 'Study of fatigue behaviour of 7475 aluminium alloy', *Bull. Mater. Sci.*, vol. 24, no. 2, pp. 231–236, Apr. 2001, doi: 10.1007/BF02710107.
- [8] J. P. Davim, Ed., *Surface Integrity in Machining*. London: Springer London, 2010. doi: 10.1007/978-1-84882-874-2.
- [9] Harish, D. Shivalingappa, N. Raghavendra, and V. Ganesh, 'Impact of Ball Burnishing Process on Residual stress distribution in Aluminium 2024 Alloy using Experimental and Numerical Simulation', *IOP Conf. Ser. Mater. Sci. Eng.*, vol. 1189, no. 1, p. 012002, Oct. 2021, doi: 10.1088/1757-899X/1189/1/012002.
- [10] A. J. Alshareef, I. D. Marinescu, I. M. Basudan, B. M. Alqahtani, and M. Y. Tharwan, 'Ball-burnishing factors affecting residual stress of AISI 8620 steel', *Int. J. Adv. Manuf. Technol.*, vol. 107, no. 3–4, pp. 1387–1397, Mar. 2020, doi: 10.1007/s00170-020-05119-x.
- [11] M. Bourebia *et al.*, 'Effect of ball burnishing process on mechanical properties and impact behavior of S355JR steel', *Int. J. Adv. Manuf. Technol.*, vol. 116, no. 3–4, pp. 1373–1384, Sept. 2021, doi: 10.1007/s00170-021-07454-z.
- [12] E. Becerra-Becerra, C. O. Aguilera Ojeda, A. Saldaña-Robles, J. F. Reveles-Arredondo, J. Barco-Burgos, and A. Vidal-Lesso, 'A review of numerical simulation of ball burnishing process', *Finite Elem. Anal. Des.*, vol. 218, p. 103926, June 2023, doi: 10.1016/j.finel.2023.103926.
- [13] J. T. Maximov, G. V. Duncheva, A. P. Anchev, and M. D. Ichkova, 'Slide burnishing—review and prospects', *Int. J. Adv. Manuf. Technol.*, vol. 104, no. 1–4, pp. 785–801, Sept. 2019, doi: 10.1007/s00170-019-03881-1.
- [14] J. T. Maximov, G. V. Duncheva, A. P. Anchev, N. Ganev, I. M. Amudjev, and V. P. Dunchev, 'Effect of slide burnishing method on the surface integrity of AISI 316Ti chromium–nickel steel', *J. Braz. Soc. Mech. Sci. Eng.*, vol. 40, no. 4, p. 194, Apr. 2018, doi: 10.1007/s40430-018-1135-3.
- [15] G. and T. Bellows Dean N., 'Introduction to Surface Integrity', General Electric Aircraft Engine Group, Cincinnati, Ohio, Pamphlet TM70-974, 1970.

- [16] V. Chomienne, F. Valiorgue, J. Rech, and C. Verdu, 'Influence of ball burnishing on residual stress profile of a 15-5PH stainless steel', *CIRP J. Manuf. Sci. Technol.*, vol. 13, pp. 90–96, May 2016, doi: 10.1016/j.cirpj.2015.12.003.
- [17] D. Borysenko, F. Welzel, B. Karpuschewski, J. Kundrák, and V. Voropai, 'Simulation of the burnishing process on real surface structures', *Precis. Eng.*, vol. 68, pp. 166–173, Mar. 2021, doi: 10.1016/j.precisioneng.2020.12.004.
- [18] W. K. Liu, S. Li, and H. S. Park, 'Eighty Years of the Finite Element Method: Birth, Evolution, and Future', *Arch. Comput. Methods Eng.*, vol. 29, no. 6, pp. 4431–4453, Oct. 2022, doi: 10.1007/s11831-022-09740-9.
- [19] H. Khanna and H. Singh, 'Burnishing Process for Surface Enhancement in Manufacturing Industry: A Comprehensive Review', 2024.
- [20] A. Saldaña Robles, J. A. Diosdado De La Peña, A. D. J. Balvantin Garcia, E. Aguilera Gomez, H. Plasencia Mora, and N. Saldaña Robles, "The Ball-Burnishing Process: State of the Art of a Developing Technology", *DYNA Ing. E Ind.*, vol. 92, no. 1, pp. 28–33, 2017, doi: 10.6036/7916.
- [21] N. S. M. El-Tayeb, K. O. Low, and P. V. Brevern, 'Influence of roller burnishing contact width and burnishing orientation on surface quality and tribological behaviour of Aluminium 6061', *J. Mater. Process. Technol.*, vol. 186, no. 1–3, pp. 272–278, May 2007, doi: 10.1016/j.jmatprotec.2006.12.044.
- [22] Eric Velázquez Corral, 'Application of the ball burnishing process on rotationally symmetrical parts to improve their fatigue resistance and wear properties', Institut National Polytechnique de Toulouse INPT; Universitat Politècnica de Catalunya BarcelonaTech, 2023.
- [23] J. A. Travieso-Rodriguez *et al.*, 'Effects of a ball-burnishing process assisted by vibrations in G10380 steel specimens', *Int. J. Adv. Manuf. Technol.*, vol. 81, no. 9–12, pp. 1757–1765, Dec. 2015, doi: 10.1007/s00170-015-7255-3.
- [24] F. Valiorgue *et al.*, 'Influence of residual stress profile and surface microstructure on fatigue life of a 15-5PH', *Procedia Eng.*, vol. 213, pp. 623–629, 2018, doi: 10.1016/j.proeng.2018.02.058.
- [25] Assault Systèmes Simulia, ABAQUS Analysis User's Manual, Version 6.6, 2006 2007.
- [26] R. Teimouri, S. Amini, and A. B. Bami, 'Evaluation of optimized surface properties and residual stress in ultrasonic assisted ball burnishing of AA6061-T6', *Measurement*, vol. 116, pp. 129–139, Feb. 2018, doi: 10.1016/j.measurement.2017.11.001.
- [27] M. Sayahi, S. Sghaier, and H. Belhadjsalah, 'Finite element analysis of ball burnishing process: comparisons between numerical results and experiments', *Int. J. Adv. Manuf. Technol.*, vol. 67, no. 5–8, pp. 1665–1673, July 2013, doi: 10.1007/s00170-012-4599-9.
- [28] G. V. Duncheva, J. T. Maximov, A. P. Anchev, V. P. Dunchev, T. P. Atanasov, and J. Capek, 'Finite element and experimental study of the residual stresses in 2024-T3 Al alloy treated via single toroidal roller burnishing', *J. Braz. Soc. Mech. Sci. Eng.*, vol. 43, no. 1, p. 55, Jan. 2021, doi: 10.1007/s40430-020-02775-8.
- [29] D. Yin, H. Zhao, Y. Chen, J. Chang, Y. Wang, and X. Wang, 'Modification of Johnson–Cook Constitutive Parameters in Ball Burnish Simulation of 7075-T651 Aluminum Alloy', *Metals*, vol. 13, no. 12, p. 1992, Dec. 2023, doi: 10.3390/met13121992.
- [30] G. R. Johnson and W. H. Cook, 'A Constitutive Model and Data for Metals Subjected to Large Strains, High Strain Rates and High Temperatures.', no. Proceedings, 7th International Symposium on Ballistics, Hague, The Netherlands, pp. 541-547., 1983.
- [31] C. Amini, R. Jerez-Mesa, J. A. Travieso-Rodriguez, J. Llumà, and A. Estevez-Urra, 'Finite Element Analysis of Ball Burnishing on Ball-End Milled Surfaces Considering Their Original Topology and Residual Stress', *Metals*, vol. 10, no. 5, p. 638, May 2020, doi: 10.3390/met10050638.

- [32] L. G. Wang, Z. Li, L. Zhang, R. Zhou, and X. Chen, 'On the Measurement of Particle Contact Curvature and Young's Modulus Using X-ray μCT', *Appl. Sci.*, vol. 11, no. 4, p. 1752, Feb. 2021, doi: 10.3390/app11041752.
- [33] A. Torres, C. Amini, N. Cuadrado, J. A. Travieso-Rodriguez, J. Llumà, and M. Vilaseca, 'Experimental validation of ball burnishing numerical simulation on ball-end milled martensitic stainless-steel considering friction and the initial surface topography', *J. Mater. Res. Technol.*, vol. 22, pp. 3352–3361, Jan. 2023, doi: 10.1016/j.jmrt.2022.12.100.
- [34] B. Yang, 'Comparisons of implicit and explicit time integration methods in finite element analysis for linear elastic material and quasi-brittle material in dynamic problems'.
- [35] U. Huner, G. Irsel, U. Bekar, and M. Szala, 'A comprehensive case study to the implicit and explicit approach in finite element analysis', *Adv. Sci. Technol. Res. J.*, vol. 19, no. 2, pp. 407–417, Dec. 2024, doi: 10.12913/22998624/196987.
- [36] 'Implicit Vs Explicit Finite Element Analysis: When to Use Which'. Accessed: Sept. 07, 2025. [Online]. Available: https://blog.technia.com/en/simulation/implicit-vs-explicit-finite-element-analysis
- [37] A. Nemade and A. Shikalgar, 'The Mesh Quality significance in Finite Element Analysis', vol. Volume 17, no. Issue 2, p. PP 44-48, 2020, doi: DOI:%2010.9790/1684-1702054448.
- [38] G. V. Duncheva, J. T. Maximov, V. P. Dunchev, A. P. Anchev, and T. P. Atanasov, 'Improvement in Fatigue Performance of 2024-T3 Al Alloy Via Single Toroidal Roller Burnishing', *J. Mater. Eng. Perform.*, vol. 30, no. 3, pp. 2256–2266, Mar. 2021, doi: 10.1007/s11665-021-05535-4.
- [39] R. Kluz, M. Bucior, A. Dzierwa, K. Antosz, W. Bochnowski, and K. Ochał, 'Effect of Diamond Burnishing on the Properties of FSW Joints of EN AW-2024 Aluminum Alloys', *Appl. Sci.*, vol. 13, no. 3, p. 1305, Jan. 2023, doi: 10.3390/app13031305.
- [40] Harish and D. Shivalingappa, 'The influence of ball and roller burnishing process parameters on surface integrity of Al 2024 alloy', *Mater. Today Proc.*, vol. 27, pp. 1337–1340, 2020, doi: 10.1016/j.matpr.2020.02.614.
- [41] Y. Charfeddine, S. Youssef, S. Sghaier, J. Sghaier, and H. Hamdi, 'Study of the simultaneous Grinding/Ball-burnishing of AISI 4140 based on finite element simulations and experiments', *Int. J. Mech. Sci.*, vol. 192, p. 106097, Feb. 2021, doi: 10.1016/j.ijmecsci.2020.106097.
- [42] Y. C. Yen, P. Sartkulvanich, and T. Altan, 'Finite Element Modeling of Roller Burnishing Process', *CIRP Ann.*, vol. 54, no. 1, pp. 237–240, 2005, doi: 10.1016/S0007-8506(07)60092-4.
- [43] L. Kamgaing Souop, A. Daidie, Y. Landon, J. Senatore, and M. Ritou, 'Investigation of Aluminum Alloy Properties During Helical Roller Burnishing Through Finite Element Simulations and Experiments', in *Advances on Mechanics, Design Engineering and Manufacturing II*, F. Cavas-Martínez, B. Eynard, F. J. Fernández Cañavate, D. G. Fernández-Pacheco, P. Morer, and V. Nigrelli, Eds, in Lecture Notes in Mechanical Engineering., Cham: Springer International Publishing, 2019, pp. 440–450. doi: 10.1007/978-3-030-12346-8_43.
- [44] M. Dumas *et al.*, '3D numerical modelling of turning-induced residual stresses A two-scale approach based on equivalent thermo-mechanical loadings', *J. Mater. Process. Technol.*, vol. 297, p. 117274, Nov. 2021, doi: 10.1016/j.jmatprotec.2021.117274.
- [45] 'Laboratoire de Tribologie et Dynamique des Systèmes École Centrale de Lyon', https://www.ec-lyon.fr/recherche-et-innovation/les-laboratoires/laboratoire-de-tribologie-et-dynamique-des-systemes.
- [46] N. Zhao, Y. Yang, M. Han, X. Luo, G. Feng, and R. Zhang, 'Finite element analysis of pressure on 2024 aluminum alloy created during restricting expansion-

- deformation heat-treatment', *Trans. Nonferrous Met. Soc. China*, vol. 22, no. 9, pp. 2226–2232, Sept. 2012, doi: 10.1016/S1003-6326(11)61453-2.
- [47] D. Manasijević *et al.*, 'Study of thermal properties of the aluminium EN AW 2024-T3 alloy', *Kov. Mater.-Met. Mater.*, vol. 62, no. 1, May 2024, doi: 10.31577/km.2024.1.31.
- [48] T. Mabrouki, F. Girardin, M. Asad, and J.-F. Rigal, 'Numerical and experimental study of dry cutting for an aeronautic aluminium alloy (A2024-T351)', *Int. J. Mach. Tools Manuf.*, vol. 48, no. 11, pp. 1187–1197, Sept. 2008, doi: 10.1016/j.ijmachtools.2008.03.013.
- [49] K. C. Chung-Kyu Park, Paul Du Bois, and Cing-Dao Kan, 'Development of Effective Taylor- Quinney Coefficient Tables of *MAT_224 for Aluminum 2024- T351, Titanium 6Al-4V, and Inconel 718 Alloys', Federal Aviation Administration William J. Hughes Technical Center Aviation Research Division Atlantic City International Air, New Jersey, DOT/FAA/TC-23/48, July 2023.
- [50] J. D. Seidt and A. Gilat, 'Plastic deformation of 2024-T351 aluminum plate over a wide range of loading conditions', *Int. J. Solids Struct.*, vol. 50, no. 10, pp. 1781–1790, May 2013, doi: 10.1016/j.ijsolstr.2013.02.006.
- [51] H. Livatyali, E. Has, and M. Türköz, 'Prediction of residual stresses in ball burnishing TI6AL4V thin sheets', *Int. J. Adv. Manuf. Technol.*, vol. 110, no. 3–4, pp. 1083–1093, Sept. 2020, doi: 10.1007/s00170-020-05837-2.
- [52] V. Kuznetsov, I. Smolin, A. Skorobogatov, and A. Akhmetov, 'Finite Element Simulation and Experimental Investigation of Nanostructuring Burnishing AISI 52100 Steel Using an Inclined Flat Cylindrical Tool', *Appl. Sci.*, vol. 13, no. 9, p. 5324, Apr. 2023, doi: 10.3390/app13095324.
- [53] B. Hoddy, N. Ahmed, K. Al-Lamee, N. Bullett, N. Curzen, and N. W. Bressloff, 'Investigating the Equivalent Plastic Strain in a Variable Ring Length and Strut Width Thin-Strut Bioresorbable Scaffold', *Cardiovasc. Eng. Technol.*, vol. 13, no. 6, pp. 899–914, Dec. 2022, doi: 10.1007/s13239-022-00625-3.